Modelling, Control and Integration of Distributed Generators for Enhanced Ancillary Services

Raboni, Pietro

DOI (link to publication from Publisher):
10.5278/vbn.phd.engsci.00051

Publication date:
2016

Document Version
Publisher's PDF, also known as Version of record

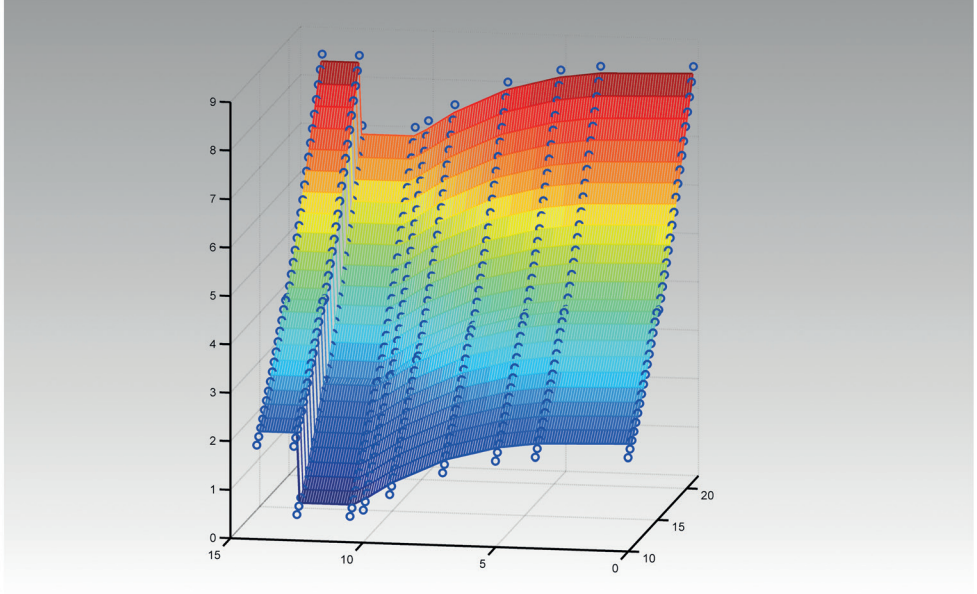

MODELLING, CONTROL AND INTEGRATION OF DISTRIBUTED GENERATORS FOR ENHANCED ANCILLARY SERVICES

BY
PIETRO RABONI

DISSERTATION SUBMITTED 2016

AALBORG UNIVERSITY
DENMARK

MODELLING, CONTROL AND INTEGRATION OF DISTRIBUTED GENERATORS FOR ENHANCED ANCILLARY SERVICES

by

Pietro Raboni

AALBORG UNIVERSITY
DENMARK

Dissertation submitted

.

Dissertation submitted:	January 31st, 2016
PhD supervisor:	Prof. Zhe Chen Aalborg University
Assistant PhD supervisor:	Associate Prof. Sanjay Chaudhary Aalborg University
PhD committee:	Associate Professor Jayakrishnan Radhakrishna Pillai (chairman), Department of Energy Technology Aalborg University
	Principal Scientist, Silvia Mastellone ABB Corporate Research ABB Schweiz AG
	Senior Researcher, Anca D. Hansen Wind Energy Department Technical University of Denmark, DTU
PhD Series:	Faculty of Engineering and Science, Aalborg University

ISSN (online): 2246-1248
ISBN (online): 978-87-7112-493-4

Published by:
Aalborg University Press
Skjernvej 4A, 2nd floor
DK – 9220 Aalborg Ø
Phone: +45 99407140
aauf@forlag.aau.dk
forlag.aau.dk

Printed in Denmark by Rosendahls, 2016

CV

The author received BSc and MSc degrees from Università degli Studi di Pavia (IT) respectively in 2008 and 2011. For his MSc thesis about optimized operation of offshore wind farms in presence of DFIG wind turbines and VSC-HVDC connection, carried out in collaboration with Vestas R&D, he received the L. Priori - Edison S.p.A. award in 2011. Since 2011 until 2013 he stayed at the Department of Energy Technology at Aalborg University (DK).

Since January 2014 until November 2015 he was R&D engineer in the Central PhotoVoltaic Inverter team of ABB DMPC PG Solar, formerly Power-One, in Valdarno (IT). During this time he was involved in the collaborations with Corporate Research Centres (CH-SE-US-CN) and with onsite researches in the field of control and integration of grid connected PV inverters. Moreover he took responsibility for development of PhotoVoltaic Inverter model portfolio (using DIgSILENT and Simulink), for grid code and patent reviewing and for the preparation and assessment of Grid Impact Studies for utility scale plants (approx. 110 MW installed in the EMEA markets). He developed the prototype of a controller for "hybrid systems" and participated to the commissioning of Gasfinolhu (MAL) microgrid. Since December 2015 he has been PowerStore specialist in ABB PG, formerly Power System Power Generation, just for its integration in microgrids. He is co-author of 5 ABB Invention Disclosures and he has 2 pending patents.

The author has interests in the modelling and control of inverters, for both grid connected and islanded operations, and in the optimized operation of renewables considering weather forecasts.

ENGLISH SUMMARY

The increasing share of Distributed Generators (DGs) poses concerns about network stability and their fair participation to the electricity market. Their aggregation in Virtual Power Plants, sometimes in combination with load prosumers, could represent an answer to these issues. Nevertheless Technical Virtual Power Plant still offer limited ancillary services, as reactive power management and spinning reserve.

Focus of this thesis is on the control of DGs for providing further and higher quality ancillary services. In particular LV dispatchable DGs, hereinafter called flexible DGs, as stationary battery units (SBUs), microturbines (MTs) and Diesel Engines (DEs) appear promising solutions.

The models of a SBU derived from a commercial Electric Vehicle battery and a MT are proposed. Both units are Voltage Source Converter (VSC) interfaced and, following recent Power Electronics state of the art, they are equipped with an LCL output filter. The thesis starts deepening the design of current control scheme for a stable operation in grid connected mode. Such flexible units offer on the other hand the possibility to survive a LV feeder in the future case of intentional islanding or for black start service. Therefore the design of the voltage regulator is developed proposing the compensation of the voltage drop on to grid side inductance. Moreover considering the hierarchical control a comparison between direct and reverse droop configurations is proposed.

The participation to local reactive power market implies the precise control of reactive power through DGs. While reactive power regulator tuning is straightforward in case of current controlled VSCs, it is more challenging in case of synchronous generator interfaced DGs, as DEs and small CHP units, due to the high system order introduced considering the electrical machines, real exciter and network equations. The analytical tuning of the same regulator is here developed starting from small signal analyses of the plant, with an approach fitting to any reactance to resistance ratio of the equivalent Thevenin model regarded for representing the network. Such time consuming tuning procedure is then compared with an automated regulator design based on multiple time domain runs driven by a Simplex Optimisation. In particular some novel objective functions relying on typical step response indexes are proposed and assessed.

The last chapter moves the research focus from DG controllers to the aggregated response of a Distribution Network (DN), highly populated by DGs, for large voltage stability system studies. Indeed while DGs dynamic reactive support and disconnection thresholds are well defined by grid codes, the overall response of the DN where they are connected is almost unknown. Just for this reason Transmission System Operators (TSOs) are used to represent a DN with an equivalent MV busbar where a handful of typical DGs and lumped loads are connected. In this chapter differently it is proposed to model part of the DN with an equivalent adaptive node, whose active and reactive power response is dependent by the voltage at the interconnection point and by main external factors affecting the response (i.e. the irradiance for a photovoltaic plant and the wind speed for a wind power plant). The proposed method is time independent and it relies on the assumption of the absence of slow dynamics in the DN to be reduced. Results are validated comparing the response of the reduced DN to the corresponding detailed model.

The overall research is carried with PSCAD®, MATLAB® and its toolboxes. This thesis was financed within the project *Development of a Secure, Economic and Environmentally-friendly Modern Power System* (SEEMPS) supported by Danish Council for Strategic Research (DSF 09-067225)

DANSK RESUME

Den øgede mængde decentrale anlæg udgør en udfordring for systemstabilitet og deltagelse på en fair måde i elmarkedet. Aggregering i virtuelle kraftværker, undertiden også kombineret med kunder, der producerer el, kan være et svar på disse udfordringer. På den anden side tilbyder sådanne virtuelle kraftværker kun systemydelser i begrænset omfang, her tænkes på eksempelvis reaktiv effektkontrol og roterende reserver.

Denne afhandling har fokus på kontrol af decentrale anlæg med henblik på at yde en bedre kvalitet systemydelser. Særligt fleksible anlæg såsom stationære batterier (SBU), mikroturbiner og dieselmaskiner fremtræder som attraktive løsninger.

Modeller af SBU er afledt fra kommercielle elbil batterier og en mikroturbine er udviklet. Begge enheder er udstyret med netinterface med voltage source converter VSC og i henhold til nutidige standarder for effektelektronik, herunder udstyret med LCL-filter. Afhandlingen lægger ud med at uddybe strøm regulering med henblik på stabil drift i nettilsluttet tilstand. Fleksible enheder kan bruges til opstart af lavspændingsnet under Ø-drift og ved opstart fra dødt net. Design af spændingsregulering er derfor udviklet til at kompensere for spændingsfald henover netinduktans. Yderligere er det overvejet at udføre en hierarkisk regulering der foretager en sammenligning med både direkte og revers droop konfigurationer.

Deltagelse i local reaktiv effektkompensering i elmarkedet nødvendiggør en præcis regulering af reaktiv effect fra decentrale anlæg. Reaktiv effektregulering er ganske ligetil når der anvendes VSC netinterface, hvorimod det er mere udfordrende når der anvendes direkte tilkoblede synkrongeneratorer som i små kraftvarmeværker. Dette skyldes det samlede systems orden er højere på grund af de elektriske maskiners dynamik, deres magnetiseringsmaskiner og netmodellering. Analytisk tuning af regulatorer er udviklet ud fra en småsignal analyse af anlæggene under anvendelse af en passende fitting (kurvetilpasning) af R/X forholdet for den ækvivalente Thevenin model, der repræsenterer nettet. Dette er tidskrævende og vil blive sammenlignet med et automatiseret regulator design baseret på multiple tidsdomæne simuleringer under anvendelse af Simplex optimering. Særlige nye objektfunktioner der baserer sig på typiske enhedsstep svar er foreslået og vurderet.

Sidste kapitel flytter det videnskabelige fokus fra de decentrale anlæg og disses regulering som enkeltenheder og til en aggregeret respons af et samlet dis-

tributionsnet DN, indeholdende mange decentrale enheder. Der udføres studier af spændingsstabilitet. Upåagtet nettilslutningsbestemmelser specificerer reaktiv effektregulering og udkoblinkskriterier for de enkelte anlæg er den samlede respons af sammensatte net/anlæg som en aggregeret enhed ikke velkendt. Derfor anvender TSO (transmissions system operatør) i dag DN som en standard samleskinne model indeholdende en standard mængde DG og belastninger. I dette kapitel foreslås at modeldanne dele af DN som et ækvivalent knudepunkt, hvis aktiv- og reaktiv effektrespons afhænger af spændingsprofilen i tilslutningspunktet og eksterne faktorer som for eksempel solintensitet og vindhastighed. Den foreslåede model er tidsuafhængig og bygger på fravær af langsom dynamik i DN, der reduceres til et ækvivalent knudepunkt. Resultaterne er valideret ved sammenligning med simuleringer af detaljerede modeller.

Resultaterne er udført under anvendelse af PSCAD, MATLAB og dennes værktøjskasser. Afhandlingen er finansieret af den Danske stat (DSF) og industrielle partnere som en del af SEEMPS projektet.

ACKNOWLEDGEMENTS

I express my sincere gratitude to my supervisor in this work, Prof. Zhe Chen, for the PhD opportunity, his kind guidance and patience.

I would like to thank Dr. Sanjay Chaudhary for fruitful and interesting discussions, the continuous support and several Skype talks even after leaving AAU. I wish him a successful career as Professor, he really deserve it! I thank Dr. Weihao Hu as well for his guidance during my stay at the Department of Energy Technology.

This thesis has been made possible thank to Prof. Claus Leth Bak for his guidance and wise recommendations, especially when I decided moving to industry but without abandoning the PhD. I want to thank as well the SEEMPS project fellows and friends, Dr. Zakir Hussain Rather, Dr. Chengxi Liu, Dr. Iker Diaz De Zerio and Dr. Mostafa Astaneh, beyond all industrial stakeholders for interesting discussions hold during the project meetings.

On the other hand I would like to thank the colleagues in ABB DMPC PG Solar and ABB CRCs. In particular I want to thank David Martini, head of R&D Central Inverter team, for fostering me going on with thesis preparation even during hard working times at the office. I am grateful to Marco Trova, head of Technical Sale team, and Antonio Rossi, EMEA Technical Sale manager, for their friendly support and for giving me opportunity to put in practice my knowledge. Likely I am now confident in my technical skills just thank to them! Moreovoer I'd like to thank Silvia, Andrea Marcianesi, Andrea Bianchi and Ettore for fruitful discussions about my thesis progresses.

Life in Aalborg was made easier, unforgettable and happier thank to Min, Chendan, Lalitta, Pia, Waruna, Coke, Quino, Juancho, Josep, Kiwoo, Christian, Yanjun, Chao, Erik, the department football team players and the overall Chinese community at the department. I cannot forget Ben&Claudia, a marvellous couple who helped me during the overall stay in Aalborg, and Vincenzo and Samuel for friendly Italian talks and dinners!

Thousands of kilometres of distance have never made me feel far away from "old friends" Hilly, Anny, Miriam, Maria, Luigi, Michele, Massi and Matteo: thank you very much!

Last but not the least I want thanking my mum, Massimo and Daniele, for continuous support, the patient and long lasting Skype calls during my stay in Aalborg.

Mantova, 28th September 2015

CONTENTS

Chapter 1 Introduction 1

1.1 Background and motivations 1

1.2 Main contributions of the thesis 3

1.3 Limitations 4

1.4 Softwares choice 4

1.5 Outline of the thesis 5

1.6 Publications 6

Chapter 2 State of the art 7

2.1 The role of LV flexible units 7

2.1.1 Intentional islanding and grid codes 8

2.1.2 VSC control modes 8

2.1.3 Unit modelling for integration studies 9

2.2 Reduction methods for large voltage stability analyses 11

Chapter 3 VSC modelling, design and controls 13

3.1 Converter models for transient simulations 13

3.2 Grid filter design and DC link rating 18

3.3 Controllers design 24

3.3.1 Principle of cascaded loops 24

3.3.2 Grid current regulator 25

3.3.3 Power control 29

3.3.4 Grid voltage regulator 29

3.4 Conclusions 35

Chapter 4 VSC interfaced LV flexible units 37

4.1 DG modelling 37

4.1.1 Microturbine modelling 38

4.1.2 Stationary battery model 41
4.2 Hierarchical control applications 44
4.2.1 Hierarchical control schemes 46
4.2.2 Intentional islanding 53
4.3 Conclusions 58
Chapter 5 Reactive power controller for distributed synchronous generators .61
5.1 Reactive power controller 62
5.2 Machine equations 65
5.2.1 Synchronous generator equations 65
5.2.2 AC5A exciter 68
5.3 Infinite bus system – steady state equations 69
5.4 Small signal analyses 71
5.5 Validation of small signal models 76
5.6 Nelder and Mead Simplex Optimization 81
5.7 Pole assignment method 86
5.8 Conclusions 89
Chapter 6 A reduction method for radial active distribution networks.....91
6.1 Problem description 91
6.2 The concept 92
6.3 Case study 94
6.3.1 Load models 94
6.3.2 Wind Turbine 95
6.3.3 PhotoVoltaic Plant 97
6.3.4 Methodological notes and mapping results 98
6.3.5 Results 101
6.4 Conclusions 104
Chapter 7 Conclusions and future work 107
7.1 Conclusions 107

7.2 Future work 109

References 111

Appendices 123

LIST OF ACRONYMS

BU	Battery Unit
B2B	Back-to-Back converter
CB	Circuit Breaker
DER	Distributed Energy Resource
DRCS	Dynamic Reactive Current Support
DSO	Distribution System Operator
DE	Diesel Engine
DG	Distributed Generator
DN	Distribution Network
GT	Gas Turbine
EMT	Electro Magnetic Transient
EV	Electric Vehicle
GSC	Grid Side Converter
KCL	Kirchoff's Current Law
KVL	Kirchoff's Voltage Law
LVRT	Low Voltage Ride Through
MG	Microgrid
MSC	Machine Side Converter
MT	Microturbine
OF	Objective Function
OFPC	Over Frequency Power Curtailment
OLTC	On Load Tap changer
PCC	Point of Common Coupling
PMSG	Permanent Magnet Synchronous Generator
PV	PhotoVoltaic
PVP	PhotoVoltaic Plant
SBU	Stationary Battery Unit
SLD	Single Line Diagram
TSO	Transmission System Operator
UFLS	Under Frequency Load Shedding
VSC	Voltage Source Converter
V2G	Vehicle To Grid
WT	Wind Turbine

LIST OF FIGURES

Figure 2-1: MT conceptual control scheme. 9

Figure 2-2: network reduction terminology. 11

Figure 3-1: detailed two-level inverter. 14

Figure 3-2: switching function represented inverter. 15

Figure 3-3: network scheme. 16

Figure 3-4: voltage and current profiles for different representations of floating DC link inverter 16

Figure 3-5: voltage and current profiles for DC split link inverter representations. 17

Figure 3-6: average inverter model. 17

Figure 3-7: nomenclature scheme. 19

Figure 3-8: phasor diagram representing KVL at the output filter. 20

Figure 3-9: overall output filter inductance and DC link voltage as function of the nominal unit power, in case of $V_g = 400V$ 21

Figure 3-10: exact transfer function of the plant to be considered for the current controller. 23

Figure 3-11: LCL current attenuation. 24

Figure 3-12: overall control scheme. 25

Figure 3-13: overall control scheme. Alternative solutions: current sensor at the inverter side, in red, and current sensor at the grid side, in blue. 26

Figure 3-14: current open loop transfer functions, assuming same regulator gains. 28

Figure 3-15: current closed loop transfer functions, assuming same regulator gains. 28

Figure 3-16: control scheme of a voltage controlled VSC using an LCL. 30

Figure 3-17: Bode plots representing the current open loop transfer function and the main steps leading to the regulator design. 31

Figure 3-18: Bode plots of the current closed loop transfer function. 31

Figure 3-19: Bode plots representing the open loop transfer function of the voltage regulator. 32

Figure 3-20: Thevenin equivalent of voltage controlled VSC. 33

Figure 3-21: Bode plots representing the closed loop transfer function of the voltage loop and the output impedance. 34

Figure 3-22: voltage drop compensation at the fundamental and overall control scheme structure (continuous arrows define dq components buses while dashed segments the single components). 34

Figure 3-23: summary flow chart for the automatic design of the VSC. 36

Figure 4-1: Microturbine conceptual scheme (© 2013 IEEE). 38

Figure 4-2: microturbine response to active power steps. 40

Figure 4-3: battery model (© 2013 IEEE). 42

Figure 4-4: 3D look-up table process definition, (a) manufacturer discharge characteristics, (b) and (c) curve processment, (d) representation of resulting 3D look-up table (© 2013 IEEE). 42

Figure 4-5: battery unit test (© 2013 IEEE). 43

Figure 4-6: Battery models comparison (© 2013 IEEE). 44

Figure 4-7: single-phase equivalent of a line. 44

Figure 4-8: direct droop control block diagram based on phase angle bias. 47

Figure 4-9: direct droop control block diagram based on frequency bias. 47

Figure 4-10: inverse droop control block diagram. 48

Figure 4-11: microgrid Single Line Diagram. 49

Figure 4-12: direct droop profiles, considering phase angle bias droop. 50

Figure 4-13:direct droop profiles, considering frequency bias droop. 50

Figure 4-14: inverse droop profiles. 51

Figure 4-15: enlargement of reactive power profiles in the direct droop control case based on angle bias. 52

Figure 4-16: phase to ground voltage profiles in the phase angle droop scenario shown in Figure 4-12. 52

Figure 4-17: secondary control for direct droop control scheme with phase angle bias. 54

Figure 4-18: power control scheme for a voltage source unit. 54

Figure 4-19: Single Line Diagram of modified C6.04.02 residential feeder. 56

Figure 4-20: comparison of flexible DGs control schemes in case of intentional islanding consequent to UFLS. Transition to islanded mode with direct drooped DGs on the left and with inverse drooped DGs on the right. 57

Figure 4-21: effect of derivative term on the battery unit voltage regulator in the inverse droop scheme (© 2013 IEEE). 58

Figure 5-1: conceptual control scheme (© 2016 IEEE). 62

Figure 5-2: infinite bus system: radial distribution network on the left and its Thevenin equivalent on the right. 62

Figure 5-3: $E_t\big|_{P_{tB}=0.5\,p.u.;Q_{tB}=0.1\,p.u}$ 64

Figure 5-4: $\varphi_t\big|_{P_{tB}=0.5\,p.u.;Q_{tB}=0.1\,p.u}$ 64

Figure 5-5: $\left.\frac{\partial P_{tB}}{\partial E_t}\right|_{P_{tB}=0.5\,p.u.;Q_{tB}=0.1\,p.u}$ 64

Figure 5-6: $\left.\frac{\partial Q_{tB}}{\partial E_t}\right|_{P_{tB}=0.5\,p.u.;Q_{tB}=0.1\,p.u}$ 64

Figure 5-7: simplified synchronous generator model. 65

Figure 5-8: d and q axis equivalent circuits. 67

Figure 5-9: AC5A control scheme (on the left) and equivalents (on the right). 68

Figure 5-10: phasor diagram (© 2016 IEEE). 70

Figure 5-11: “traditional” K-parameter model (© 2016 IEEE). 73

Figure 5-12: "extended" K-parameter model, proposed part outlined in green. 75

Figure 5-13: ΔV=0.02 p.u. step response, starting from P=0.5 p.u. and Q=0.1 p.u in the scenarios X/R=5, on the left, and X/R=1.37, on the right (© 2016 IEEE). 77

Figure 5-14: zero-pole map of closed loop transfer function $G_{CL}^{V}(s)$ in case X/R=1.37 (enlargement). 78

Figure 5-15: unit step response in X/R=1.37 scenario.....78

Figure 5-16: ΔQ=0.1 p.u. step response, starting from P=0.5 p.u. and Q=0.1 p.u in the scenarios X/R=5, on the left, and X/R=1.37, on the right (© 2016 IEEE).79

Figure 5-17: comparison of analytical and identified reactive power closed loop transfer functions. 80

Figure 5-18: runtime detectors for rise time (a), settling time (b) and overshoot (c) (© 2016 IEEE). 83

Figure 5-19: summary results referred to OF_1 (© 2016 IEEE). 84

Figure 5-20: summary results referred to OF_2 (© 2016 IEEE). 84

Figure 5-21: results referred to the objective function(5.65), formulated as $OF(k_p, \frac{1}{k_i})$ 86

Figure 5-22: relation between CIs and zero pole map in presence of dominant complex conjugate poles. 87

Figure 5-23: poles and zeros map of the plant (enlargement). 88

Figure 5-24: closed loop step response (a) and enlargement of pole-zero map with geometrical limits considering a second order closed loop transfer function (b) (© 2016 IEEE). 88

Figure 5-25: Step response comparison of same system considering different sets of reactive power regulator parameters (© 2016 IEEE). 89

Figure 6-1: reduction of the external radial susbsystem in an equivalent dynamic PQ node. 92

Figure 6-2: mapping procedure. 93

Figure 6-3: PSCAD® SLD of simplified Støvring network. The DN to be reduced is red outlined (© 2013 IEEE). 94

Figure 6-4: type 4, pitch controlled, wind turbine scheme (© 2013 IEEE). 96

Figure 6-5: Grid Side Converter control scheme (© 2013 IEEE).....97

Figure 6-6: rotational speed control.....97

Figure 6-7: PhotoVoltaic unit control scheme (© 2013 IEEE).....98

Figure 6-8: photovoltaic plant characteristic (© 2013 IEEE). 99

Figure 6-9: active power meshes as function of voltage at the aggregation node and wind speed, considering no EVs in charging mode and constant impedance loads. No and high irradiance scenarios, respectively G=0 W/m2 and G=1000 W/m2 (a and b). Enlargements of mesh slope variations due to WT disconnection in case of wind stronger than cut-off speed (c) and PV plant disconnection for LVRT (d). 100

Figure 6-10: characteristics of the aggregated distribution network assuming base power 10 MVA (© 2013 IEEE). 101

Figure 6-11: PSCAD® representation of the power system with the aggregated distribution network (© 2013 IEEE). 101

Figure 6-12: comparison in the same scenario. Voltage (a), active and reactive power (b and c) at the retained node. The enlargements of fault transients, highlighted with grey boxes are proposed on the right for a detailed comparison (© 2013 IEEE)..... 102

Figure 6-13: photovoltaic plant response to the fault (base power 250 kVA) (© 2013 IEEE). 103

Figure 6-14: wind turbine response to the fault (base power 1.5 MVA) (© 2013 IEEE). 104

Figure A-1: dominant pole location and relation with natural pulsation and damping factor 3

Figure A-2: Rowen model neglecting the exhaust temperature controller 5

Figure A-3: block scheme reduction process. 6

Figure A-4: labelling according to Mason's rule. 7

LIST OF TABLES

Table 1-1: thesis limitations. 4

Table 2-1: summary about MT publications. 10

Table 3-1: simulation times in case of different models of floating DC link inverter. 18

Table 3-2: VSC parameters and design specifications. 21

Table 3-3: LCL parameters. 21

Table 3-4: current regulator parameters for grid connected VSC. 26

Table 3-5: current regulator parameters for voltage controlled VSC. 30

Table 3-6: voltage regulator parameters for voltage controlled VSC. 32

Table 4-1: MicroTurbine parameters. 39

Table 4-2: nominal values and droop parameters. 49

Table 4-3: droop parameters. 49

Table 4-4: power regulator parameters. 55

Table 5-1: closed loop transfer function characteristics. 78

Table 5-2: optimisation references 83

Table 5-3: weighting factor and optimisation tolerance values 84

Table 5-4: closed loop transfer function characteristics. 87

Table 6-1. external factors regarded for the mapping process 99

Table A-1: Grid characteristics at the Point of Common Coupling. 9

Table A-2: Synchronous Generator and shaft data 9

Table A-3: AC5A parameters. 9

Table A-4: measurement smoothing constants. 9

CHAPTER 1

INTRODUCTION

1.1 BACKGROUND AND MOTIVATIONS

In the last decade the pace of installation of renewables has been increasing worldwide. Mainly for environmental concerns the European Commission set an energy consumption target of 20% from renewables by 2020 and 27% within 2030. On the other hand scale economies are making cheaper renewables technologies. In this scenario the relentless transition from centralized to decentralized generation appears firm [1]. Such a paradigm shift is certainly beneficial from the environmental point of view but it poses concerns about to the security and cost sustainability of the power systems. Higher share of independent Distributed Generators (DGs) can have negative impact mainly due to [2]:

- Reduced system stability;
- Power quality issues, as:
    - Voltage flicker (common for wind power either under normal and for switching operations, or due to energization of step-up transformers);
    - Harmonics, due to the combination of DGs and exacerbated by underground cables;
    - Voltage unbalances, due to single phase DGs;
- Multidirectional power flow in distribution networks;
- Power production volatility due to renewables;
- Risk of unwanted islanding operation;
- Reduced margin of overloading and lack of inertia due Voltage Source Converter (VSC) interfaced DGs;
- Lack of coordinated control among DGs for operating grid black start; Reduced provision of primary regulations by renewable based DGs, traditionally operating at MPPT or close to it;

On the other hand Distributed Generators (DGs) could offer new benefits like:

- increasing the overall conversion efficiency;
- meeting the load demand on site, which implies:

- combining electrical and thermal load requirements;
- possibility to intentionally operate in islanded mode;
- increased possibility to perform voltage regulation, either under normal operation and during fault, through Dynamic Reactive Current Support (DRCS);

In order to aggregate DGs and loads the concept of Virtual Power Plant was coined [3] in the first decade of the century. In a nutshell the units are going to be clustered and managed in order to appear as a single player either for energy auctions and/or for provision of ancillary services. These functions respectively differentiate Commercial and Technical Virtual Power Plants (respectively CVVP and TVPP) [3]. Large demonstration project funded by EU (ADINE, FENIX [4] and PowerMatcher [5]) witnessed the benefits of the VPPs. Nevertheless TVPPs remained limited to a couple of ancillary services, such as voltage regulation for normal operation and provision of spinning reserve. With reference to the latter Flexitricity [6] foresaw the potential of stand-by DGs, hereinafter defined as flexible DGs; a function later included in a recent release of the PowerMatcher [5].

On the other hand since early 2000, control and power electronics engineers have been pioneering the Microgrid (MG) sector [7-11]. According to the first definition [7] a MG is "a cluster of loads and microsources operating as a single controllable system that provides both power and heat to its local area". The MG term however started soon referring only an electrical system that can be operated in islanded mode and eventually even in grid connected one. In IEEE-1547.4 [12] the MGs have been associated to a "distributed resources (DRs) island systems" that "are a part of electric power system that have DR and load, have the ability to disconnect from and parallel with the EPS". In practice, the feasibility of intentional islanding remains however negligible due to unwillingness of TSOs and DSOs and as such, nowadays is limited to sensitive areas (as hospitals and military campuses). It must be noted that UPS regulations differ from normal grid connected units.

Amid this scenario manufacturers have been striving to ensure the compliance of DGs to new standards and grid codes. Nevertheless the market drivers remained electricity costs, subsidies and specific tariffs. Such schemes however don't award yet voltage regulation at distribution level, featured by poor reactance to resistance ratios, and intentional islanding. Nevertheless the presence of stand-by generators, frequently VSC interfaced, and the incoming diffusion of Stationary Battery Units (SBUs) for residential peak shifting could open the market opportunity to tap such ancillary services.

In this thesis the control issues allowing such functionalities are addressed. It is worth to mention that this thesis represents the fifth work package of "Development of a Secure, Economic and Environmentally-friendly Modern power System" (SEEMPS) project led by Prof. Zhe Chen at AAU. The project, kicked off in 2010, has been possible thanks to a 23.4 millions DKK (approx 3.1 M€) funding provided by the Danish Strategic Fund and industrial partners (kk-electronics, ALSTOM, Energinet.dk, DONG Energy and HEF).

1.2 MAIN CONTRIBUTIONS OF THE THESIS

Given the background described in section 1.1, this thesis tackles below mentioned problems:

- Analytical design of a passive damped LCL filter for the universal operation of a VSC interfaced unit both in current and voltage control modes. The study investigates the effect of the grid impedance variations and the current sensor position in depth. Moreover the Thevenin equivalent of such type of voltage control unit is provided.

- Providing the guidelines for VSC modelling for transient simulations;

- Enhanced operation of a residential feeder of a Distribution Network (DN) through flexible VSC interfaced LV DGs. In this framework two models for power system simulations are proposed. Moreover the comparison of following VSC controls for islanded operation is also provided:

    - direct droop with angle bias;

    - direct droop with frequency bias;

    - reverse droop;

- The control of reactive power through synchronous generators is well known however literature indicates that there is a lack of any analytical treatise of the reactive power regulator tuning. Traditional K parameter model is applied in case of AC5A exciter model and it was proofed that such AVR model leads to a steady state voltage regulation. On the base of this and extending the small signal analyse two plant transfer functions for the reactive power regulator are presented and validated. Given the high complexity of aforementioned method, the tuning is performed also through Simplex based multiple simulations proposing novel Objective Functions (OFs) based on runtime tracked Characteristic Indexes;

- A first answer to the presence of DGs contributing to dynamic simulations, including the effects of weather dependant sources and their contributions to the dynamic reactive current support throughout the DNs could be the

aggregation of distribution MV feeders. In this thesis a novel aggregation method based on multidimensional data structure is given.

1.3 LIMITATIONS

The limitations to this work are listed in Table 1-1.

Table 1-1: thesis limitations.

Chapter number	*Limitation*
3	▪ The design of VSC output filter doesn't cover the magnetic study as well the optimization of the filter parameters;
4	▪ The performance of the proposed Li-Ion battery model and MT are not validated by lab tests; ▪ The same VSC model was considered for all LV flexible LV units; ▪ An islanding signal is supposed to be dispatched to the flexible DGs, without taking into account any communication delay; ▪ In the simulations all DGs are neither performing anti-islanding nor providing ancillary services; ▪ Droop parameters are calculated without performing specific stability studies; ▪ The impedance angle of the equivalent grid is supposed to be known, no grid impedance estimation methods are considered, as well as the interaction with the inverter output impedance;
5	▪ Both proposed tuning methods are made taking into account a single line equivalent system;
6	▪ Proposed method fits only to symmetrical network conditions; ▪ All the loads are represented through the exponential equation; ▪ WT rotor inertia as well as possible frequency variations are disregarded for obtaining the equivalent network;

1.4 SOFTWARES CHOICE

All time domain simulations are carried out using PSCAD®. This simulation tool allows running EMT simulations and it offers a wide library of power electronic and power system devices, in addition to main automation, logic and control functions. Moreover the designer can define customized components through FORTRAN programming language. The assessment of the SBU is made comparing the performances of proposed model implemented in PSCAD®, with the battery model included in Simulink-SimPowerSystem [13] library. The overall MATLAB® has been used broadly for:

- Handling the data series and performing interpolations;
- Scripting;
- Obtain homogeneous quality and formatting of all the plots and meshes presented in the thesis figures;

Moreover following MATLAB® toolboxes have been used:

- Symbolic Math Toolbox [14], in particular through MuPAD interface, for expliciting the closed loop form of all the transfer functions and for solv-

ing numerically the power flow equations, necessary for both PSCAD® initializations and definition of the starting point of in the small signal model analyses. Moreover it allows computing symbolically the transfer functions of complex control bock diagrams applying Mason's rule;

- Control System Toolbox [15], for handling transfer functions, recognizing poles and zeros, as well as plotting root locus, Bode plots and step responses;

- System Identification Toolbox [16], limited to the validation of developed small signal models in Chapter 5.

1.5 OUTLINE OF THE THESIS

The thesis is organized as follows:

- Chapter 1 gives an introduction of the overall work, summarizing the main contributions, limitations and the software choice;

- Chapter 2 reports specifically the state of the art regarding all the topics dealt throughout the thesis;

- Chapter 3 proposes through analytical analyses the design of the VSC, including LCL output filter, bulk rating design, converter modelling. Important topics such as the influence of current sensor position, approximation of the current loop plant transfer function, effects of grid impedance for current controlled VSC and the compensation of the voltage drop along the grid side inductance in voltage controlled mode are addressed. Moreover the closed loop form of the current and voltage regulators are proposed;

- Chapter 4 deals with the modelling of VSC interfaced LV flexible units and their control for coping islanded distribution feeders. The performance of a Microtubine (MT) model are assessed, moreover a novel Li-Ion battery model is presented and tested. The hierarchical control is presented, with particular reference to the use of the decoupling matrix. A comparison between direct, either based on angle and frequency biases, or reverse droop control scheme is presented, highlighting the reason why latter control scheme is traditionally disregarded for voltage controlled units. The comparison is carried out initially considering a simple two sources fed MG under different load scenarios and in a second stage considering the intentional islanding of a more complex network, as the residential feeder of CIGRE benchmark network;

- Chapter 5 covers the control of reactive power dispatched by a synchronous generator. In particular the effects of the grid impedance on the regulation are discussed. Thereafter two alternative approaches for the regulator tuning are presented and compared. The first relies on the selection of regula-

tor parameters through optimized multiple time domain simulations, while the second is based on the small signal analyses of synchronous generator, exciter and power flow equations;

- Chapter 6 proposes an innovative reduction method suitable for radial active distribution networks populated by VSC interfaced DGs. The method is validated through the comparison of the response of the detailed network with the same network including the equivalent, in case of fault occurring in the internal subsystem;

- Chapter 7 includes the overall conclusions and proposals for a future work.

The thesis includes the list of references and a final appendix, intended by the author as a collection of specific demonstrations, list of data and a control scheme, useful for the comprehension of the work but not strictly fitting to formerly described chapters.

Presented outline does not reflect completely the workflow of the PhD study. During his time at AAU the author supervised two MSc students in their final thesis. That work deepened the modelling and control of a DC MG but it is not included in this text. Several further researches were carried out by the author in his positions as R&D Engineer initially at ABB DMPC Solar and more recently in ABB Power Grids, respectively in the fields of control and integration of PV inverters and storages in DNs and MGs, but they are not disclosed in the thesis for IP reasons.

1.6 PUBLICATIONS

- M. Martino, Y. F. Quinones, P. Raboni, and Z. Chen, "Intelligent control for a DC micro-grid system," in *Universities Power Engineering Conference (UPEC), 2012 47th International*, London, 2012, pp. 1-5.
- P. Raboni and Z. Chen, "Reduction method for active distribution networks," in *PowerTech (POWERTECH), 2013 IEEE*, Grenoble, 2013, pp. 1-6.
- P. Raboni, H. Weihao, S. K. Chaudhary, and Z. Chen, "Modeling and control of low voltage flexible units for enhanced operation of distribution feeders," in *Industrial Electronics Society, IECON 2013 - 39th Annual Conference of the IEEE*, Wien, 2013, pp. 7469-7474.
- P. Raboni, S. K. Chaudhary, Z. Chen, “Design of Reactive Power Regulator for Synchronous Generator assigned Characteristic Index Objectives and considering the Grid Impedance Angle,” IET Generation Transmission and Distribution (submitted in January 2016).

CHAPTER 2

STATE OF THE ART

2.1 THE ROLE OF LV FLEXIBLE UNITS

While the intermittency of renewables is difficult to predict there are some DGs, rated no more than few hundreds of kilowatts, that turn out dispatchable, as well as conventional power plants. They are even featured by fast ramp rate, which makes them ideal for providing spinning reserve. In this thesis microturbines (MTs), stationary battery units (SBUs) and Diesel Engines (DEs) are considered. It must be noted that while MT and SBU are VSC interfaced, DEs makes use of synchronous generators.

MTs are traditionally exploited as Combined Heat and Power units, featured by good efficiencies ($\eta_{El}\approx28\%$ and $\eta_{Th}\approx44\%$), the latter in the form of hot water at 90 °C [8]. They are typically heat-led controlled and offer large flexibility both in terms of admitted fuels [9] and operation at partial loading (constant efficiency from 45% up to the nominal power [10]).

SBU can be represented by stationary batteries, both stand alone and in combination with renewables. In this thesis the Vehicle to Grid concept is not regarded even if it could offer same type of ancillary services to the grid. SBU indeed appears the preferred solution by industries which at the time of the thesis publication have just announced some industrial products. ABB PowerStore [17] is a flexible inverter that can be connected to different types of storages. ABB REACT [18] is single phase product combining a PV unit and a Li-Ion storage just for load shifting and stand alone feeding of households loads in case of black-out. Tesla PowerWall [19] instead is a real household storage but it interfaces only through the DC side of a PV inverter for peak shifting purposes. On the other hand latter product confirms the validity of the choice made in this thesis about the usage of a vehicle battery for stationary applications.

High operating costs of DEs make them a viable solution for certain CHP applications or whenever a grid forming unit is needed, as for back-up applications (UPS) and in networks operated in islanded mode. On the other hand the presence of a

synchronous generator offer certainly advantages in terms of transient overload respect to MTs and BUs.

2.1.1 INTENTIONAL ISLANDING AND GRID CODES

The transition to Active Low Voltage Distribution Networks gives rise to the scenario of intentional islanding [12] in case of disturbance in the main grid. As already mentioned IEEE 1547.4 is a standard providing guidelines for islanded operation of DGs and DNs. So far however neither grid codes nor utilities allow such operating mode, unless the unit complies with UPS requirements. On the contrary all DGs must pass the Anti-Islanding (AI) tests, whose procedures are clearly described for example in [20, 21]. Depending on the grid code regulations, the AI method and the number of parallel DGs, the maximum allowed disconnection time varies between 0.5 s and 5 s.

2.1.2 VSC CONTROL MODES

Voltage Source Converters are the standard interface for DGs. For grid connected operation they are typically current controlled, since the grid voltage is supposed to be stiff. The power flow through the equivalent series filter inductance indeed can be easily controlled, acting on the amplitude and phase displacement of the inverter fundamental voltage. Such feature doesn't hold anymore in islanded mode, in particular in absence of a grid forming unit, where the VSC control must pass to voltage control mode. Nevertheless an inner current loop can be maintained in order to improve the rejection to the current perturbations. It must be noted that voltage control well fit to flexible units while it poorly adapts to MPPT based renewables. Either in the case of current and voltage controls harmonic current compensation loops can be added. Application of three wire VSCs eases the control since there cannot be homopolar component, reducing the number of variable components to two. In particular the control can be performed either in the rotating reference frame, through the Park transformation, or in the stationary frame, through Clark transformation.

The parallel operation of VSCs in islanded mode is made possible by power sharing method, as known since first VSC interfaced UPS [22-26]. Nowadays the hierarchical control [27] appears as the standard method, due to its reliability and high decentralized principle. It is based on the well known frequency and voltage regulation schemes developed for power systems [27]. Through the primary control the autonomous power sharing among the units is achieved through droop regulation. With the secondary control instead the restoration of nominal voltage and frequency values is obtained. This control layer can operate both with a single unit or through a cluster of properly coordinated units [28]. Power sharing on the other hand relies on

the power flow equations, in particular the assumption of mainly inductive transmission lines led the power system engineers to traditional P-f and Q-V droops. Such assumption is not anymore valid in case of islanded LV distribution networks, where transformers and long overhead lines are absent, unless the output impedance of the inverter is highly inductive. The effect of the Equivalent Series Resistor on the output filter inductors could add a further degree of variability that jeopardize the droop typology. Also for this reason a widespread solution is using a virtual impedance [29, 30], in order to shape the output impedance of the inverter. If it is represented by a virtual inductor [29-31], the traditional droops can be maintained. However in case of harmonic loads, high THD is observed, unless adopting further solutions like a high pass filter on the current feeding the virtual inductor [29]. Alternatively setting a virtual resistor allows adopting reversed droops [32]. For real cases with unknown and variable reactance to resistance ratio, an adaptable virtual impedance is proposed in [33]. Alternatively the equivalent network impedance can be taken into account implementing an orthogonal linear transformation to the powers [34]. This approach has been followed by [35] but the equivalent network impedance information is required. On the other hand [36] proposed to maintain the hierarchical control in islanded mode through the cooperation of grid supporting VSI based units. This solution, defined inverse droop, in opposition to the traditional direct droop, relies on external voltage and frequency regulators and an inner current one.

2.1.3 UNIT MODELLING FOR INTEGRATION STUDIES

This thesis primarily focus on the effect of unit controls for their integration in the modern power system. From this perspective an outlook of the generators model is given. As anticipated both MT and EVB are VSC interfaced and their control functionalities from a power system point of view just depends by the Machine Side Converter (MSC) control. In this paragraph the state of the art about unit modelling is given.

A broad literature is nowadays available about MT modelling and a review is proposed in [37]. On the other hand only little info is made available by MT manufacturers (f.e. Capstone, Turbec, Honeywell, ABB).

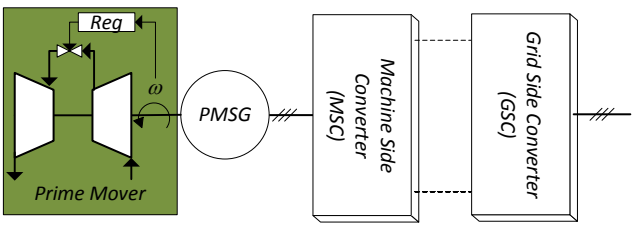

Figure 2-1: MT conceptual control scheme.

Table 2-1: summary about MT publications.

Thesis reference	Reference machine		Regulat.		Prime mover model					MSC			Simulation software		
	Manufacturer (model)	P_n [kW]	Grid following	Grid forming	1st order system	Rowen [38]	GAST[38]	Approx. th. laws	Detailed th. laws	Passive rectifier (diodes)	Active rectifier (SCRs)	Active rectifier (VSC)	DIgSILENT®	MATLAB® Simulink	PSCAD®
[39]		100							x						
[40]	Turbec (T100)	100	x	x					x						
[41]			x		x					x					
[42]		105	x	x	x						x		x		
[43]	Honeywell	200	x		x							x			x
[44]				x		x				x				x	
[45]		400		x		x				x					x
[46]		30		x		x				x				x	
[47]	Capstone (C60)	60	x	x		x						x			x
[48]		150	x	x			x							x	
[49]		60		x		x				x				x	
[50]		50	x	x		x				x					x
[51]		30	x	x		x				x					x
[52]		100	x	x				x			x				x
[53]	Capstone (C60)	60	x					x							x
[54]			x			x						x		x	
[55]	Capstone (C30)	28	x			x						x		x	

With reference to the conceptual scheme in Figure 2-1 a specific survey about MT models is given in Table 2-1, reporting whenever possible the industrial product taken into account for the research.

The overview shed light on the absence of specific MT prime mover models for integration studies. Some authors proposed detailed thermodynamic studies, not suitable for Power System studies. Latter consideration prompted most of the designer adopting the Rowen model, reported in appendix A.3, developed years earlier

for larger gas turbine units [38]. Evidently this choice doesn't allow conducting specific studies about the power ramp rate of this unit. The MSC structure is broadly debated, even if the adoption of a diode rectifier appears the most common solution.

Literature on the other hand proposed some dedicated models for the integration of battery storages in power systems, both as SBUs and V2G applications. Electro-Chemical models for obvious reason do not suit to these studies, for which is necessary adopting an equivalent model. In [56] a model identification method for Lead-Acid batteries was firstly proposed. This method takes into account both nonlinear battery behaviour and not ideal charging efficiency. On the other hand the definition of model parameters is not possible starting from common manufacturers datasheets. This need prompted [57] proposing a simpler model, defining a State Of Charge dependant Thevenin equivalent, later included in SimPowerSystem library [13]. Latter however is featured by a constant internal resistance and Thevenin source is modelled through an exponential curve. Further studies about the parameter estimation are made in [13]. In [14] a model is developed on the basis of a standard discharge curve and the assumption of homothetic discharge curves for non-standard current values.

2.2 REDUCTION METHODS FOR LARGE VOLTAGE STABILITY ANALYSES

Network reduction has been a widely analysed topic in power systems in the past when engineers had to deal transmission system simulation with limited computational resources. Nowadays those methods turn out useful for grid operators in order to avoid disclosing their network details to neighbouring operators.

Traditionally the part of the network that is going to be represented with an equivalent is defined as external subsystem. On the contrary the remaining part of the grid, which maintains its model, is defined as internal subsystem [58]. Those subsystem share so called boundary nodes as shown in Figure 2-2.

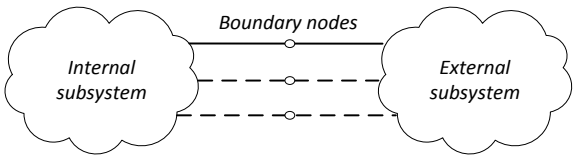

Figure 2-2: network reduction terminology.

The reduction can take place through one or the combination of the following methods:

- Physical reductions, leading to a more or less detailed representation of system elements, depending its influence on the system behaviour in response to a predefined perturbation;
- Topological reduction, leading to an elimination and aggregation of nodes;
- Modal reductions, relying on linearized models, aiming to delete or neglect insignificant system modes.

Ward method, belonging to the topological reduction class, eliminates the nodes of the external subsystem through manipulation of the admittance matrix. Nevertheless it relies on the assumption of constant impedance loads not realistic for transient studies. Reference [59] considered voltage dependant loads and proposed a method based on linearized multiple power flows. However this implies updating the base case whenever the linearization error becomes too large. Zhukov method is the most known aggregation technique and it allows reducing a set of nodes to a fictitious equivalent one, featured by a power flow equivalent to the algebraic sum of the powers exchanged between the external retained network and the nodes to be aggregated. To be noted that this method works for a system state and cannot be straightforward extended to transients studies. Just this property however led to formulate the identification coherency method [60] and [61]. A set of synchronous generators having similar rotor angle deviation in case of system perturbation can be grouped and reduced to a single machine with a good approximation in the results. Since the 1990's commercial software DYNRED® performs network reductions using the last method. More recently instead the interest respect to the reduction has grown for wind power plants featured by large amount of turbines [62] or for the aggregated response of Technical Virtual Power Plants [3]. But so far only [63] applied the coherency method for the aggregation of DN in presence of various synchronous generators.

CHAPTER 3

VSC MODELLING, DESIGN AND CONTROLS

This chapter provides an analytical background to modelling, design and control of Voltage Source Converters for distributed generators, with the aim of fully describing power electronics and control details useful for the comprehension of the rest of the thesis. In particular this chapter is a preparatory background for the design of VSC interfaced LV Flexible DGs described in chapter 4.

The first paragraph is focused on VSC modelling and it is highly recommended for defining the best model fitting to the purpose of the simulation. The design of LCL filter and DC bulk voltage choice follow, on the base of well known literature. In this treatise the robustness of a passive damped LCL filter respect to the grid impedance variations is deepened. The control of the VSC is widely described in the third paragraph, starting from the principles of cascaded loops. Both current and voltage controlled VSCs are presented, describing pros and cons of an LCL filter for such applications. The overall chapter is analytically structured: each solution starts with the definition of the corresponding control scheme, the analytical definition of the plant transfer function, along with the regulator synthesis given the representations of both open and closed loop transfer functions. Such an approach is reflected in a MATLAB® script, as reported in the conclusion, which essentially allows designing of any type of LCL filter and the VSC regulators given main specifics.

3.1 CONVERTER MODELS FOR TRANSIENT SIMULATIONS

Nowadays more and more VSCs are deployed in the power systems. Some VSC models have been developed in recent years with the aim of speeding up power system simulations. Nowadays following models are known for EMT simulations:

- *Detailed semiconductor models;*
- *Switching function models;*
- *Average models;*

At the time of this thesis publication latest SimPowerSystem release [13] easily allows switching from one type to another. In this paragraph however are shown the features of all designed models in PSCAD®, applied throughout the thesis, focusing on the computation time and the effects of grounding status. In particular the two-level inverter,is considered, whose topology is shown in Figure 3-1, with a *detailed semiconductor model representation*:

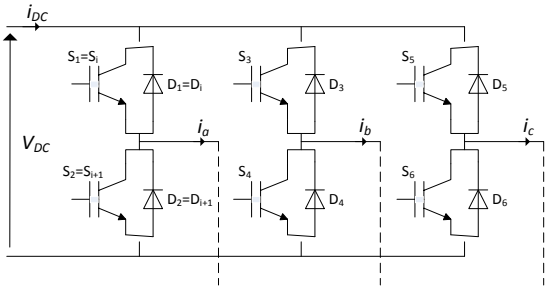

Figure 3-1: detailed two-level inverter.

For studies where loss evaluation and harmonic analyses is not of interest the VSC can be represented with a *switching functions model* [64]. With reference to the topology shown in Figure 3-1 and known that the gate signals of the semiconductor switches belonging to the same leg are complementary:

$$g_j = \overline{g_{j+1}} \tag{3.1}$$

Where:

$$\begin{aligned} j &= \{1,3,5\} \\ g_j &= \{0,1\} \end{aligned} \tag{3.2}$$

A switching function model as shown in Figure 3-2 can be developed, where:

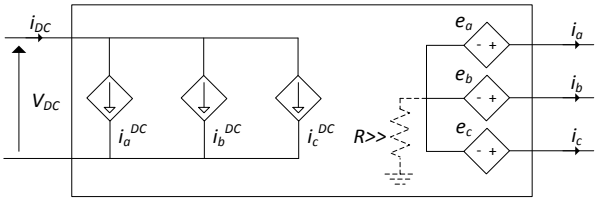

Figure 3-2: switching function represented inverter.

$$e_i = V_{DC}\left(g_i - \frac{1}{2}\right) \tag{3.3}$$

$$i_i^{DC} = i_i\left(2g_i - 1\right) \tag{3.4}$$

Where:

$$i = \left\{1 \Leftrightarrow a, 2 \Leftrightarrow b, 3 \Leftrightarrow c\right\} \tag{3.5}$$

In case of balanced currents and straightforward from (3.4) is:

$$i^{DC} = \sum i_i^{DC} = 2\sum g_i i_i \tag{3.6}$$

Since in this model DC and AC electrical circuits are completely split, particular care should be taken respect to the grounding or to specifically designed recirculation paths between DC and AC sides. Considering solidly grounded networks, as LV ones, and transformerless inverters two scenarios can show up represented. Traditionally the DC side of the inverter is kept floating, like in commercial PV inverters, avoiding any nuisance with transient voltages during switching periods. In this case the switching model of the inverter must be featured by a grounding point on the DC link, necessary for avoiding simulation errors, and a floating star centre of fictitious voltage sources representing the internal ac side of the model. Instead this point must be grounded for modelling split DC link inverters. It must be noted that DC link cannot be grounded in other nodes in transformerless configurations unless resulting harmful neutral point voltage shift and ground currents. Considering the simple network of Figure 3-3, where:

- a two level inverter is controlled as a simple current source without implementing any LVRT control;
- a single phase fault occurs on phase at 1.5 s with clearing time 50 ms;

The effects of aforementioned described countermeasures can be easily verified comparing the subplots in Figure 3-4 and Figure 3-5.

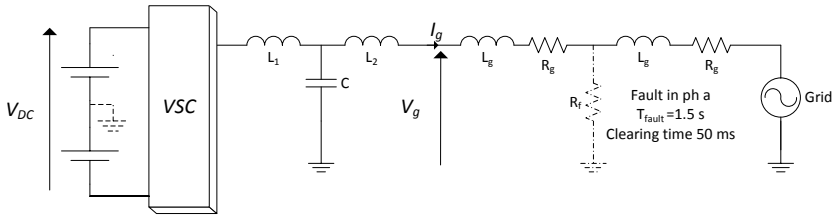

Figure 3-3: network scheme.

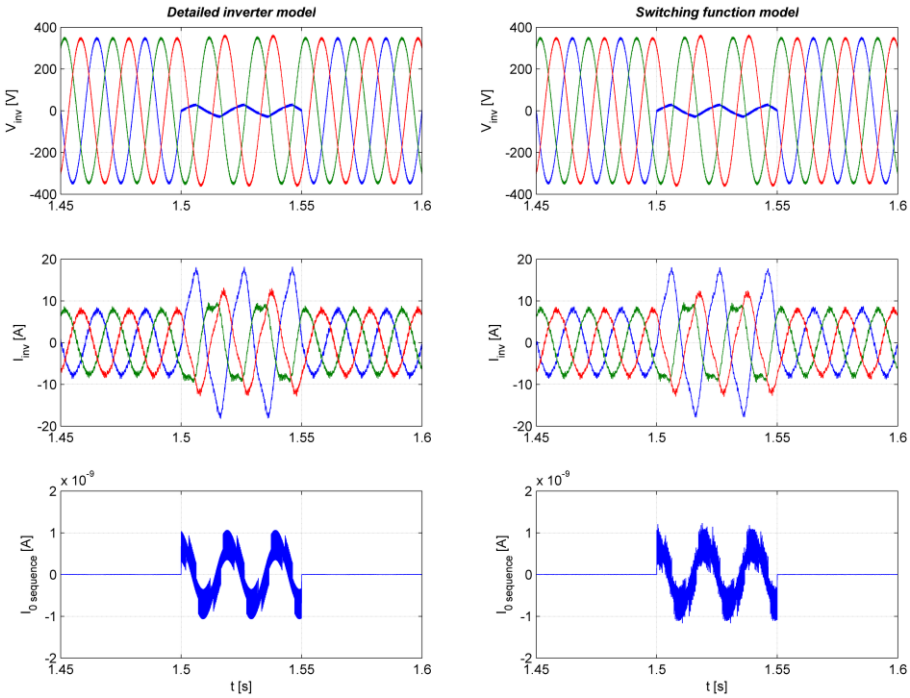

Figure 3-4: voltage and current profiles for different representations of floating DC link inverter

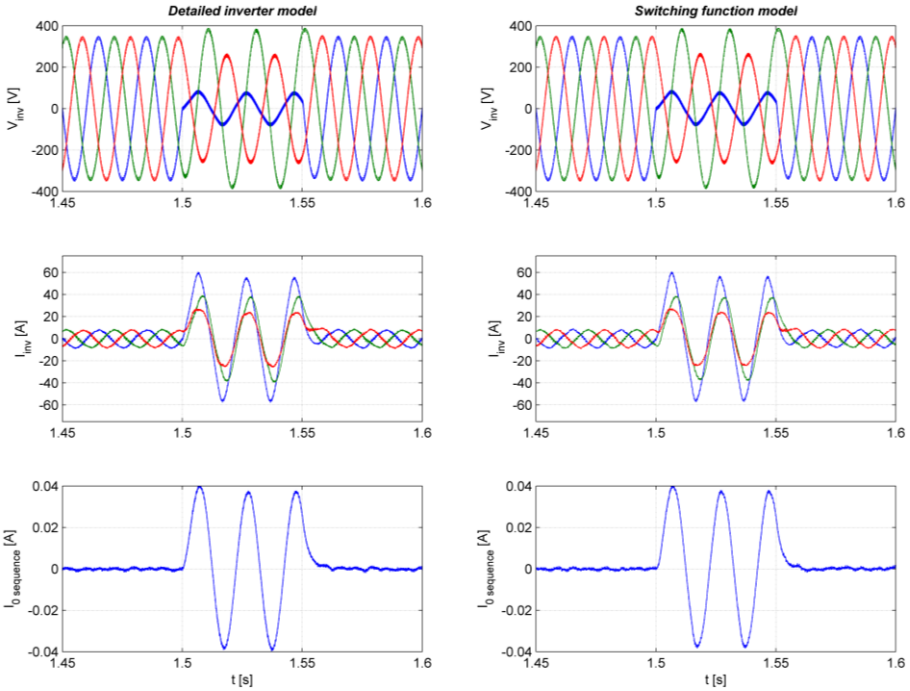

Figure 3-5: voltage and current profiles for DC split link inverter representations.

If the harmonics response at PWM orders is out of interest for the designer, an *average model* [65], as shown in Figure 3-6, can be adopted.

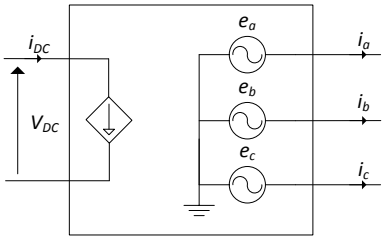

Figure 3-6: average inverter model.

On the assumption of lossless inverter this model keeps the power balance between inputs and outputs over a sampling time interval. This is made possible by:

$$i_{DC} = \frac{\sum_{j=a,b,c} e_j i_j}{V_{DC}} \tag{3.7}$$

Since externally controlled voltage sources composing the AC side are directly driven by the output of the current regulator, no information regarding the modula-

tion is necessary. The designer should be aware that previous simplification doesn't allow verification of the decoupling of current regulator bandwidth with the switching frequency.

In case the designer is interested only to the response at fundamental frequency, the shunt branch of output filter can be neglected. This clearly cannot be done whenever interested to evaluate the stability at low order harmonics.

Same countermeasures and considerations about grounding status, described for switching function model, must be taken for the average one.

As proof of the treatise are reported in Table 3-1 the time taken by aforementioned types of inverter models running the simulation in a computer powered by an Intel® Core™ i7 CPU with 4 GB RAM and mounting Win7, SP1, 64bits and using PSCAD® 4.5.1. It must be noted that in order to get a fair comparison the same duration of the run, time step and plot step are adopted, even if the average model could work with much larger time steps.

Table 3-1: simulation times in case of different models of floating DC link inverter.

Inverter model	**Semiconductor**	**Switching function**	**Average**
Duration of the run [s]	2	2	2
Time step [μs]	5	5	5
Plot time [μs]	25	25	25
Simulation time [s]	**60**	**30**	**22**

3.2 GRID FILTER DESIGN AND DC LINK RATING

Grid filter design has been widely studied in the last decade [66-69]. This paragraph focuses on the design criterion for the particular case of flexible DGs, described in paragraph 2.1. They are featured by:

- Some tens of kilowatt rating;
- Three-phase LV connection in transformer less configuration;
- Variable grid impedance, since the unit should be operated both in grid connected and islanded modes;
- Variable active and reactive powers, not leading to a constant power factor operation;

Given the system focus of this thesis, practical issues like magnetic design, Equivalent Series Resistances of filter inductors and evaluation of the overall filter efficiency are neglected. Moreover the choice of the switching frequency is here made regardless by the efficiency optimisation of the converter and heat dissipater design.

Nowadays low pass LCL filters are the state of the art solution for complying with grid code regulations in terms of limiting the harmonic injection. Hereinafter the nomenclature of Figure 3-7 is considered.

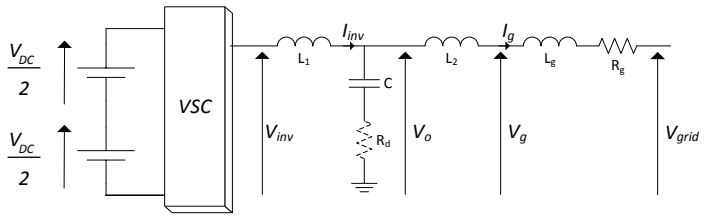

Figure 3-7: nomenclature scheme.

In the ideal LCL filter, neglecting the grid impedance, the equivalent impedance at the VSC terminals results null at the resonance frequency f_{res} :

$$f_{res}^{id} = \frac{1}{2\pi}\sqrt{\frac{L_1 + L_2}{L_1 L_2 C}} \tag{3.8}$$

Harmonics at frequencies higher than f_{res} are filtered out with $-60\frac{dB}{dec}$ slope. Therefore f_{res} should be chosen [67] in order to meet:

$$10 f_{grid} < f_{res} < 0.5 f_{SW} \tag{3.9}$$

Where f_{SW} is the switching frequency and f_{grid} is the grid frequency.

Inequality (3.9) provides first LCL design criterion. The choice of LCL parameters on the other hand turns out subject to some trade-offs, as between inductors size current harmonics injected into the grid or DC link rating and the same inductors.

The VSC side inductor L_1 , here called boost inductor, is usually selected on the base of maximum admissible current ripple ΔI_{max} set for the VSC side inductor. With a reasonable approximation indeed the PWM current harmonic is flowing almost at all through the shunt filter capacitor, an impedance path at very low impedance at this frequency. In a two level inverter every half switching period v_{inv} varies between $\pm\frac{V_{DC}}{2}$ and $\mp\frac{V_{DC}}{2}$. KVL applied to inductors implies:

$$v_L = L_1 \frac{di_{inv}}{dt} \tag{3.10}$$

Under previous considerations equation (3.10) turns in:

$$V_{DC} = L_1 \frac{\Delta I_{max}}{\frac{T_s}{2}} \tag{3.11}$$

Straightforward the boost inductance should be:

$$L_1 > \frac{V_{DC}}{2 f_{SW} \Delta I_{max}} \tag{3.12}$$

Grid side inductance L_2 can be designed following the thumb rule [67] for achieving high harmonic attenuation towards the grid:

$$0.5 L_1 < L_2 < L_1 \tag{3.13}$$

It must be noted that the choice of both inductances, L_1 and L_2, is bound by the resonance frequency, therefore to the capacitance C and by the linearity limit of the PWM. Without performing third harmonic injection [70] and regarding a sinusoidal PWM, for operating in linear region must be fulfilled:

$$V_{DC\min} = 2 V_{inv}^{L-N peak} \tag{3.14}$$

Where $V_{inv}^{L-N\,peak}$ is the peak of the fundamental phase voltage at the VSC side. Latter consideration is of primary importance in high current DGs, where the voltage drop across the filter can be relevant. At the fundamental indeed, where the current flowing in the shunt capacitor can be considered negligible, the voltage drop across both filter inductances, hereinafter summarized with $L_t = L_1 + L_2$, has not to force to overmodulation. Considering the PCC voltage equivalent to the nominal grid value and the worst case, occurring when the current is in quadrature lagging respect to the grid voltage (over-excited mode), as shown in Figure 3-8, the PWM linear mode is ensured by the least DC link rating voltage of Figure 3-9.

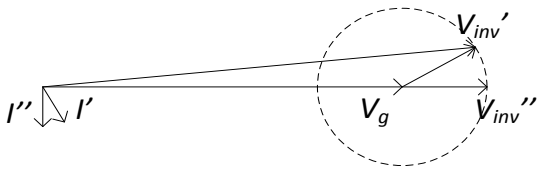

Figure 3-8: phasor diagram representing KVL at the output filter.

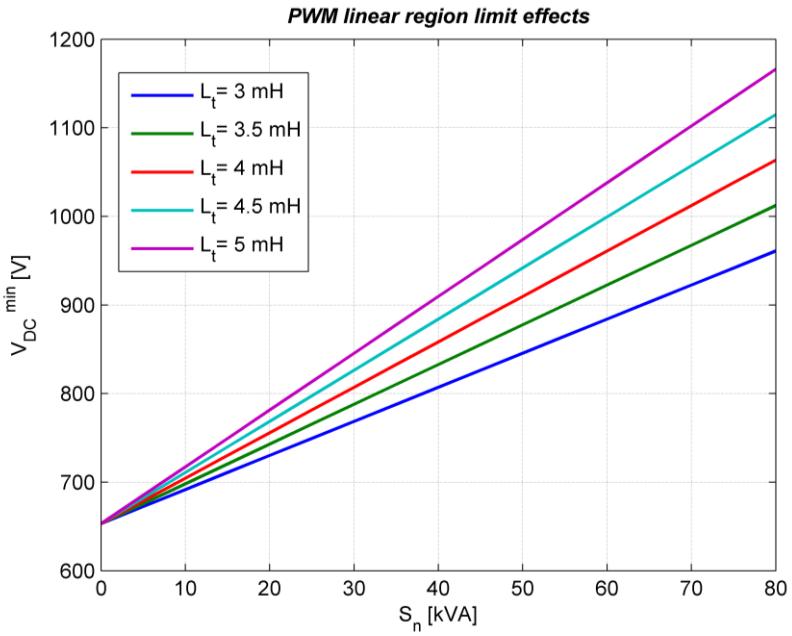

Figure 3-9: overall output filter inductance and DC link voltage as function of the nominal unit power, in case of $V_g = 400V$.

Above design criterion for given VSC parameters and design specifications listed in Table 3-2, resulted into the passive damped LCL parameters of Table 3-3.

Table 3-2: VSC parameters and design specifications.

f_{sw}[kHz]	12
S_n [kVA]	80
V_{dc} [kV]	1
$f_{res}^{id}[\,kHz\,]$	2
I_{ripple} [A]	5.6

Table 3-3: LCL parameters.

L_1 [mH]	2.5
L_2 [mH]	1.5
C [μF]	6.75
R_d [Ω]	7.5
R_1 [Ω]	0
R_2 [Ω]	0

The passive damping resistor listed in Table 3-3 is considered to be installed in series to the filter capacitor as shown in Figure 3-7. Such topology provides more robustness to the filter, which is expected to fit to flexible DGs operating either in grid connected or islanded modes. On the other hand it results an overall efficiency reduction due to increased losses. The passive damping choice can be shortly ex-

plained examining the plant transfer function of the current loop whenever sensing the inverter side current, representing the equivalent admittance at VSC terminals:

$$
\begin{aligned}
Y_{eq}(s) &= \left.\frac{i_{inv}}{v_{inv}}\right|_{v_{grid}=0} = \frac{\sum_{i=0}^{2} N_i s^i}{\sum_{j=0}^{3} D_j s^j} \\
N_0 &= 1 \\
N_1 &= \left(R_d + R_g\right)C \\
N_2 &= \left(L_2 + L_g\right)C \\
D_0 &= R_g \\
D_1 &= \left(L_1 + L_2 + L_g + CR_dR_g\right) \\
D_2 &= \left(L_1R_d + L_2R_d + L_1R_g + L_gR_d\right)C \\
D_3 &= \left(L_2 + L_g\right)CL_1
\end{aligned}
\tag{3.15}
$$

In Figure 3-10 the plant transfer function of (3.15) is plotted under different scenarios. Relevant observations follow:

- The equivalent admittance is characterised by two resonance peaks. It must be noted that the peak at highest admittance represents the resonance at f_{res} ;
- As much as the short circuit power of the network is lower (weaker network) as much the resonance frequencies are lower than ideal;
- The resistive components, either due to R_d and R_g, decrease the magnitudes of the equivalent admittance at the resonance frequencies. This is beneficial for current loop stability since it reduces the risk of multiple 0 dB axe crossovers;
- The adoption of a passive damping resistor contributes to make the filter more robust respect to impedance network variations.

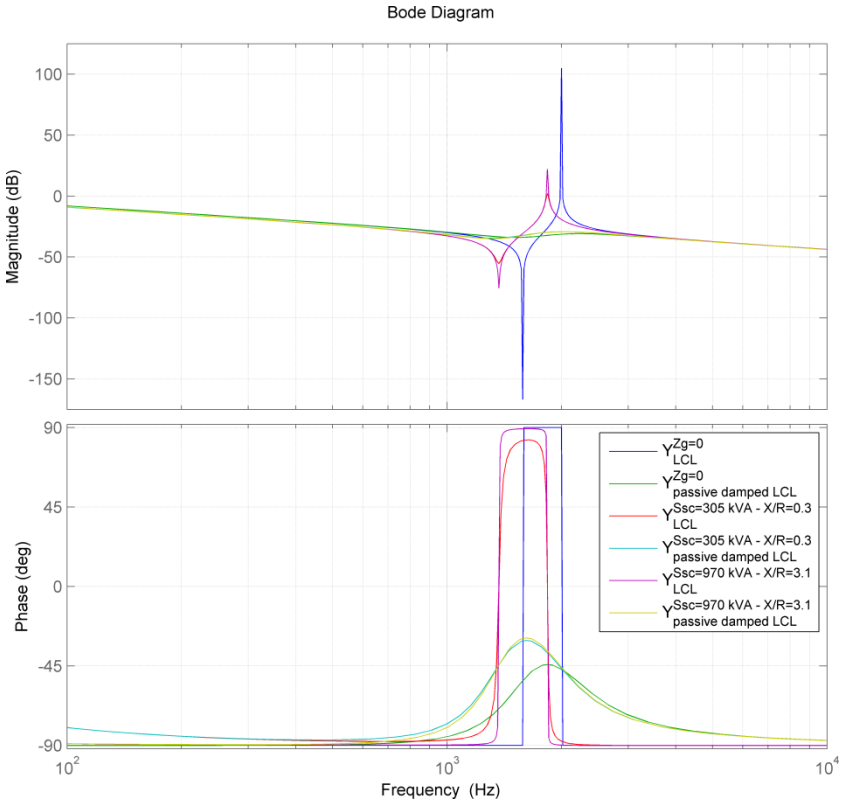

Figure 3-10: exact transfer function of the plant to be considered for the current controller.

On the other hand, it is imperative reminding that passive damping solution decreases the efficacy of the LCL filter in terms of current harmonic rejection. Regarding the transfer function between output and input currents:

$$G_i(s) = \frac{i_{grid}}{i_{inv}} = \frac{(CR_d)s + 1}{(CL_2 + CL_g)s^2 + (CR_d + CR_g)s + 1} \tag{3.16}$$

The corresponding Bode plots shown in Figure 3-11 confirm aforementioned drawback of the passive damping, since the attenuation of harmonics higher than corner frequency has a slope higher than $-60\frac{dB}{dec}$. Moreover same plots highlight that the usage of a damping resistor slightly decrease the corner frequency, as already shown by Figure 3-10.

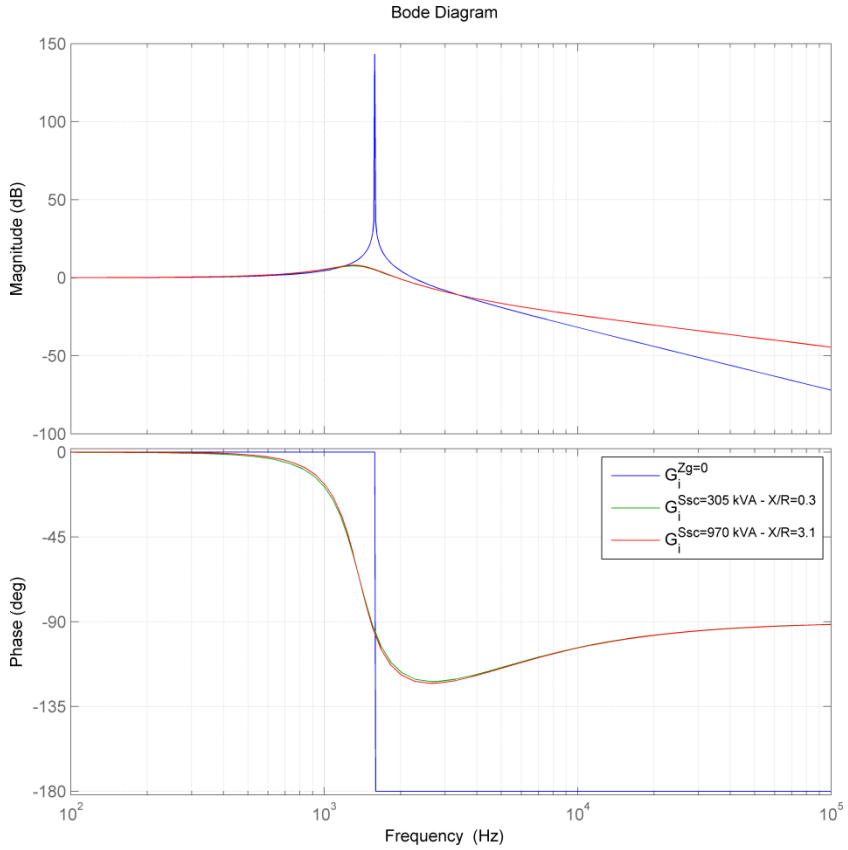

Figure 3-11: LCL current attenuation.

An active damping solution on the other hand would have been more efficient but it is more sensitive to parameter uncertainties [68].

3.3 CONTROLLERS DESIGN

3.3.1 PRINCIPLE OF CASCADED LOOPS

Cascaded loop principle is well known in control theory for having a quick control response with good disturbance rejection. If the disturbance in fact acts on an internal control variables, an inner loop can cope it without significantly affecting the overall response. Such principle nevertheless relies over proper decoupling of different regulator loops. A thumb rule is having a ten times factor between the bandwidth of cascaded closed loops. Practically, with minimum phase systems, such relations can be extended to the crossover frequencies, referred to the open loop transfer function, as done by [66, 71, 72] for VSC controls.

3.3.2 GRID CURRENT REGULATOR

The current controller has been widely implemented both for drives and grid connected inverters [71-74]. The detailed demonstration of the ideal plant equations is given in A.1. In Figure 3-12 both grid current plant and control are represented, regarding the synchronously rotating reference frame aligned to the sensed voltage.

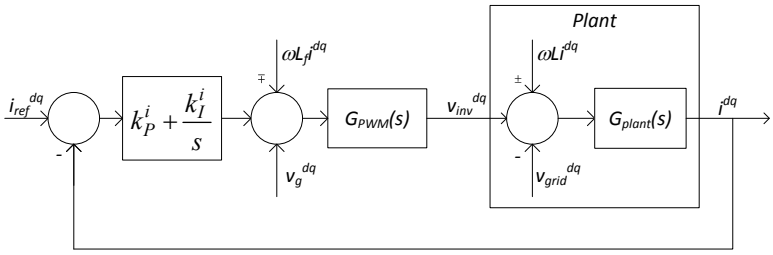

Figure 3-12: overall control scheme.

In particular in Figure 3-12 can be identified:

- The plant transfer function, which in the ideal case according to A.1 is:

$$G_{plant_{ideal}}(s) = \left.\frac{i}{v_{inv}}\right|_{v_{grid}=0} = \frac{1}{R+sL} \tag{3.17}$$

- The block $G_{PWM}(s)$ represents the computational delay introduced by the DSP (one switching period) and the actuation time taken by the modulator for transforming the duty in the corresponding IGBTs status (corresponding on average to an half switching period). The lumped dead time delay can be approximated to a first order lag transfer function, through Padè approximations at the first order term:

$$G_{PWM}(s) = e^{-1.5T_s s} \cong \frac{1}{1+1.5T_s} \tag{3.18}$$

- $\omega L i^{dq}$ cross-coupling terms to be approximated (frequently approximated to $\omega(L_1+L_2)i^{dq}$);
- v_g^{dq} feed-forward voltage terms added in order to speed up the controller response;
- v_{grid}^{dq} acting as a disturbance on a current regulated VSC;
- A PI controller aiming to a quick and null steady state error response [71].

Straightforward from Figure 3-12 the open loop transfer function is:

$$L(s) = G_{PI}(s) \cdot G_{PWM}(s) \cdot G_{plant}(s)$$
$$L(s) = k_p \frac{1+s\tau_i}{s\tau_i} \frac{1}{1+1.5sT_s} \frac{1}{R_s(1+s\tau)} \quad (3.19)$$

Where $\tau_i = \frac{k_p}{k_i}$ and $\tau = \frac{L}{R}$

The PI regulator can be tuned through Modulus Optimum Criteria, demonstrated in A.2, which aims cancelling the dominant pole and achieving a predefined damping (equivalent to a predefined settling time to the step response). The gains so calculated are reported in Table 3-4. It is to be noted that this method doesn't provide any information regarding the proper decoupling between closed loop bandwidth and switching frequency, so it must be verified once the closed loop transfer function is found.

Table 3-4: current regulator parameters for grid connected VSC.

k_p [Ω]	18
k_i [Ω/s]	200

On the other hand, as previously mentioned, the plant of the current regulator is different from (3.17), either due to the presence of the filter shunt branch or the position of the current sensor, which could be mounted on the grid side inductor or at the inverter one. The corresponding control schemes are synthetically represented in Figure 3-13.

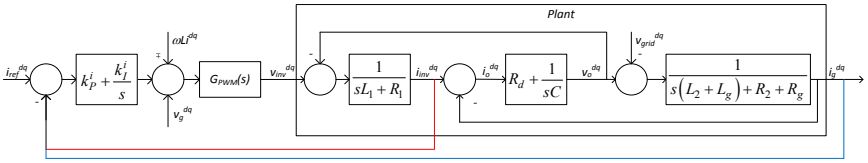

Figure 3-13: overall control scheme. Alternative solutions: current sensor at the inverter side, in red, and current sensor at the grid side, in blue.

The plant transfer function in case of current sensor at the inverter side was already given in (3.15), while whenever the measurement is performed at the grid side turns out:

$$G_{plant_{real}}(s) = \left.\frac{i_g}{v_{inv}}\right|_{v_{grid}=0} = \frac{\sum_{i=0}^{1} N_i s^i}{\sum_{j=0}^{3} D_j s^j}$$

$$\begin{aligned} N_0 &= 1 \\ N_1 &= CR_d \\ D_0 &= R_1 + R_2 + R_g \\ D_1 &= L_1 + L_2 + L_g + C\left(R_1R_2 + R_1R_d + R_2R_d + R_1R_g + R_gR_d\right) \\ D_2 &= \left[L_1\left(R_2 + R_d + R_g\right) + L_2\left(R_1 + R_d\right) + L_g\left(R1 + Rd\right)\right]C \\ D_3 &= \left(L_2 + L_g\right)CL_1 \end{aligned} \tag{3.20}$$

The open and closed loop transfer functions are respectively represented in Figure 3-14 and Figure 3-15. Following considerations are drawn out:

- The approximation introduced considering the ideal plant, therefore used for tuning the regulator, is acceptable since the mismatching between the Bode plots appears only at frequencies much higher than system bandwidth;
- The bandwidth is approximately 450 Hz, therefore it is well decoupled respect to VSC switching frequency;
- The margin of phase is rather high, ensuring a good stability of the system;
- The current closed loop transfer function can be approximated for the definition of the plant of outer loops, as a lag first order transfer function with unity gain and cut-off frequency given by the bandwidth [72];

Overall previous analyses don't take into account the immunity to the grid voltage, which acts as a disturbance for current controlled VSC [75].

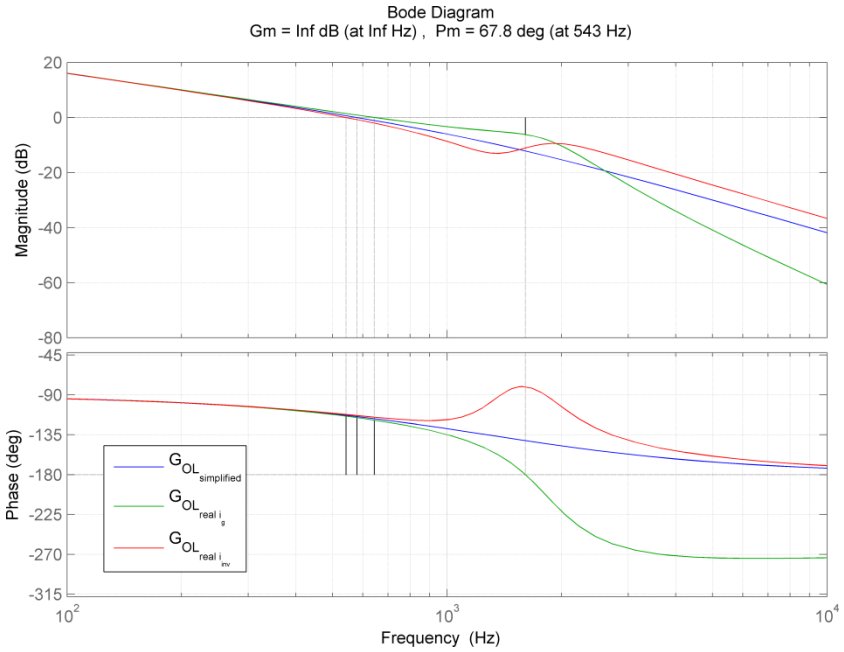

Figure 3-14: current open loop transfer functions, assuming same regulator gains.

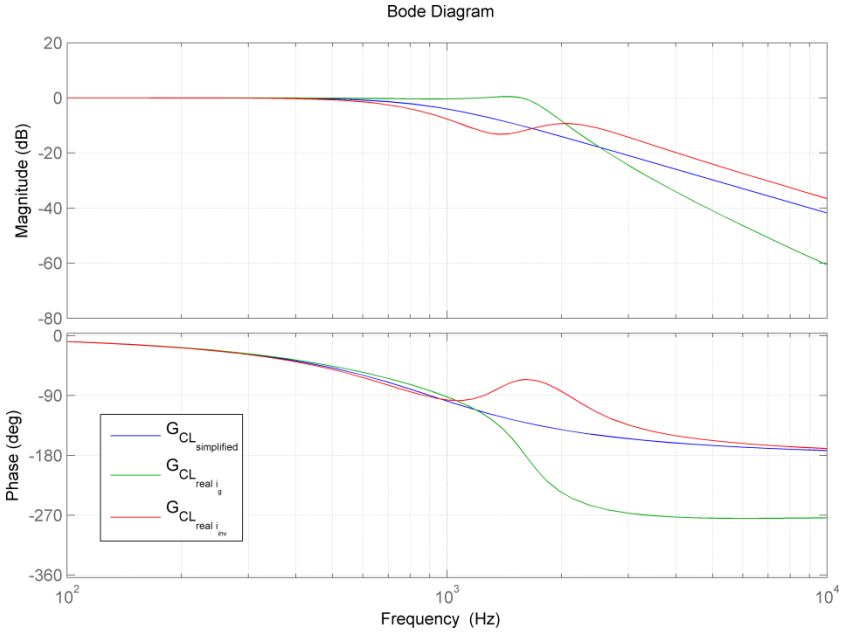

Figure 3-15: current closed loop transfer functions, assuming same regulator gains.

3.3.3 POWER CONTROL

Power regulation can be attained through following alternative methods [68]:

- Open-loop controls directly relying on instantaneous power expression;
- Closed loop control once the bandwidth of the inner current loop is known [76];
- Direct Power Control.

Neglecting the Direct Power Control, which is rather resource demanding and sensitive to grid impedance variations, the first two methods differs only for their bandwidth. The closed loop control in fact is forced to be decoupled by the inner current loop therefore its bandwidth could fall below hundred of Hertz. A particular closed-loop power control is presented in 4.2.2. The open loop method on the other hand has theoretically the same bandwidth of the current loop but the designer has to pay attention to grid filtering issues. In fact given the power references the peak voltage would results enough for computing the current references but the designer should pay attention to the harmonic issue. Whenever operating the control on the rotating reference frame the application of a low pass filter to the grid voltage measurement indeed could improve harmonic rejection, but leading to an overall narrower bandwidth of the control loop.

3.3.4 GRID VOLTAGE REGULATOR

The operation of a VSC in voltage controlled mode is possible either through direct control of the voltage or using a cascaded control structure [77], with an inner current regulator and an outer voltage one. Latter control architecture appears the most adopted in literature but also in this case the current sensor can be mounted at different positions: at the inverter side inductor, as in [9, 31, 33, 78], or at the shunt capacitor, as in [8]. The controlled current indeed cannot be the grid side one, since it acts as a disturbance for voltage controlled VSCs, unless the load impedance is known [79].

Such considerations are of paramount importance and only few papers deals with LCL based voltage controlled VSC [78-80]. In this work the inverter current is kept under control but a second current sensor is mounted at the grid side for taking into account the instantaneous voltage drop across the grid side inductance. This method is equivalent to the adoption of an equivalent mainly capacitive virtual impedance whenever controlling the filter capacitor voltage as performed in [78] (but where the compensation is not operated at the fundamental).

The corresponding control scheme is shown in Figure 3-16.

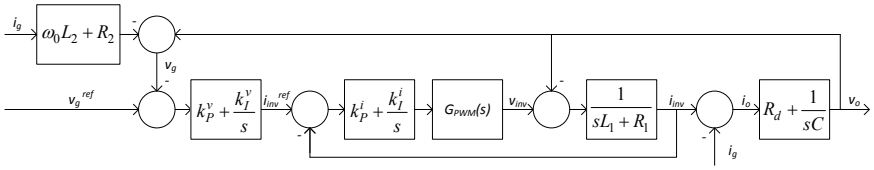

Figure 3-16: control scheme of a voltage controlled VSC using an LCL.

Straightforward the electrical plant transfer function of the current loop is different to what has been described in paragraph 3.3.2. That is:

$$G_{plant}(s) = \left.\frac{i_{inv}}{v_{inv}}\right|_{i_g=0} = \frac{Cs}{(CL_1)s^2 + (R_1 + R_d)Cs + 1} \tag{3.21}$$

In the following treatise the lumped PWM delay block is neglected.

The regulator parameters of the current regulator should be chosen in order to obtain a bandwidth as large as possible, to track at the best the reference in the limits of the stability and for reducing the effect of the disturbance [33]. In order to limit the effect of the zero (implying a negative "type" transfer function) a PI regulator is considered and tuned with the following targets:

- Obtaining a limited attenuation at the fundamental frequency, therefore ensuring a low steady state error;
- Ensuring the stability;

Given the regulator parameters of Table 3-5, the Bode plot representing the open loop and closed loop transfer functions are respectively shown in Figure 3-17 and Figure 3-18, .

Table 3-5: current regulator parameters for voltage controlled VSC.

k_p^i [Ω]	500
k_i^i [Ω/s]	10^6

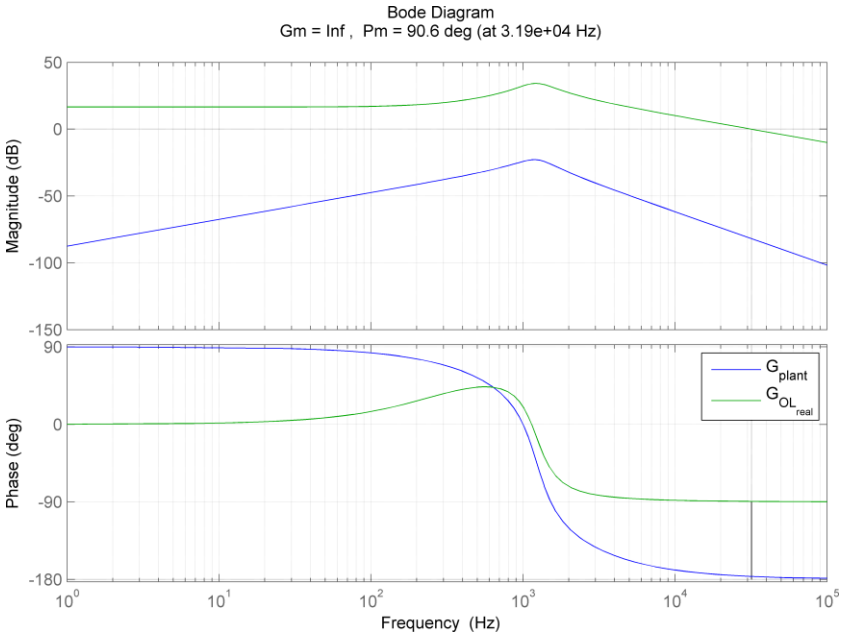

Figure 3-17: Bode plots representing the current open loop transfer function and the main steps leading to the regulator design.

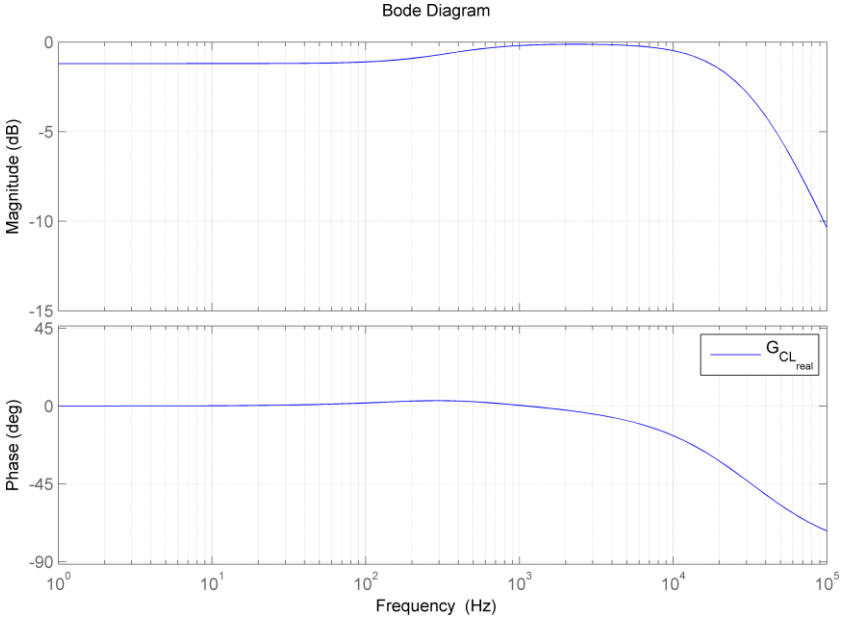

Figure 3-18: Bode plots of the current closed loop transfer function.

Proposed regulator appears fulfilling the regulator design goals. It is interesting to highlight that the error at the fundamental grid frequency is related to the static gain of the closed loop transfer function, approximately -1 dB, since the regulator operates on the rotating reference frame. It must be noted that the synthesis of the regulator is easier whenever the value of the capacitor is higher, as in the case of LC filters (considering the same inverter side inductance, the capacitance must be higher in an LC filter in order to achieve the same resonance frequency).

With reference to the control scheme in Figure 3-16 the open loop transfer function of the voltage regulator becomes:

$$G_{plant}(s) = \left.\frac{v_o}{i_{inv}}\right|_{i_g=0} = \frac{(CG_iG_{pwm}R_d)s + G_iG_{pwm}}{(CL_1)s^2 + (R_1 + R_d + G_iG_{pwm})Cs + 1} \qquad (3.22)$$

Where G_i represents the regulator of the current controller. Applying a PI regulator, whose parameters are listed in Table 3-6 the Bode plot of the open loop transfer function appears as shown in Figure 3-19.

Table 3-6: voltage regulator parameters for voltage controlled VSC.

$\mathbf{k_p^v}$ **[Ω]**	1
$\mathbf{k_i^v}$ **[Ω/s]**	312.5

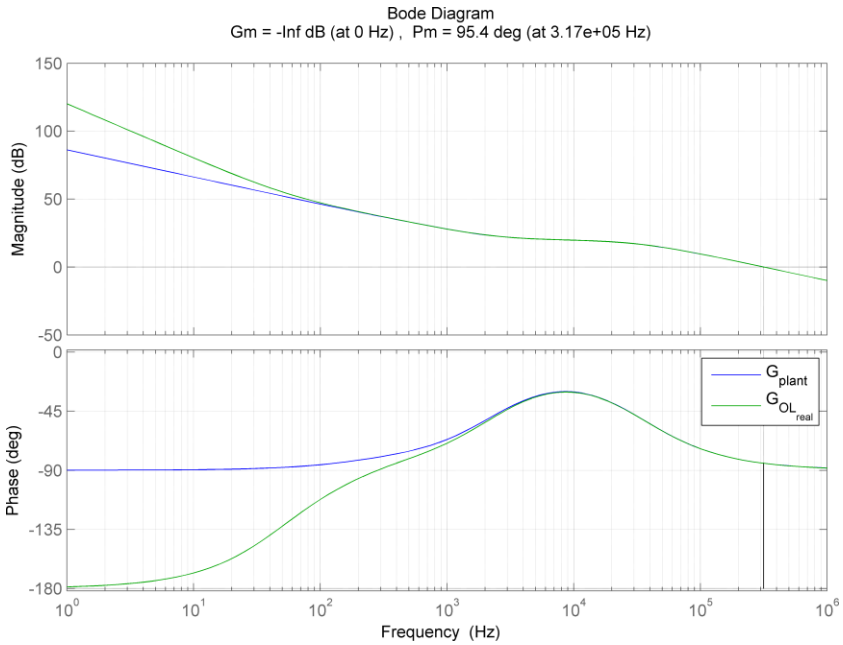

Figure 3-19: Bode plots representing the open loop transfer function of the voltage regulator.

With reference to the notation adopted in this paragraph, the voltage controlled VSC can be reduced to the Thevenin equivalent of Figure 3-20.

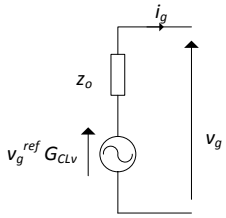

Figure 3-20: Thevenin equivalent of voltage controlled VSC.

Straightforward:

$$v_g = G_{CLv} v_g^{ref} - z_o i_g \tag{3.23}$$

Where:

- G_{CLv} represents the closed loop transfer function respect to the voltage reference:

$$G_{CLv} = \left.\frac{v_g}{v_g^{ref}}\right|_{i_g=0} = \left.\frac{v_o}{v_g^{ref}}\right|_{i_g=0} = \\ = \frac{(CG_iG_{pwm}G_vR_d)s + G_iG_{pwm}G_v}{(CL_1)s^2 + (R_1 + R_d + G_iG_{pwm} + G_iG_{pwm}G_vR_d)Cs + G_iG_{pwm}G_v + 1} \tag{3.24}$$

- z_o is traditionally referred as the output impedance of the converter:

$$z_o = \left.\frac{v_g}{i_g}\right|_{v_g^{ref}=0} = z_o^I + z_o^{II}$$

$$z_o^I = \frac{(CL_1R_d)s^2 + (L_1 + CR_1R_d + CG_iG_{pwm}R_d)s + R_1 + G_iG_{pwm}}{(CL_1)s^2 + (R_1 + R_d + G_iG_{pwm} + G_iG_{pwm}G_vR_d)Cs + G_iG_{pwm}G_v + 1} \tag{3.25}$$

$$z_o^{II} = (R_2 + sL_2)G_{CLv}$$

- G_i and G_v refers respectively to the current and voltage regulator transfer functions.

The Bode plots representing G_v and z_o are shown in Figure 3-21.

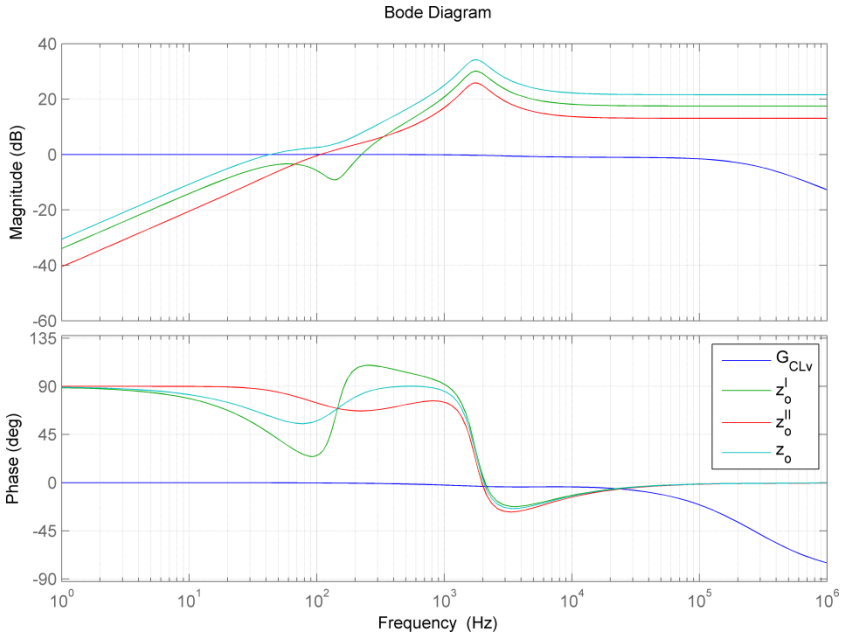

Figure 3-21: Bode plots representing the closed loop transfer function of the voltage loop and the output impedance.

The voltage regulation appears well performing from Figure 3-21. With reference to the output impedance it is interesting to note that its behaviour at the fundamental frequency is inductive with almost unit reactance value. Starting from almost 1 kHz the output impedance tends to be purely resistive and dominated by the passive damping resistance in series to the filter capacitor. Such observations are different from [29] likely due to rather large value of regarded passive damping resistor.

It must be noted that for practical reasons the voltage compensation on the grid side inductor is here going to be limited to the fundamental, applying KVL, as shown in Figure 3-22.

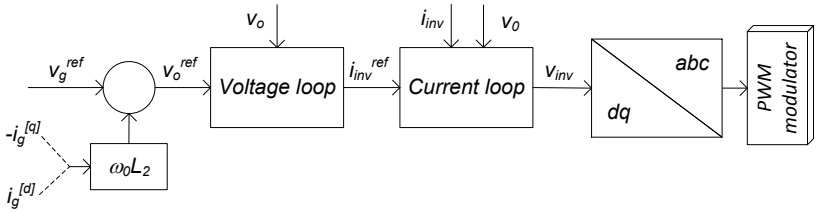

Figure 3-22: voltage drop compensation at the fundamental and overall control scheme structure (continuous arrows define dq components buses while dashed segments the single components).

Extending the compensation to the harmonics improves the quality of the output voltage but implies higher computation burden and a higher amount of harmonics across the filter capacitor.

3.4 CONCLUSIONS

This chapter focuses on different engineering areas but it lays the fundamentals for the design and simulation of networks including VSC interfaced LV flexible DGs.

The choice of the proper VSC model turns out important not only for the extent of details necessary for the simulation but also for the overall run time. For most of the power system simulations an average model is suitable, but the designer should be aware that this VSC representation doesn't allow evaluating both harmonics and their interference with the control. The equivalent switching model overcomes aforementioned limitation but it may lack representation of common mode disturbances.

The chapter demonstrates that a passive damped LCL filter is suitable for both current and voltage controlled VSCs. In this treatise the filter stabilization is achieved through a passive damping resistor, an effective solution for a wide range of equivalent grid impedance that on the other hand impacts on the overall conversion efficiency of the unit. The rating of the DC link voltage is here regarded in order to avoid modulator saturation issues, a design criterion rather important for flexible DGs, which could prompt these units to operate on the capability edge in over-excited mode. The regulators tuning is widely covered through a symbolical analyses of the plant transfer functions, obtained at a priori using MuPAD tool [14]. In order to compensate the voltage drop on the grid side inductance of the LCL filter, a compensation at the fundamental is proposed and its effect on the output Thevenin impedance is taken into account.

The analytical approach described throughout the chapter turned out useful for defining a MATLAB® program for the overall design of a VSC. Given main specifics such script allows automatically designing either the output filter and tuning the regulators. A summary flow chart is proposed in Figure 3-23.

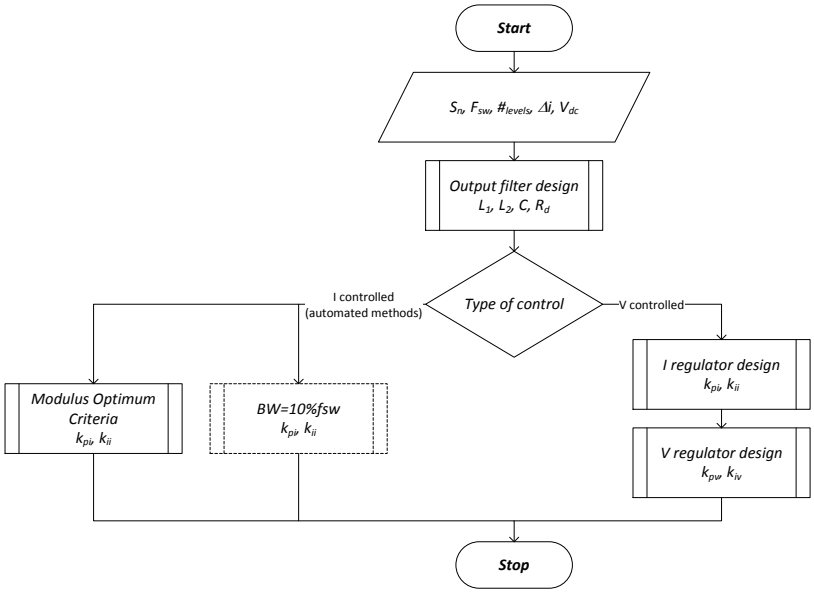

Figure 3-23: summary flow chart for the automatic design of the VSC.

As a final consideration the overall chapter takes into account rather large values of the filter inductances, not practical for industrial VSCs. On the other hand this doesn't impact on the overall analyses, which can be easily repeated since all the transfer functions are symbolically defined. A further improvement could address the effects of the PWM delay on the stability of the voltage regulation in presence of a passively damped LCL filter.

CHAPTER 4

VSC INTERFACED LV FLEXIBLE UNITS

The transition to Active Low Voltage Distribution Networks opens the scenario about intentional islanding [12] in case of poor grid quality or system black-out. Nevertheless in order to manage the islanded system both dispatchable LV units and a proper control of the grid interface must be defined.

The first requirement can be satisfied through microturbines and stationary battery units derived from electric vehicle battery packs as recently annonunced by [19]. This chapter therefore proposes in the first part the modelling of those units for integration studies. A detailed model of the MT is provided and tested. A novel battery model is here defined starting directly from cell manufacturer datasheet.

The chapter follows with the analyses of the hierarchical control and its applications to VSC interfaced units, starting from the background given about inner control loops given in the previous chapter. A comparison between direct droop schemes, with angle bias and frequency bias, is given under different load conditions in a single busbar MG. Moreover the reverse droop, traditionally applied to grid following units, is here tested for managing a MG, describing its limitations. The comparison between direct and reverse droop control scheme follows in the case of islanding of CIGRE benchmark network residential feeder [81] in case of distribution network subject to load shedding. Under this scenario the effect of secondary control is tested and the effects of a PID controller for the voltage regulator in the reverse droop scheme is assessed.

The contents of this chapter are partially presented in [82].

4.1 DG MODELLING

As stated in paragraph 2.1.3 this chapter considers a MT and a SBU, whose storage is derived from EVB, as two possible flexible units. Both units indeed are dispatchable, they are featured by fast ramp response and are VSC interfaced. From a VSC control modelling perspective the knowledge of the "prime mover" model itself would not be necessary, since the DC side could be represented by an ideal DC

voltage source. Nevertheless this paragraph moves the designer's horizon to power system simulations, proposing two models for these units.

4.1.1 MICROTURBINE MODELLING

The survey reported in Table 2-1 highlights that typical layout for a MT rated several tens of kilowatts is as in Figure 3-1.

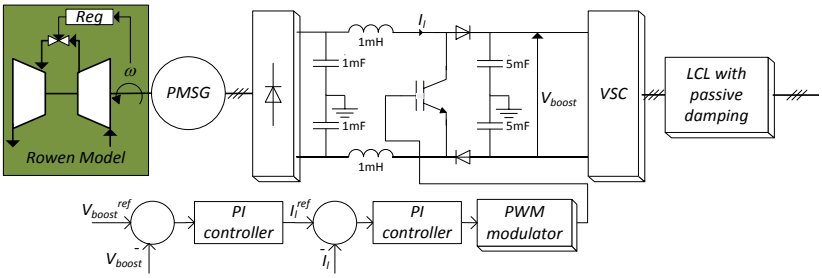

Figure 4-1: Microturbine conceptual scheme (© 2013 IEEE).

Starting from the prime mover every MT performs a regenerative Brayton cycle by means of a compressor, a rotating recuperator, a combustor and a turbine, in single shaft configuration and without Inlet Guide Vanes. According to large part of literature the prime mover can be represented through the reduced Rowen model, as shown in A.3. In fact the fuel flow rate is determined by the speed regulator, because the limiting signals regarding the acceleration control (involved only during startup) and the outlet gases temperature (usually not available in MTs) are neglected. This prime mover model is inherited from larger gas turbines, therefore it cannot fit to MT start up procedure and it doesn't take into account the effect of recuperator. The shaft is directly coupled with a gearboxless construction to a Permanent Magnet Synchronous Generator. Its rotational speed is typically about 100000 rpm. The shaft is represented with a one-mass lumped model. The power converted by the PMSG is normally processed by a power electronics stage, composed of:

- a six bridge diode rectifier. Apart from this an auxiliary smaller rated inverter is usually adopted for start-up procedure;
- a boost converter, necessary for maintaining a sufficiently high voltage at the DC side of the VSC in order to avoid operating the VSC in PWM saturation region. Indeed considering a traditional LV voltage level of 400 V the minimum DC link side voltage must be:

$$V_{DC\min}^{VSC} = 2V_{L-Npeak} = 653.2 \ V \tag{4.1}$$

On the other hand taking into account the nominal voltage of the PMSG, as listed in Table 4-1, the rectifier output voltage whenever the PMSG is spinning at nominal speed is:

$$V_{DC}^{rec} \cong \frac{3\sqrt{2}}{\pi} V_{AC}^{rec} = \frac{3\sqrt{2}}{\pi} V_n^{PMSG} = 648 \quad V \tag{4.2}$$

Evidently there is the need of boosting the voltage, taking also into account the possibility of voltage rise at the AC terminal of the MT and transient shaft speed drops. The boost stage is operated in Continuos Current Mode and controlled with a cascade of a voltage and current loops according to [83];

- The VSC is designed according to the guidelines given in Chapter 3;

For stability reason the boost topology is symmetrical with respect to the ground. The converter pursues the regulation of its output DC link voltage.

All MT parameters apart from VSC related parameters, already given in the previous chapter, are listed in Table 4-1.

Table 4-1: MicroTurbine parameters.

Subsystem	Parameter	Value
PMSG	$V_n \left[V\right]$	480
	$P_n \left[kVA\right]$	85
	$\omega_n \left[rpm\right]$	60000
Lumped shaft	$H = \frac{J\omega_n^2}{2P_n}\left[s\right]$	1.5
Boost parameters	$V_{DC}^{ref}\left[V\right]$	850
	$k_p^V \left[S\right]$	0.8
	$k_i^V \left[\frac{1}{\Omega s}\right]$	5
	$k_p^I \left[\frac{1}{kA}\right]$	1.4
	$k_i^I \left[\frac{1}{kC}\right]$	10
	$f_{SW}\left[kHz\right]$	7.5

The MT response is evaluated in case of step active power set-point variations. Main system profiles are shown in Figure 4-2.

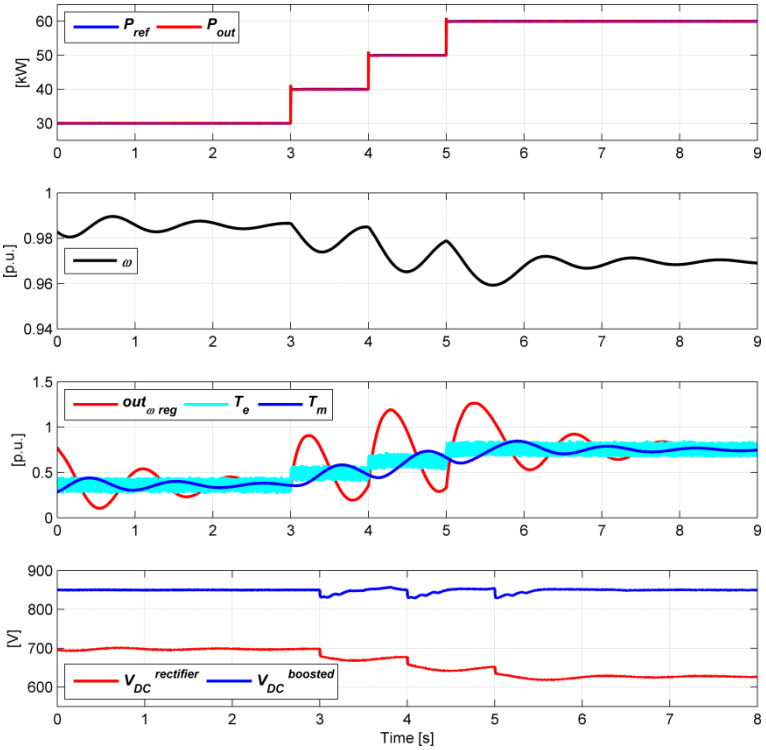

Figure 4-2: microturbine response to active power steps.

From the scenario represented in Figure 4-2, it can be observed that:

- Active power control is effective as described in 3.3.2;
- Rowen model shows up a damped oscillatory response both at low and high loadings. The same turns out not to be isochronous, even if the speed deviation is limited. It is worth to notice that the output of the speed regulator overcomes the upper limiter ceiling (at 1 p.u.) at the step changes at high loadings. Latter behaviour however has no consequences on the mechanical torque due to the dynamics affecting the fuel flow rate;
- Electromechanical torque is affected by a ripple due to the harmonics currents drawn by the diode rectifier;
- The boost converter appears working properly maintaining the voltage at the DC terminal of the VSC close to the reference value, almost regardless of speed deviations, which affect the rectified voltage;
- As aforementioned Rowen model cannot be considered representative of a real MT since the step response appears almost ideal.

4.1.2 STATIONARY BATTERY MODEL

Conducting power system simulations of SBU for dynamic grid studies allows neglecting fast dynamics of the battery itself, the DC/DC converter or the same VSC interfacing to the grid. To exploit this feature and the need of an easy to be used model a novel battery model is proposed for a Li-Ion stationary storage based on a smart limitation of the dispatching power signal. The proposed methodology relies directly on manufacturer's cell static discharge curves and it can be extended to the charging ones. The overall modelling relies on the following assumptions:

- constant voltage feeding the VSC, a reasonable assumption when the battery is interfaced to the VSC by a bidirectional DC/DC converter;
- fast dynamic response of the cells;
- neglecting temperature variation effects;
- no Peukort and memory effects are considered;

Previous considerations allow modelling the overall "aggregated cell - DC/DC converter" system with a fixed DC voltage source interfaced to the VSC stage. On the other hand the VSC power must be properly limited, taking into account the instantaneous State Of Charge (SOC), that defines both the allowed working region and the maximum output power at instantaneous SOC, and the maximum deliverable current declared by the manufacturer.

The modelling approach here described relies on cell discharge characteristics provided in [84] for a battery cell working in continuous operating mode, where the current limit is set for thermal reasons to 2C (where 1C is the current rate leading to fully discharge a completely charged battery in one hour). Such limitation fits to normal operations, indeed sometimes manufacturers allow reaching up to 4C value or peak usage. Regarded cell [84] is scaled-up in the model by 1544 in order to achieve the nominal capacity of a typical Electric Vehicle battery pack [19] of 40 kWh.

State variable of this model is represented by the SOC, calculated through so called "Coulomb counting" method [85], therefore integrating the instantaneous current given the initial SOC. This model on the other hand doesn't take into account SOC losses at no load, therefore parasitic elements under this condition. The current used for the integral calculation is drawn from a 3D look-up table whose inputs are the instantaneous output power, the same flowing into the VSC, and instantaneous SOC. The simplified scheme is shown in Figure 2.

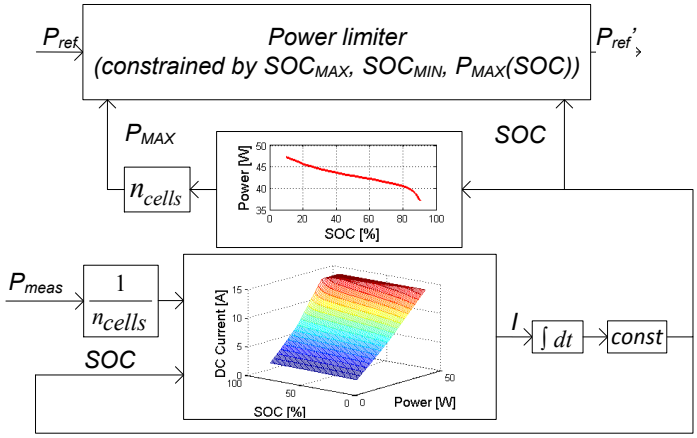

Figure 4-3: battery model (© 2013 IEEE).

Aforementioned 3D look-up table is derived from manufacturer discharge curves on the base of simple considerations, as shown in Figure 4-4. Starting from the parameterized current discharge curves they can be explicitly considered as a function of the output battery power, as shown in Figure 4-4b. Fitting latter curves the power mesh of Figure 4-4c is derived. However as previously described the SOC calculation relies on the integration of the battery current. In order to obtain it previous power mesh is manipulated, defining a current mesh representing a 3D look-up table, whose entries are just the battery power and SOC.

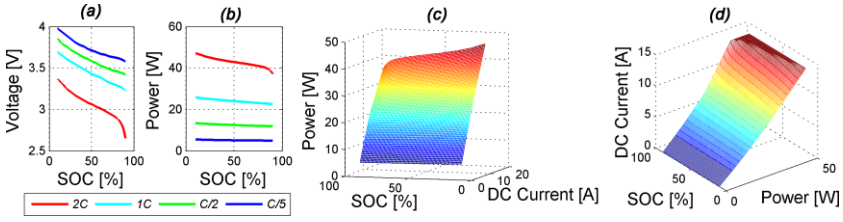

Figure 4-4: 3D look-up table process definition, (a) manufacturer discharge characteristics, (b) and (c) curve processment, (d) representation of resulting 3D look-up table (© 2013 IEEE).

The battery unit modelled in PSCAD® is firstly tested varying the input power reference, in order to test the limitations imposed by the operating SOC (20÷90%) and maximum allowed power (dependant by the SOC). The battery response is illustrated in Figure 4-5. Initially the power reference exceeds the maximum deliverable power, therefore the power output turns out lower. At 72 s the battery runs to the least limit of SOC interrupting the discharge mode regardless of the dispatching export power signal. This condition lasts until 120 s, when the reference power becomes negative starting the charging mode.

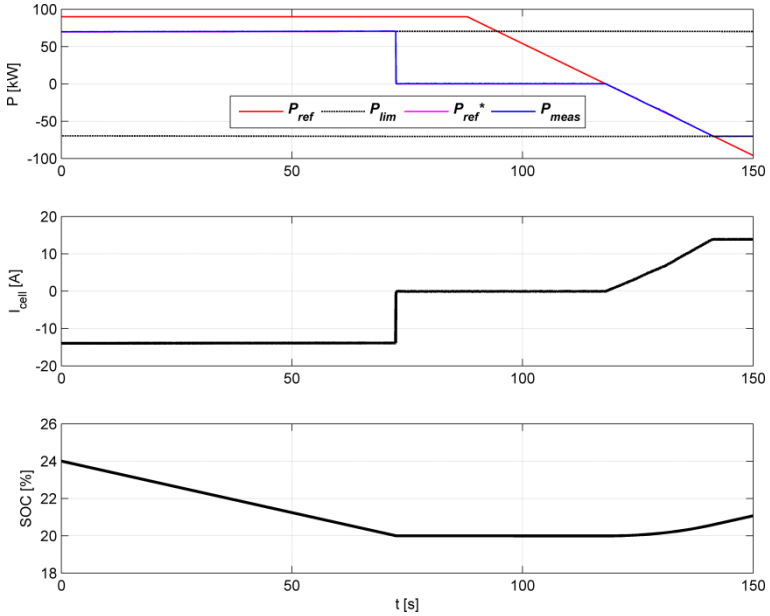

Figure 4-5: battery unit test (© 2013 IEEE).

The same proposed battery model is then compared with the corresponding model available in SimPowerSystems library [13]. Latter simulation on the other hand includes a bidirectional DC/DC converter. A static comparison is made in the first time window, between 0 s and 30 s, starting from the same initial SOC, while the dynamic response is evaluated imposing two step power reference changes. Main profiles about the two simulations are proposed in Figure 4-6. Both static and dynamic responses match. Only a small current mismatch appears throughout the simulation. Moreover the first subplot in Figure 4-6 confirms the initial assumption made in this paragraph for defining the proposed battery model about the constant output voltage of the DC/DC converter during dynamic conditions.

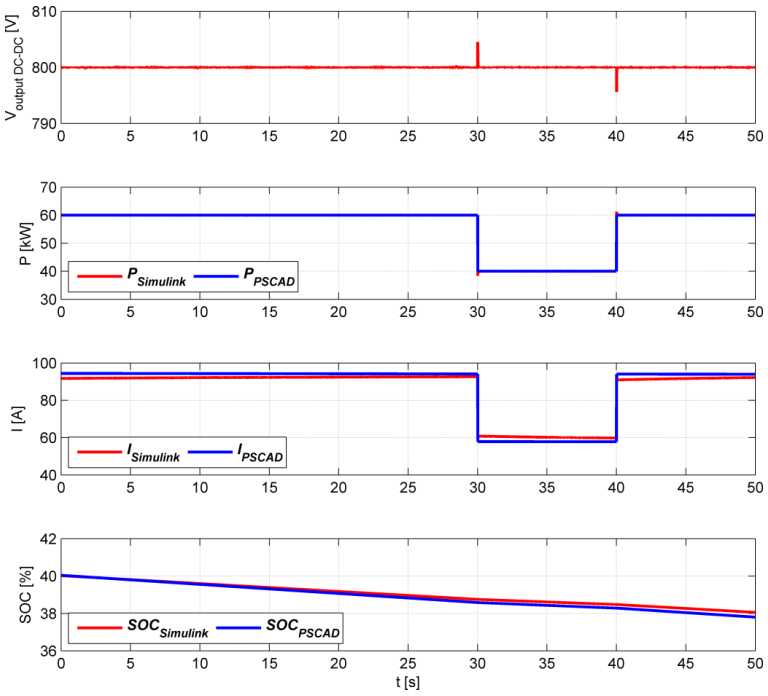

Figure 4-6: Battery models comparison (© 2013 IEEE).

4.2 HIERARCHICAL CONTROL APPLICATIONS

Power sharing among VSCs in islanded mode has been developed from traditional power systems. As mentioned in the state of the art the droop characteristics are dependant on the Thevenin equivalent impedance, connecting the DG to the equivalent voltage source.

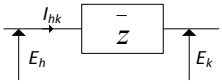

Figure 4-7: single-phase equivalent of a line.

Considering the scheme of Figure 4-7 the load flow equations defining the power send from node *h* to *k* can be written:

$$\overline{S_{hk}} = P_{hk} + j \cdot Q_{hk} = \frac{V_h^{\,2}}{z}\left[cos\,\varphi_z + j \cdot sin\,\varphi_z\right] - \frac{V_h V_k}{z}\left[cos\left(\varphi_z + \theta_h - \theta_k\right) + j \cdot sin\left(\varphi_z + \theta_h - \theta_k\right)\right] \quad (4.3)$$

Where:

- $\bar{z} = R + j \cdot X = z(\cos\varphi_z + j \cdot \sin\varphi_z)$
- E and V respectively refer to the phase-to-ground and phase-to-phase voltages;
- $\theta_h - \theta_k = \angle\overline{V_h} - \angle\overline{V_k}$.

Assuming $\theta_k = 0$ equation (4.3) leads to:

$$\Rightarrow \begin{cases} P_{hk} = \frac{V_h}{z^2}\left[R\left(V_h - V_k\cos\theta_h\right) + XV_k\sin\theta_h\right] \\ Q_{hk} = \frac{V_h}{z^2}\left[-RV_k\sin\theta_h + X\left(V_h - V_k\cos\theta_h\right)\right] \end{cases} \tag{4.4}$$

Through the following linear transformation, firstly proposed by [34], two power terms, $P_{hk}{}'$ and $Q_{hk}{}'$, can be identified, which are decoupled from φ_z respect to P_{hk} and Q_{hk}.

$$\begin{bmatrix} P_{hk}{}' \\ Q_{hk}{}' \end{bmatrix} = T\left(\varphi_z\right)\begin{bmatrix} P_{hk} \\ Q_{hk} \end{bmatrix} = \begin{bmatrix} \sin\varphi_z & -\cos\varphi_z \\ \cos\varphi_z & \sin\varphi_z \end{bmatrix}\begin{bmatrix} P_{hk} \\ Q_{hk} \end{bmatrix} \tag{4.5}$$

$$\Rightarrow \begin{cases} P' = \frac{V_h V_k}{z}\sin\theta_h \\ V_h - V_k\cos\theta_h = \frac{zQ'}{V_h} \end{cases} \tag{4.6}$$

From equation (4.6) it is evident that $P'-\theta_h$ and $Q'-V_h$ droops can be established. It is then straightforward that droops are grid impedance dependant. Some authors therefore proposed to properly modify the inverter output impedance [29, 34] while others used the decoupling matrix given the grid impedance angle [34, 35, 86]. The impedance angle on the other hand is usually unknown, therefore in literature several grid impedance estimation methods were proposed [35, 87-90]. It must be noted on the other hand that incorrect network impedance estimation, as well as too strict droop gains, could have the effect of deteriorating the system stability. Those effects can be analytically assessed only through eigenvalue analyses, as proposed in [35, 86, 91]

In this work the network impedance estimation was ignored since the intentional islanding is supposed to be limited to the farther part of LV feeders. This assumption

is made taking into account that considered flexible DGs have very limited rating. Follows that the cross section of the feeder conductor interested by the islanding is relatively small, therefore implying an equivalent grid impedance featured by a relative high resistance to reactance ratio. Under previous considerations and neglecting the output impedance of the converter, which is relatively small, and the load effects, in islanded mode the equivalent grid impedance angle φ_z to be used for the orthogonal transformation of equation (4.5) is going to be considered null.

From a practical point of view it is highly recommended to signal the intentional islanding through a dedicated signal, wired or wireless, putting in communication the circuit breaker and flexible DGs. Benefits of a physical media are as follows:

- Safely enabling the islanded mode avoiding unwanted DG disconnections due to asynchronous anti-islanding protection actuations in combination with a loose primary regulation;
- Avoid dangerous swings between units operating with different droop characteristics. Such nuisance could be overcome by the adoption of virtual inductances in the grid forming units;
- Performing the resynchronization to the mains once the conditions that triggered the intentional islanding are ceased;
- Dispatch the control signals inherent to the secondary regulation (optionally);
- Operate gain scheduling for current and voltage controlled modes.

In this work therefore whenever a flexible DG receives the intentionally-islanded signal, the same unit swaps automatically to hierarchical control mode varying the value of the grid impedance angle from 90 deg to 0 deg. Current controlled units instead are not affected by the mode since they are modelled as pure active current controlled sources not providing any ancillary service (f.e. OFPC or DRCS).

4.2.1 HIERARCHICAL CONTROL SCHEMES

The state of the art control scheme for voltage controlled VSCs, as flexible DGs, is the *direct droop*. Two alternative droops are possible [91]: angle based, exploiting $P'-\theta$ characteristics, or frequency based one, exploiting $P'-f$. The relative control schemes are shown in Figure 4-8 and Figure 4-9.

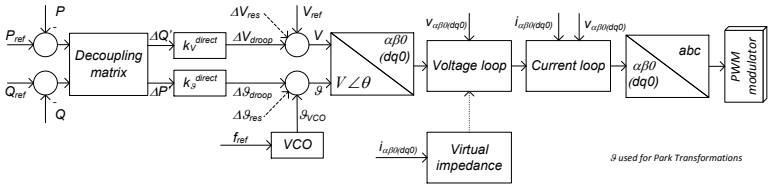

Figure 4-8: direct droop control block diagram based on phase angle bias.

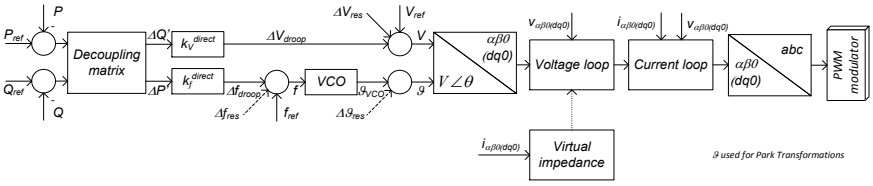

Figure 4-9: direct droop control block diagram based on frequency bias.

It must be noted that in both direct droop control schemes the usage of a PLL can be avoided, even whenever operating the overall control in the dq reference frame. Indeed if the rotating frame is going to be aligned to ϑ, it is enough using the same angle for all Park transformations. Moreover the adoption of such rotating reference frame avoids using the reference generator, since under this assumption the reference of the voltage regulator are $v_d^{ref} = V$ and $v_q^{ref} = 0$. A Voltage Controlled Oscillator is used in both schemes for computing the phase angle, given the frequency. It must be noted that in order to reduce the impact of oscillations on the power measurements, the feedback values are filtered through a first order filter with time constant $T_{PQfilter}$.

Supposing the operation of a single VSC feeding the MG and given the maximum allowable frequency and voltage deviations $\Delta f_{\max}, \Delta V_{\max}$ the droop coefficients can be defined as:

$$k_f^{direct} = \frac{\Delta f_{max}}{\Delta P'_{max}}$$
$$k_V^{direct} = \frac{\Delta V_{max}}{\Delta Q'_{max}} \quad (4.7)$$

Where $\Delta P'_{max}$ and $\Delta Q'_{max}$ refer respectively to the maximum allowed transformed active and reactive power variations of the VSC. It is to be noted that (4.7) underlies to the assumption of no cross couplings between active and reactive power, a simplistic assumption since VSC capability is normally constrained by current and power limits.

The overall network stability can then be verified through eigenvalue analyses. In [91] the VSC dynamics were taken into account, while in [35, 86] simplified treatises were proposed.

Direct droop scheme can be operated even in grid connected mode, even if the power regulation bandwidth becomes rather strict. However operation in parallel to a stiff grid forces selecting the biased frequency droop scheme (the angle droop would not be effective since grid frequency is subject to deviations).

The orthogonal transformation can be applied as well to current controlled units, allowing their participation in the primary control through so called *inverse droop* scheme, as shown in Figure 4-10.

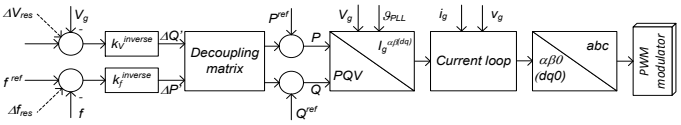

Figure 4-10: inverse droop control block diagram.

The droop coefficient can be computed through:

$$k_f^{inverse} = \frac{\Delta P'}{\Delta f_{max}}$$
$$k_V^{inverse} = \frac{\Delta Q'}{\Delta V_{max}} \quad (4.8)$$

It must be noted that such control turns out suitable for grid following units, instead it suffers the management of a MG without any explicitly voltage controlled unit.

Latter behaviour, as well as the performances of direct droop schemes are below proposed, considering the network of Figure 4-11 featured by:

- Two equivalent DGs, DG1 and DG2. In the first second of time both of them operate at no load, then they share the network loads. At 5 s DG2 is disconnected in order to test DG1 response maintaining previous MG load;
- A 50 m line connecting each DG to the load busbar, featured by $r = 1\frac{\Omega}{km};\ l = 0.656\frac{mH}{km}$ and negligible shunt capacitive component;
- Different types of loads, given a predefined insertion sequence, are stated below:
    - A Constant Power Load L1, irrespective of voltage and frequency variations, inserted at 1 s;

- A Constant Current Load L2, inserted at 2s;
- A Constant Impedance (resistance) Load L3, inserted at 3s;
- A three-phase rectifier, representing a harmonic load, L4, inserted at 4s.

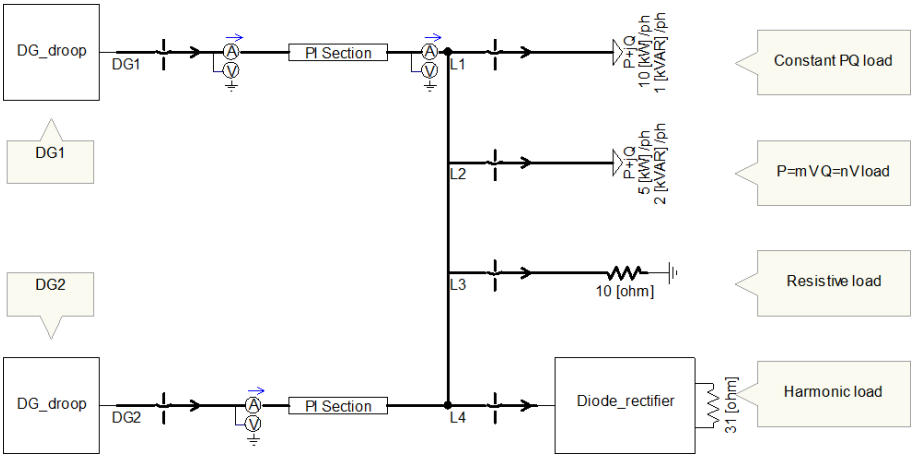

Figure 4-11: microgrid Single Line Diagram.

Moreover in order to achieve a fair comparison between different control schemes the droops are made equivalent, thorough the settings of Table 4-3 and the droop coefficients of Table 4-3. It must be noted that the voltage droop gain was selected in order to highlight significant voltage deviations at high MG loadings. The consequent voltage and frequency deviation therefore result out of normal operating windows.

Table 4-2: nominal values and droop parameters.

S_n [kVA]	80
f_n [Hz]	50
V_n [V]	400
P^{ref} [p.u.]	0
Q^{ref} [p.u.]	0
$T_{PQfilters}$ [ms]	10

Table 4-3: droop parameters.

$k_f^{inverse}$ [kVA/Hz]	5
$k_v^{inverse}$ [kVA/V]	2.5
$k_f^{inverse}$ [p.u./p.u.]	3.13
$k_v^{inverse}$ [p.u./p.u.]	200
k_f^{direct} [p.u./p.u.]	0.32
k_{angle}^{direct} [rad/p.u.]	6.28
k_v^{direct} [p.u./p.u.]	0.4

Most significant plots are given in Figure 4-12, Figure 4-13 and Figure 4-14:

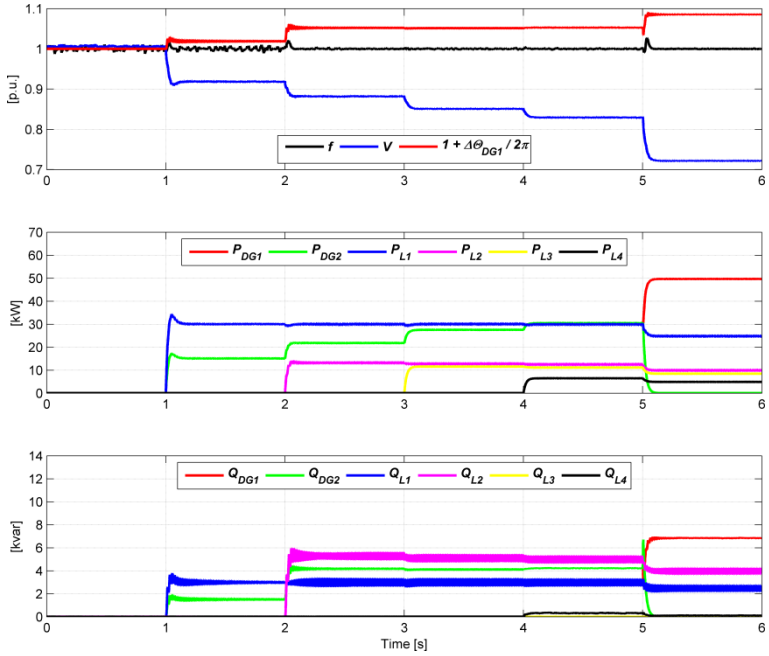

Figure 4-12: direct droop profiles, considering phase angle bias droop.

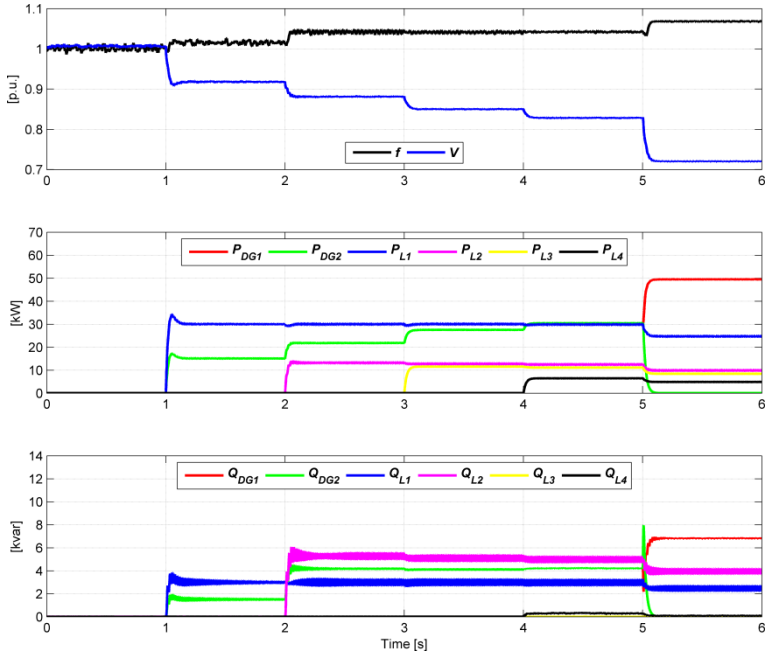

Figure 4-13:direct droop profiles, considering frequency bias droop.

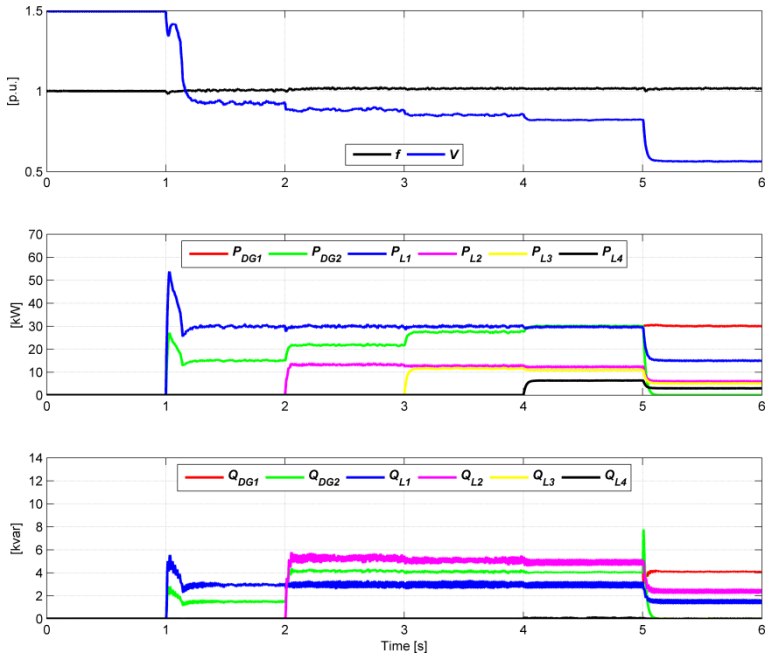

Figure 4-14: inverse droop profiles.

The observations are described as follows:

- Both direct droop schemes led managing the MG through primary control. Assuming no voltage drops along the lines the voltage results:

$$V = 1 - \Delta V = 1 - \frac{P_L}{n \cdot k_v^{inverse}} [\, pu \,] \tag{4.9}$$

  Equation (4.9) establishes that in the first time window spanning from 0 s to 2 s, featured by no load, there are no steady state errors. On the contrary in the following time window, spanning from 1 s to 2 s, where the constant load L1 is connected, the voltage is 0.92 p.u. This can be observed in Figure 4-12 and Figure 4-13, moreover the same confirms that both DGs are equally sharing the load power;

- In presence of reactive power load and considering a mainly resistive grid impedance the steady state frequency error is negative;

- Direct droop scheme based on phase angle shifting has no impact on the frequency, which is kept at the nominal value. This is shown in the first subplot of Figure 4-12. Such a feature seems very interesting for controlling a MG with primary control layer only, in case of traditional droop characteristics (ϑ/P and Q/V) supposing load dominated by active power rather than reactive power. On the other hand such control strategy would

not fit to load shedding protections based on the frequency value and for concurring to the regulation through traditional renewable based DGs exploiting OverFrequency active Power Curtailment method (also defined by SMA as Frequency Shift Power Control [92] for the integration of PVI into the MGs);

- The reactive power profiles of L1 and L2 loads, sharing the same Point of Coupling, in both direct droop cases is affected by a ripple. Such behaviour turns out unexpected for the Constant Power Load L1. It is interesting noticing in the enlargement proposed in Figure 4-15 that the ripples appear in counterphase at the fundamental frequency. Evidently the power delivered by the sources is instead constant;

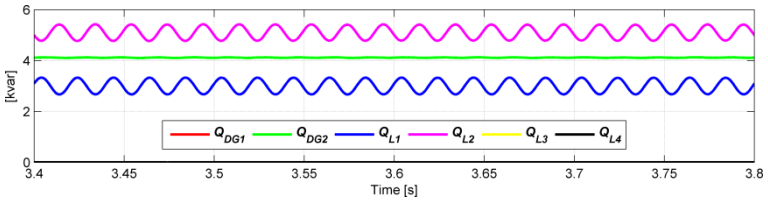

Figure 4-15: enlargement of reactive power profiles in the direct droop control case based on angle bias.

- All proposed schemes appear to be robust with respect to harmonic loads. Nevertheless it is interesting to highlight that power quality is poor whenever operating the MG at no load, as shown in the enlargements of Figure 4-16, referred to direct droop control scheme response. This is mainly due to the fact that in this condition the output voltage corresponds to the voltage on the shunt branch of the filter, therefore it is affected by the switching ripple. As soon as the VSC starts providing current to the MG the output voltage results almost perfectly sinusoidal as shown in the right subplot of Figure 4-16;

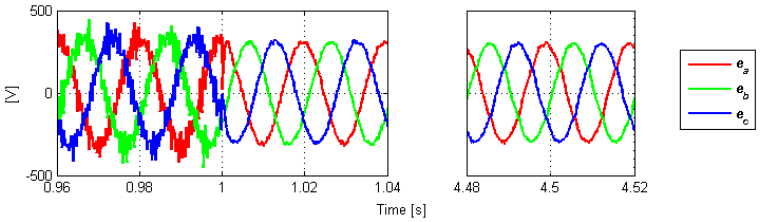

Figure 4-16: phase to ground voltage profiles in the phase angle droop scenario shown in Figure 4-12.

- On the other hand inverse droop scheme turned out:
  - Inadequate in case of no load or in presence of a single DG feeding the loads, respectively shown in the time windows spanning between 0 s and 1 s and between 5 s and 6 s. In particular in the first case the DG is evidently forced to operate in overmodulation;

- Reaching the control purposes in presence of loads and different DGs concurring to the MG control. Nevertheless the resulting power quality appears not fully satisfactory, especially at low loadings.

With reference to the inverse droop scenario shown in Figure 4-14 between 1 s and 5 s it is remarkable since it could represent the case of islanding of a distribution feeder in the absence of anti-islanding method enabled DGs. For such a reason the grid operators recommend decoupling over time the droops of grid connected DGs [93].

4.2.2 INTENTIONAL ISLANDING

Traditional Under-Frequency-Load-Shedding (UFLS) schemes involve parts of the power system as DNs. Nevertheless parts of them could be self sufficient due to on-site balancing between loads and DGs. On the other hand specific power quality requirements could imply swapping cluster of loads from grid connected mode to islanded mode during grid contingencies.

In this paragraph the behaviour in case of a system under-frequency event triggering an UFLS and the consequent transition to intentional islanding of a distribution feeder are shown. Flexible units under this scenario can support the network according to grid codes and then later, once part of shedded network, they can play the role of managing the islanded system. This paragraph despite 4.2.1 aims to show the transient and islanded management in presence of secondary control. The comparison between direct droop control scheme with phase angle bias and inverse droop control schemes is here continued. In this work the communication layer is disregarded and no communication delays are taken into account.

As known from power system theory the *secondary control* [27] allows cancelling the steady state frequency and voltage, at a given network node, errors due to primary control. Despite synchronous generators and inverse droop scheme implementing the secondary control doesn't imply adding an integral branch to the primary control schemes. Indeed it is imperative to note that through direct droop control schemes the voltage and frequency control is indirectly achieved through power regulations. Therefore it is necessary adding a further control structure that modifies directly the references of the three phase generator. As described in section 4.2.1 the direct droop scheme based on phase angle bias naturally maintains the frequency constant, therefore only the control scheme biasing the voltage must be added, as shown in Figure 4-17.

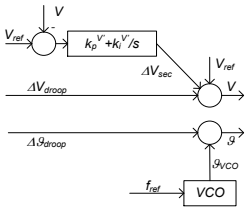

Figure 4-17: secondary control for direct droop control scheme with phase angle bias.

It is to be noted that the control scheme in Figure 4-17 represents a redundancy loop with respect to the voltage regulator. Indeed a null steady state voltage error regulation could be simply obtained by operating the same unit as a master. Latter approach on the other hand would jeopardize system security, since a contingency occurring in the master unit would imply operating the system in absence of a grid forming source.

As mentioned in paragraph 3.3.3 the power control is normally attained through current controlled units for industrial products. It is interesting to highlight that it can be obtained through voltage controlled units too for both grid connected and islanded modes as described in [35] and shown in the control scheme of Figure 4-18.

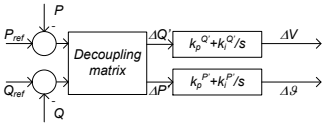

Figure 4-18: power control scheme for a voltage source unit.

On the other hand it must be noted that phase drooped control doesn't fit to industrial products operated in grid connected mode, since natural grid frequency deviations could interphere with the control loop performances. Indeed with reference to Figure 4-8 the reference phase angle for the three phase generator is given by:

$$\vartheta = \Delta\vartheta + mod\left\{2\pi\int f_{ref}\,dt; 2\pi\right\} \tag{4.10}$$

Evidently this control scheme cannot adapt to grid frequency deviations, unless indirectly through the power regulator output term $\Delta\vartheta$. Such power control on the other hand turns out of practical use in islanded mode, since it avoids swapping from hierarchical control to current control. The tuning of this regulator is fully described in [35], in a nutshell the designer aware of the orthogonal transformation in (4.5), has to linearize the equations (4.6):

$$\frac{\partial P'}{\partial \vartheta_h} = \frac{V_h V_k}{z} cos\,\vartheta_h$$
$$\frac{\partial Q'}{\partial V_h} = \frac{2V_h - V_k\,cos\,\vartheta_h}{z} \quad (4.11)$$

Moreover the power averaging effect over a fundamental period and the filter applied to the measured powers should be taken into account. In this way two PI regulators with the parameters listed in Table 4-4 can be defined:

Table 4-4: power regulator parameters.

$k_p^{P'}$ [rad/VA]	7.85e-5
$k_i^{P'}$ [rad/VAs]	0.001
$k_p^{Q'}$ [V/VA]	0.002
$k_i^{Q'}$ [V/VAs]	0.1

Such control scheme is here exploited for restoring the pre-islanding dispatched power of the MT when the battery takes over the MG control through the secondary control. In this case indeed the direct droop scheme would not deliver anymore power.

The comparison is carried out considering a slightly modified residential feeder of CIGRE C6.04.02 benchmark network [81], as shown in Figure 4-19. The feeder is populated by two flexible DGs, two ideal PV units producing 40 kW not participating to the primary control and symmetrical loads. All DGs are represented through VSC switching models. Only three-phase Constant Power Loads are regarded and their powers were scaled down by 33% with respect to the benchmark network in order to maintain the power balance in the islanded feeder.

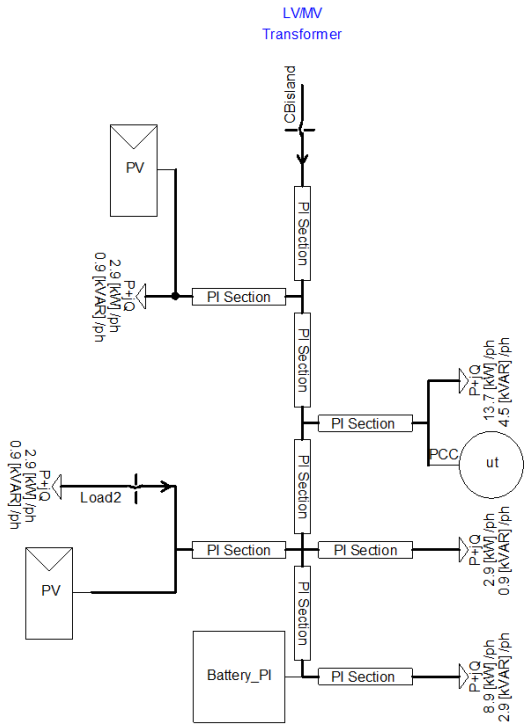

Figure 4-19: Single Line Diagram of modified C6.04.02 residential feeder.

The UFLS occurs when the frequency drops below 49.5 Hz by means of a frequency sensitive Circuit Breaker (CB) located upstream to the feeder. In the next simulations the power references for MT and EVB are kept respectively 30 kW and 0 kW.

Initially the feeder operates in grid connection mode therefore the units track their power set-points. At 1.5 s the mains frequency starts ramping down and the flexible DGs support the network with a power-frequency droop of 0.4 pu/Hz with respect to their nominal power (80 kW), without any dead-band. Once the frequency braches UFLS threshold (at 49 Hz) at 2.5 s, the feeder circuit breaker operates and the flexible DGs swap automatically to droop control in islanded mode, assuming a null equivalent grid impedance angle. Such operation implies swapping also from current controlled to hierarchical control for the angle based droop DGs scenario, while for the direct droop one an overall gain rescheduling is actuated.

At 3.5 s the storage unit starts operating the secondary control, while at 5.5 s a disconnection of a 9 kVA - cosϕ=0.95 load follows (ΔL=-8.2% of the overall MG loading).

System responses with angle based direct drops and with inverse droop control schemes for both the flexible DGs are proposed in Figure 4-20.

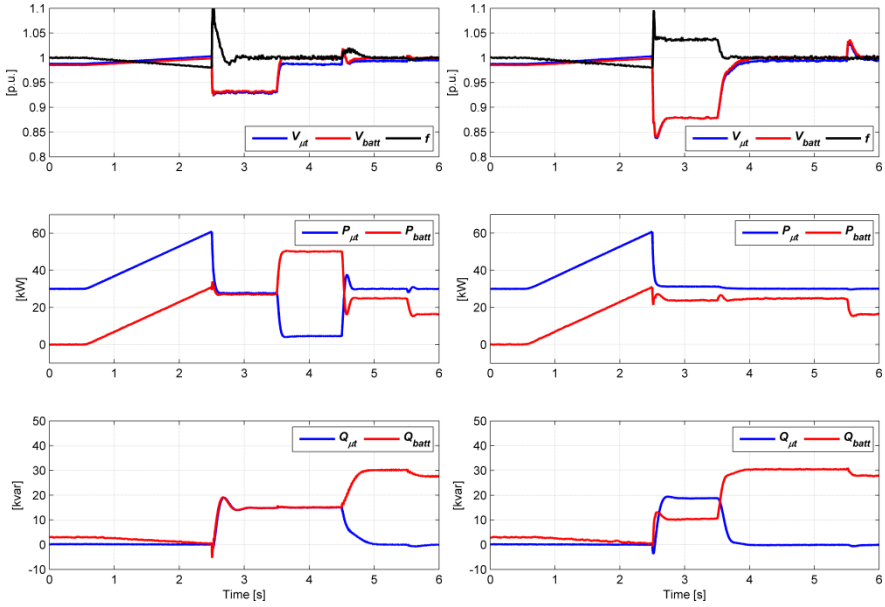

Figure 4-20: comparison of flexible DGs control schemes in case of intentional islanding consequent to UFLS. Transition to islanded mode with direct drooped DGs on the left and with inverse drooped DGs on the right.

The plots in Figure 4-20 leads to following observations:

- The support in grid connected mode is equivalent since both cases rely on the current control scheme;
- The abrupt passage to droop control in both scenario determines a significant frequency transient deviation;
- The operation in power droop confirms the observations proposed in 4.2.1. Despite the analyses in 4.2.1 in this case the results comparison is not straightforward, since the inverse drooped MT receives a non zero active power reference;
- The activation of the secondary control in the network managed through direct droops implies almost nulling the power output of the units operated with primary control. This is an outstanding difference with respect to inverse droop, similar to synchronous generators. For this reason in the scenario of direct droop managed island at 4.5 s the MT is started operated as a dispatchable source through the scheme in Figure 4-18;
- The steady state values after 4.5 s of two scenarios well match;

- Assuming a null impedance angle turned out a reasonable choice leading to a stable system;
- The severity of the voltage variation consequent to the load disconnection at 5.5 s is much larger for the inverse drooped DGs respect to direct one. This is deemed due to the stiff control of the voltage and frequency in secondary controlled direct droop unit. Such control results indirectly achieved with the inverse droop control scheme, even with secondary control enabled, since it relies on the grid following unit principle. In this sense considering a derivative term in the voltage regulator of the secondary unit, making it a PID, could contribute in reducing the peak value but on the other hand implies consequent damped voltage swings. This is shown in Figure 4-21, where same scenario considered for Figure 4-20 was run with different derivative term k_d values. It is to be noted that such derivative term emulates the inertia effect of synchronous generators on the system frequency.

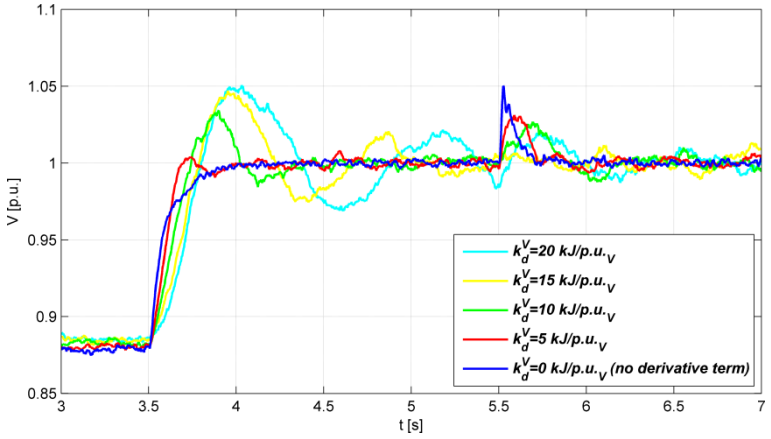

Figure 4-21: effect of derivative term on the battery unit voltage regulator in the inverse droop scheme (© 2013 IEEE).

This turns out a further clue proving the lower large stability of inverse droop respect to direct one. On the other hand the parallel operation of different VSC confirms being beneficial for improving the large signal stability in case of inverse drooped managed MG.

4.3 CONCLUSIONS

This chapter gives evidence about the feasibility of intentional islanding and management of the MG through LV flexible units. Both MT and SBU proposed models don't allow precisely evaluating the ramp response but they turn out fitting to integration studies. In particular the MT model appears well behaving respect to step

load changes, maintaining the shaft speed close to the reference value. The proposed battery model instead has performances similar to [57], adopted by [13] too, but it starts directly from cell manufacturer curves. This model likely fits to Vehicle To Grid applications and more in general to stationary battery units supporting the network during both grid connected and islanded modes.

On the other hand this chapter deals as well with the hierarchical control of such VSC interfaced sources. In particular the adoption of the decoupling matrix is here considered, assuming purely resistive grid impedance in islanded mode. Latter consideration is only an approximation but turned out enough correct for the islanded residential feeder of CIGRE benchmark network. Previous literature confirmed that wrong grid impedance increases the risk of instability but no similar problems occurred in the studied cases. The chapter instead focuses on the comparison of different droop schemes for the overall hierarchical control of the MG. Both direct droop control schemes, through frequency bias and angle bias, turned out fitting to the MG control. It is interesting pointing that second method allows maintaining a constant frequency, therefore it doesn't fit in case of traditional droops to the support at the primary control by standard renewable sources operating overfrequency power curtailment. Moreover these control schemes were compared with the MG management through reverse drooped VSCs. This control scheme derived from synchronous generators, which are voltage sources, is normally relegated only to current controlled VSCs for grid following units. Such consideration holds whenever the MG is fed by a single reverse drooped unit or in case it operates at no load: in both cases the reverse droop turns out not suitable for a stable MG management. On the other hand parallel reverse drooped VSCs appears properly maintaining the MG control. The comparison between direct and reverse droop schemes is operated in presence of primary control and different types of loads initially and later for surviving an intentionally islanded distribution feeder operating also the battery unit through secondary control. Minor changes were necessary to direct droop scheme for achieving the secondary control and dispatching the reference power through the unit supporting the primary regulation only. The islanding scenario, followed by primary and secondary regulation stages, highlighted a poor voltage control of the reverse droop scheme with secondary control in presence of load disturbances. This drawback was tackled effectively adding a derivative term to the voltage regulator, with an effect similar to the inertia emulation. The study was performed through multiple runs, each one featured by a different predefined value of the derivative parameter.

This chapter therefore proofed the possibility to manage a hierarchically controlled MG through different control schemes exploiting LV flexible units. On the other hand the overall chapter, even if relying on the analytical tuning of the inner loops of the VSC proposed in the former chapter, shows the different hierarchical control

schemes responses in the time domain, in one case through parametric multiple simulations. Just the crosschecking of a detailed Laplace study and properly optimized multiple runs is the focus of next chapter.

The contents of this chapter could be further deepened tackling the grid impedance estimation and the effects of the adoption of different values for the decoupling matrix in different units. Moreover the effects of unbalanced loads and communication infrastructure give further room for extending this chapter.

CHAPTER 5

REACTIVE POWER CONTROLLER FOR DISTRIBUTED SYNCHRONOUS GENERATORS

Traditional control of synchronous generators is designed in order to deliver active power and support voltage and frequency regulations. Nevertheless a synchronous generator could be controlled differently based on specific needs. Some grid code regulations for example demands to control the dispatched reactive power or to operate at constant power factor. Such operating modes are expected to become more and more frequent in the future scenario of virtual power plants [94]. The cluster aggregator in fact could demand SG dispatching reactive power in the context of participation to local reactive power market. Another case where traditional synchronous generator control could be revolutionized is represented by mainly resistive islanded networks, ruled by inverse droops characteristics, where the share of SGs turns out scarce respect VSC interfaced units [95].

In this chapter the adoption of an outer reactive power loop is proposed, relying on a PI regulator, biasing the voltage reference of traditional exciters. The study is performed considering a 100 kVA Diesel Generator Set connected to a LV feeder modelled as an infinite bus system and equipped with a brushless exciter but it can be extended to any type of SG. Main contribution is represented by the comparison of two different tuning techniques: one based on a couple of novels objective functions for optimization enabled time domain simulations and the second relying on the traditional pole placement method applied to the linearized system model. For this purpose an extension of the K-parameter model [27, 96] is proposed taking into account the impact of reactance to resistance ratio of the interconnecting equivalent line. The optimization enabled time domain simulations are performed in PSCAD®.

The contents of this chapter are presented in [97].

5.1 REACTIVE POWER CONTROLLER

Mimic a current controlled source through a Synchronous Generator, just as VSC interfaced DGs, is possible adding a reactive power regulator. Normally in fact the active power is already controlled for dispatching reasons.

In this chapter an external reactive power regulator is proposed with the aim of biasing the voltage reference of the AVR, as shown in Figure 5-1. It is to be noted that such architecture derives from traditional knowledge of power systems, where voltage variations heavily affect the reactive power flow through the lines. In order to evaluate the effects of impedance network angle and module in case of distribution network following research was carried out.

The DE prime mover has been modelled with a first order actuator and a delay representing the combustion process according to [98-100].

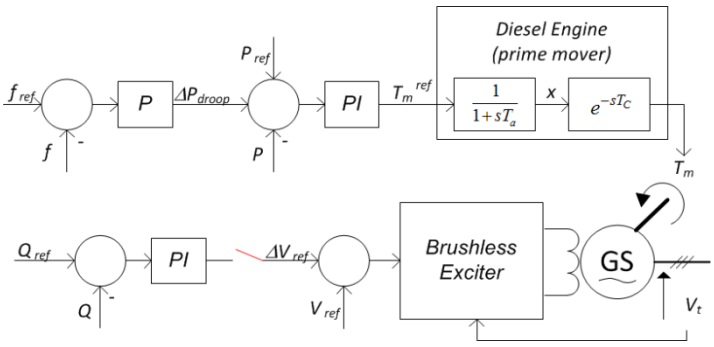

Figure 5-1: conceptual control scheme (© 2016 IEEE).

For the sake of simplicity a radial system is considered hereafter, as shown in the left side of Figure 5-2, which can be easily reduced to the corresponding Thevenin equivalent, as in the right side of the same picture. This scheme is traditionally referred as single bus bar system.

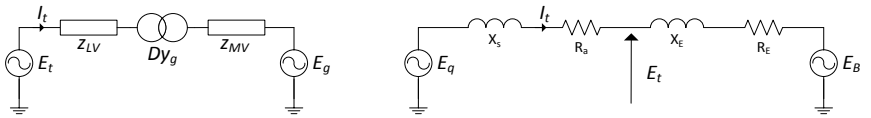

Figure 5-2: infinite bus system: radial distribution network on the left and its Thevenin equivalent on the right.

From the basic load flow equation applied to the SG node, towards the grid node:

$$\overline{S_{tB}} = P_{tB} + j \cdot Q_{tB} = \frac{E_t^{\,2}}{z}\left[cos\,\varphi_z + j \cdot sin\,\varphi_z\right] - \frac{E_t E_B}{z}\left[cos\left(\varphi_z + \varphi_t\right) + j \cdot sin\left(\varphi_z + \varphi_t\right)\right] \quad (5.1)$$

Considering the grid as a slack node of voltage E_B and the synchronous generator acting as a PQ node, whose powers are P_{tB}, Q_{tB}, equation (5.1) is solved making use of [14] for a subsets of impedance angle and module values. Such approach, not directly implementing classical Newton-Raphson method, doesn't lead to find the Jacobian elements $\frac{\partial P_{tB}}{\partial E_t}$ and $\frac{\partial Q_{tB}}{\partial E_t}$. Instead they are computed separately as:

$$\frac{\partial P_{tB}}{\partial E_t} = \frac{2E_t\,cos\,\varphi_z - E_B\,cos\left(\varphi_z + \varphi_t\right)}{z} \quad (5.2)$$

$$\frac{\partial Q_{tB}}{\partial E_t} = \frac{2E_t\,sin\,\varphi_z - E_B\,sin\left(\varphi_z + \varphi_t\right)}{z} \quad (5.3)$$

With per unit treatise and considering $P_{tB} = 0.5\,p.u.; Q_{tB} = 0.1\,p.u$ the terminal voltage E_t and voltage angle φ_t are respectively shown in Figure 5-3 and Figure 5-4. Moreover in Figure 5-5 and Figure 5-6 the voltage dependent Jacobian terms $\frac{\partial P_{tB}}{\partial E_t}$ and $\frac{\partial Q_{tB}}{\partial E_t}$ are proposed.

These figures highlight:

- $\frac{\partial P_{tB}}{\partial E_t} \approx 0$ in the case of mainly inductive lines $\left(\varphi_z \approx 90°\right)$, hypothesis on the base of which relies the Fast Decoupled Load Flow simplification;
- $\frac{\partial Q_{tB}}{\partial E_t} \approx 0$ for mainly resistive lines $\left(\varphi_z \approx 0°\right)$;
- Lower short circuit power at synchronous generator terminals, in other terms higher impedance module values, reduces both considered Jacobian elements, otherwise increases both sensitivities with respect to terminal machine voltage.

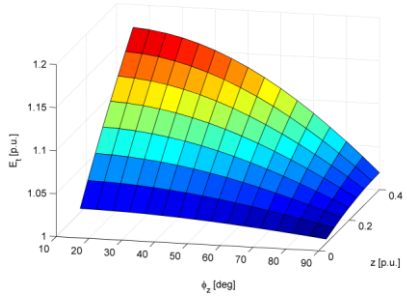

Figure 5-3: $E_t\big|_{P_{tB}=0.5\,p.u.;Q_{tB}=0.1\,p.u}$

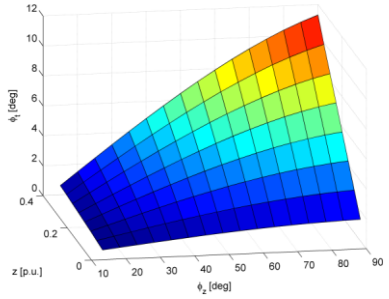

Figure 5-4: $\varphi_t\big|_{P_{tB}=0.5\,p.u.;Q_{tB}=0.1\,p.u}$

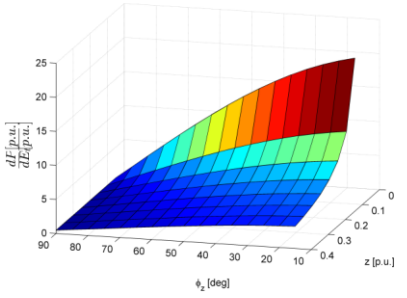

Figure 5-5: $\left.\dfrac{\partial P_{tB}}{\partial E_t}\right|_{P_{tB}=0.5\,p.u.;Q_{tB}=0.1\,p.u}$

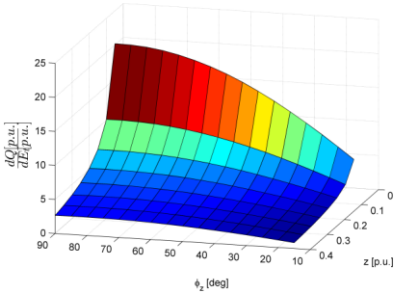

Figure 5-6: $\left.\dfrac{\partial Q_{tB}}{\partial E_t}\right|_{P_{tB}=0.5\,p.u.;Q_{tB}=0.1\,p.u}$

Therefore it can be concluded that proposed reactive power regulator would lead to rather high reference voltages for the AVR in case of very resistive equivalent network. This phenomenon doesn't occur in presence of step up distribution transformers, while it could happen with transformerless LV MGs. On the other hand it is to be noted that the voltage variation is dependent on both active and reactive power variations components. Indeed Jacobian and perturbations are linked by (5.4) useful for the comprehension of the results shown in the following paragraphs.

$$\begin{bmatrix}\Delta P\\ \Delta Q\end{bmatrix}=\begin{bmatrix}\dfrac{\partial P}{\partial \varphi_t} & \dfrac{\partial P}{\partial E_t}\\ \dfrac{\partial Q}{\partial \varphi_t} & \dfrac{\partial Q}{\partial E_t}\end{bmatrix}\begin{bmatrix}\Delta\varphi_t\\ \Delta E_t\end{bmatrix}=J\begin{bmatrix}\Delta\varphi_t\\ \Delta E_t\end{bmatrix} \tag{5.4}$$

5.2 MACHINE EQUATIONS

5.2.1 SYNCHRONOUS GENERATOR EQUATIONS

The treatise of synchronous generator equations is rather common [27, 101, 102] . This paragraph is intended for brushing up the meaning of machine parameters, with particular reference to PSCAD® model mask, and for highlighting the assumptions made for obtaining the small signal model.

Hereinafter the scheme of Figure 5-7 will be considered, as well as the followings:

- per unit (p.u.) notation, considering machine rated voltage and power as base values;
- equations in the transformed Park domain d-q, where 0 sequence component is neglected. The q-axis is going to be considered aligned to the internal machine voltage E_q;
- a salient rotor, therefore a single damper winding (so called ammortisseur) is present;
- negligible subtransient inductances;

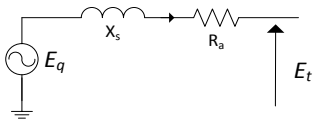

Figure 5-7: simplified synchronous generator model.

Under previous conditions shall be defined:

- Stator voltage equations:

$$\begin{aligned} e_d &= p\psi_d - \psi_q \omega_r - R_a i_d \\ e_q &= p\psi_q + \psi_d \omega_r - R_a i_q \end{aligned} \tag{5.5}$$

- Rotor voltage equations:

$$\begin{aligned} e_{fd} &= p\psi_{fd} + R_{fd} i_{fd} \\ 0 &= p\psi_{1d} + R_{1d} i_{1d} \\ 0 &= p\psi_{1q} + R_{1q} i_{1q} \end{aligned} \tag{5.6}$$

- Stator flux linkage equations:

$$\begin{aligned} \psi_d &= -(L_{ad} + L_l) i_d + L_{ad}(i_{fd} + i_{1d}) \\ \psi_q &= -(L_{aq} + L_l) i_q + L_{aq} i_{1q} \end{aligned} \tag{5.7}$$

- Rotor flux linkage equations:

$$\begin{aligned}\psi_{fd} &= L_{ffd} i_{fd} + L_{f1d} i_{1d} - L_{ad} i_d \\ \psi_{1d} &= L_{f1d} i_{fd} + L_{11d} i_{1d} - L_{ad} i_d \\ \psi_{1q} &= L_{11q} i_{1q} - L_{aq} i_q\end{aligned} \tag{5.8}$$

- Air-gap torque

$$T_e = \psi_d i_q - \psi_q i_d \tag{5.9}$$

Where the subscripts *a, l, fd* and *1* respectively refers to armature (stator), leakage inductance, field circuit and to the damper circuit.

The treatise can be eased considering following rotor circuit per unit inductances:

$$\begin{aligned}L_{fd} &= L_{ffd} - L_{f1d} \\ L_{1d} &= L_{11d} - L_{f1d} \\ L_{1q} &= L_{11q} - L_{aq}\end{aligned} \tag{5.10}$$

Substituting the terms declared in (5.10) in equations (5.8), allow deducing the equivalent circuits of Figure 5-8. Here can be easily recognized PSCAD® parameters belongings to the "Equivalent circuit data format" tab:

- R_a armature resistance;
- L_l stator leakage inductance;
- L_{ad} and L_{aq} d and q axis unsaturated magnetizing inductances (not to be confused with L_d and L_q);
- $L_{f1d} - L_{ad}$ Field and damper mutual leakage inductance;
- L_{1d} and L_{1q} d and q axis damper leakage inductances;
- R_{1d} and R_{1q} damper resistances respectively at d and q axis;
- L_{fd} field leakage inductance;
- R_{fd} field resistance;

It must be noted that aforementioned inductances correspond to respective reactances since p.u. notation is assumed.

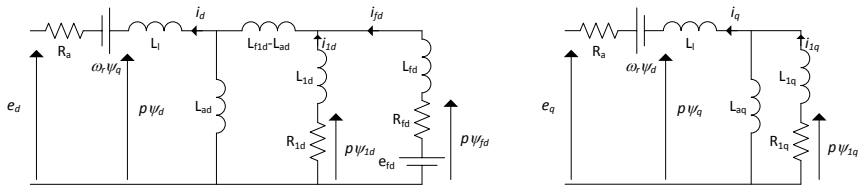

Figure 5-8: d and q axis equivalent circuits.

For power system studies different parameters are frequently considered, which are introduced as follows:

$$\begin{aligned} L_d &= L_l + L_{ad} \\ L_q &= L_l + L_{aq} \end{aligned} \tag{5.11}$$

Nevertheless for stability studies the equivalent circuit is usually simplified neglecting:

- series inductance representing flux linkage between field winding and ammortisseur;
- ammortisseur effects;
- speed deviations $p\omega_r = 0$;
- time derivative of flux linkages $p\psi = 0$;

Under these assumptions d-axis mutual flux linkage can be expressed as:

$$\psi_{ad} = L_{ad}\left(i_{fd} - i_d\right) = -L_{ad} i_d + \frac{L_{ad}}{L_{fd}}\left(\psi_{fd} - \psi_{ad}\right) = L_{ad}{}'\left(-i_d + \frac{\psi_{fd}}{L_{fd}}\right) \tag{5.12}$$

Where:

$$L_{ad}{}' = \frac{L_{ad} L_{fd}}{L_{ad} + L_{fd}} \tag{5.13}$$

And analogously for q-axis:

$$L_{aq}{}' = \frac{L_{aq} L_{1q}}{L_{aq} + L_{1q}} \tag{5.14}$$

Stator and rotor flux linkage equations (5.7) and (5.8) become:

$$\begin{aligned} \psi_d &= -L_l i_d + L_{ad}(i_{fd} - i_d) = -L_l i_d + \psi_{ad} \\ \psi_q &= -(L_{aq} + L_l) i_q = -L_l i_q + \psi_{aq} \\ \psi_{fd} &= \psi_{ad} + L_{fd} i_{fd} \end{aligned} \tag{5.15}$$

Similarly to (5.11) the transient inductances are defined:

$$\begin{aligned} L_d' &= L_l + L_{ad}' \\ L_q' &= L_l + L_{aq}' \end{aligned} \tag{5.16}$$

So far saturation effects, affecting mutual inductances, were not mentioned but they play a significant role in real machines. In the PSCAD® model however they are not taken into account. This implies from here on the equivalence of unsaturated and saturated values. The former are going to be denoted by an additional *u* subscript, while the latters with an *s*.

$$\begin{aligned} L_{ad} &= k_{ad} L_{adu} = L_{adu} \\ L_{aq} &= k_{aq} L_{aqu} = L_{aqu} \end{aligned} \tag{5.17}$$

$$\begin{aligned} L_{ads} &= L_{adu} \\ L_{aqs} &= L_{aqu} \end{aligned} \tag{5.18}$$

According to (5.13) is therefore introduced:

$$L_{ads}' = \frac{L_{ads} L_{fd}}{L_{ads} + L_{fd}} \tag{5.19}$$

5.2.2 AC5A EXCITER

Distributed synchronous generators are usually equipped with brushless exciters for reducing maintenance costs [103]. In this work the AC5A model, as defined by IEEE standard [104], is considered. Its control scheme is shown in the left side of Figure 5-9.

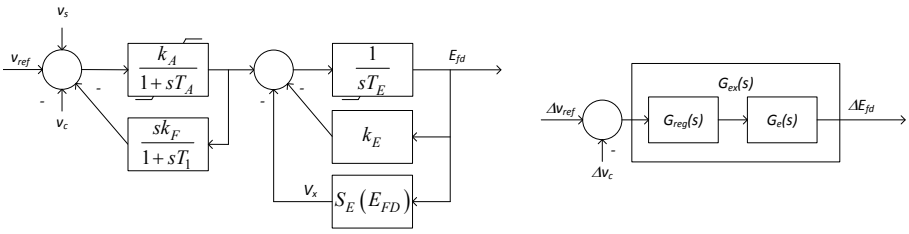

Figure 5-9: AC5A control scheme (on the left) and equivalents (on the right).

Under following simplifications the scheme on the right side of Figure 5-9 is derived:

- saturation-loading effects are neglected, setting a constant V_x term, regardless from E_{fd};

- limiters are not taken into account;
- no power system stabilizer;

Where:

$$G_{reg}(s) = \frac{k_A(1+sT_1)}{T_A T_1 s^2 + (T_A + T_1 + k_A k_F) + 1} \tag{5.20}$$

$$G_e(s) = \frac{1}{(k_E + S_E) + sT_E} \tag{5.21}$$

$$G_{ex}(s) = G_{reg}(s) G_e(s) \tag{5.22}$$

5.3 INFINITE BUS SYSTEM – STEADY STATE EQUATIONS

Considering the network of Figure 5-2 and using power flow equation (5.1), E_t and φ_t can be calculated. Such step, computed through a MATLAB® script, allows defining the initial values for the PSCAD® simulation.

The current and power angle expressions are defined as below:

$$I_t = \frac{\sqrt{P_t^2 + Q_t^2}}{E_t} \tag{5.23}$$

$$\Phi = \angle\overline{E_t} - \angle\overline{I_t} = a\tan\frac{Q_t}{P_t} \tag{5.24}$$

Considering the phasor diagram of Figure 5-10 following definitions useful this treatise can be introduced:

- Internal rotor angle δ_i :

$$\delta_i = \angle\overline{E_q} - \angle\overline{E_t} \tag{5.25}$$

- Rotor angle δ :

$$\delta = \angle\overline{E_q} - \angle\overline{E_B} = \delta_i + \varphi_t \tag{5.26}$$

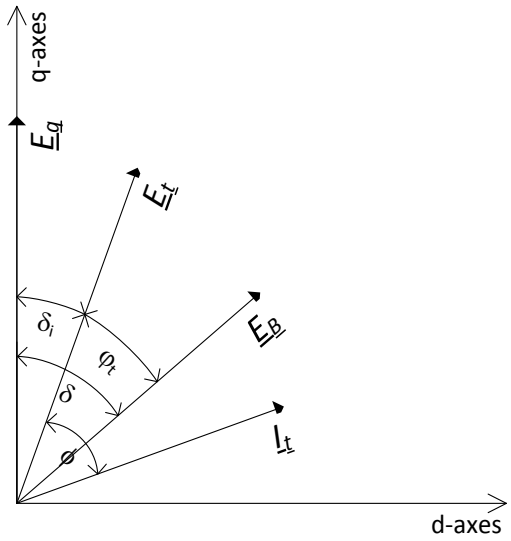

Figure 5-10: phasor diagram (© 2016 IEEE).

Neglecting ψ_d and considering steady state conditions, equation (5.5) permits stating the internal rotor angle as:

$$\delta_i = a\tan\left(\frac{x_q I_t \cos\Phi - R_a I_t \sin\Phi}{E_t + R_a I_t \cos\Phi + x_q I_t \sin\Phi}\right) \tag{5.27}$$

Heading to the overall small signal analyses, the infinite bus system equation is considered, following the approach of [27]:

$$\overline{E_t} = \overline{E_B} + \left(R_E + jX_E\right)\overline{I_t} \tag{5.28}$$

Regarding the transformed d-q domain, with q-axis aligned to $\overline{E_q}$, the projection of $\overline{I_t}, \overline{E_t}$ and $\overline{E_B}$ on the system axis can be easily found:

$$\begin{aligned}
&\overline{E_t} = e_d + je_q = E_t \sin\delta_i + jE_t \cos\delta_i \\
&\overline{I_t} = i_d + ji_q = I_t \sin\left(\delta_i + \Phi\right) + jI_t \cos\left(\delta_i + \Phi\right) \\
&\overline{E_B} = E_B \sin\delta + jE_B \cos\delta
\end{aligned} \tag{5.29}$$

From equations (5.5), neglecting time derivative terms and considering $\omega = 1 p.u.$, and (5.7), without taking into account the ammortisseur effects, the terminal voltage components can be rewritten as:

$$\begin{aligned} e_d &= -R_a i_d - (-L_l i_q + \psi_{aq}) \\ e_q &= -R_a i_q - (L_l i_d - \psi_{ad}) \end{aligned} \tag{5.30}$$

Current components turn out as below:

$$\begin{aligned} i_d &= \frac{X_{Tq}\left[\psi_{fd}\left(\frac{L_{ads}}{L_{ads}+L_{fd}}\right) - E_B \cos\delta\right] - R_T E_B \sin\delta}{D} \\ i_q &= \frac{R_T\left[\psi_{fd}\left(\frac{L_{ads}}{L_{ads}+L_{fd}}\right) - E_B \cos\delta\right] + X_{Td} E_B \sin\delta}{D} \end{aligned} \tag{5.31}$$

Where following parameters were introduced:

$$\begin{aligned} R_T &= R_a + R_E \\ X_{Tq} &= X_E + (L_{aqs} + L_l) = X_E + X_{qs} \\ X_{Td} &= X_E + (L_{ads}' + L_l) = X_E + X_{ds}' \\ D &= R_T^2 + X_{Tq} X_{Td} \end{aligned} \tag{5.32}$$

Moreover the internal voltage E_q can be stated on the base of the equivalent circuit of Figure 3-7:

$$E_q = e_q + R_a i_q + X_{qs} i_d \tag{5.33}$$

5.4 SMALL SIGNAL ANALYSES

Complete small signal analyses of a synchronous generator is proposed in [27, 96] leading to so called K-parameters model. Traditional treatise includes the effect of saturation, here neglected, and it takes into account the AVR model and single bus-bar system. For sake of simplicity the definition of K-parameters is here re-proposed.

$$m_1 = \frac{\partial i_d}{\partial \delta} = \frac{E_B\left(X_{Tq}\sin\delta_0 - R_T\cos\delta_0\right)}{D} \tag{5.34}$$

$$m_2 = \frac{\partial i_d}{\partial \psi_{fd}} = \frac{X_{Tq} L_{ads}}{D\left(L_{ads}+L_{fd}\right)} \tag{5.35}$$

$$n_1 = \frac{\partial i_q}{\partial \delta} = \frac{E_B\left(R_T\sin\delta_0 + X_{Td}\cos\delta_0\right)}{D} \tag{5.36}$$

$$n_2 = \frac{\partial i_q}{\partial \psi_{fd}} = \frac{R_T L_{ads}}{D\left(L_{ads} + L_{fd}\right)} \tag{5.37}$$

$$K_1 = \frac{\partial T_e}{\partial \delta} = E_{q0} n_1 + i_{q0}\left(X_q - X_d{}'\right) m_1 \tag{5.38}$$

$$K_2 = \frac{\partial T_e}{\partial \psi_{fd}} = \frac{L_{ads}}{L_{ads} + L_{fd}}\left[\frac{R_T}{D} E_{q0} + \left(\frac{X_{Tq}\left(X_q - X_d{}'\right)}{D} + 1\right) i_{q0}\right] \tag{5.39}$$

$$K_3 = \frac{L_{ads} + L_{fd}}{L_{adu}\left[1 + \frac{X_{Tq}}{D}\left(X_d - X_d{}'\right)\right]} \tag{5.40}$$

$$T_3 = \frac{L_{ads} + L_{fd}}{\omega_0 R_{fd}\left[1 + \frac{X_{Tq}}{D}\left(X_d - X_d{}'\right)\right]} \tag{5.41}$$

$$K_4 = \frac{E_B}{D}\left(X_d - X_d{}'\right)\left(X_{Tq}\, sin\,\delta_0 - R_T\, cos\,\delta_0\right) \tag{5.42}$$

$$K_5 = \frac{\partial E_t}{\partial \delta} = \frac{e_{d0}}{E_{t0}}\left[-R_a m_1 + n_1\left(L_l + L_{aqs}\right)\right] + \frac{e_{q0}}{E_{t0}}\left[-R_a n_1 - m_1\left(L_l + L_{ads}{}'\right)\right] \tag{5.43}$$

$$K_6 = \frac{\partial E_t}{\partial \psi_{fd}} = \frac{e_{d0}}{E_{t0}}\left[-R_a m_2 + n_2\left(L_l + L_{aqs}\right)\right] + \frac{e_{q0}}{E_{t0}}\left[-R_a n_2 - L_l m_2 + L_{ads}{}'\left(\frac{1}{L_{fd}} - m_2\right)\right] \tag{5.44}$$

The corresponding control scheme is represented in Figure 5-11, where:

- $G_{field}(s) = \frac{K_3}{1 + sT_3}$ represents the field equations;
- $G_f^V(s) = \frac{1}{1 + sT_V}$ models the filtering effect of voltage measurement.

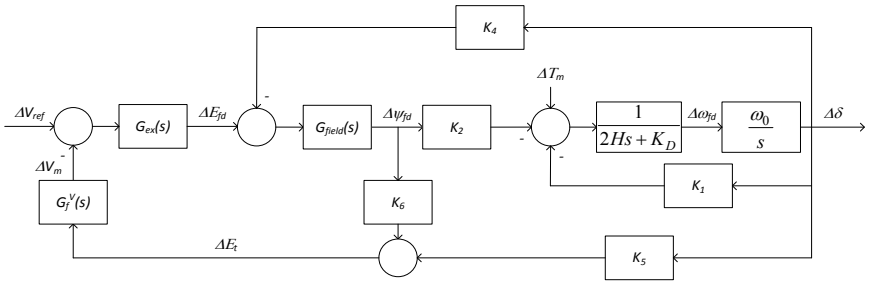

Figure 5-11: "traditional" K-parameter model (© 2016 IEEE).

Hereinafter for simplicity the mechanical equations are expressed in compact form:

$$G_{mec}(s) = \frac{\omega_0}{s(2Hs + K_D)} \tag{5.45}$$

The closed loop transfer function $G_{CL}^{V}(s) = \frac{\Delta V_m}{\Delta V_{ref}}$ turns out:

$$G_{CL}^{V}(s) = \frac{G_{ex}G_f^V G_{field}(k_6 + G_m k_1 k_6 - G_m k_2 k_5)}{G_m k_1 + G_{ex}G_f^V G_{field}k_6 - G_{field}G_m k_2 k_4 + G_{ex}G_f^V G_{field}G_m k_1 k_6 - G_{ex}G_f^V G_{field}G_m k_2 k_5 + 1} \tag{5.46}$$

In order to analytically study the proposed reactive power controller, based on a PI regulator biasing the AVR voltage reference as shown in Figure 5-1, the reactive power expression (5.1) has to be considered:

$$Q = \frac{E_t^2 \sin\varphi_z}{z} - \frac{E_t E_B \sin(\varphi_t + \varphi_z)}{z} \tag{5.47}$$

More commonly known for transmission lines with inductive behaviour as:

$$Q = \frac{E_t(E_t - E_B \cos\varphi_t)}{X_t} \tag{5.48}$$

Keeping the general formulation, suitable to any type of line, and supposing a small perturbation:

$$dQ = \frac{\partial Q}{\partial E_t} dE_t + \frac{\partial Q}{\partial \varphi_t} d\varphi_t \tag{5.49}$$

In (5.49) the $d\varphi_t$ term can be formulated in two different ways, hereinafter referred as *A* and *B methods*.

A method relies on the assumption that reactive power perturbations have no impact on the active power. From (5.4) follows:

$$\Delta\varphi_t = -\frac{\partial P}{\partial E_t}\frac{\partial \varphi_t}{\partial P}\Delta E_t \tag{5.50}$$

Hence the plant transfer function for the reactive power controller is:

$$G_{plant}^{Q(A)} = \frac{\Delta V_{ref}}{\Delta Q_m} = \left(\frac{\partial Q}{\partial E_t} - \frac{\partial Q}{\partial \varphi_t}\frac{\partial P}{\partial E_t}\frac{\partial \varphi_t}{\partial P}\right) G_{CL}^{V}(s) G_f^{Q}(s) \tag{5.51}$$

Where $G_f^Q(s) = \dfrac{1}{1+sT_Q}$ models the smoothing effect of the reactive power meter.

Alternatively *B method* relies on (5.26), which makes (5.49):

$$dQ = \frac{\partial Q}{\partial E_t}dE_t + \frac{\partial Q}{\partial \varphi_t}\left(d\delta - d\delta_i\right) \tag{5.52}$$

Where $d\delta_i$ term can be defined as a function of the dQ:

$$d\delta_i = \frac{\partial \delta_i}{\partial I_t}\cdot dI_t + \frac{\partial \delta_i}{\partial E_t}\cdot dE_t + \frac{\partial \delta_i}{\partial \phi}\cdot d\phi = \frac{\partial \delta_i}{\partial I_t}\cdot\frac{\partial I_t}{\partial Q}\cdot dQ + \frac{\partial \delta_i}{\partial E_t}\cdot\frac{\partial E_t}{\partial Q}\cdot dQ + \frac{\partial \delta_i}{\partial \phi}\cdot\frac{\partial \phi}{\partial Q}\cdot dQ \tag{5.53}$$

Traditional K-parameter block diagram representation can be now expanded as shown in Figure 5-12, where terms:

$$K_7 = \frac{\partial Q}{\partial E_t} = \frac{2E_t \sin\varphi_z - E_B \sin(\varphi_t + \varphi_z)}{z_t} \tag{5.54}$$

$$K_8 = \frac{\partial Q}{\partial \varphi_t} = -\frac{E_t E_B}{z_t}\cos\left(\varphi_t + \varphi_z\right) \tag{5.55}$$

$$K_9 = \frac{\partial \delta_i}{\partial I_t}\cdot\frac{\partial I_t}{\partial Q} + \frac{\partial \delta_i}{\partial E_t}\cdot\frac{\partial E_t}{\partial Q} + \frac{\partial \delta_i}{\partial \phi}\cdot\frac{\partial \phi}{\partial Q} \tag{5.56}$$

Where terms of K_9 can be determined once known the internal rotor angle expression in (5.25) and basic reactive power statement in p.u. notation.

$$const = E_t + R_a I_t \cos\phi + x_q I_t \sin\phi$$

$$\frac{\partial \delta_i}{\partial I_t} = \cos^2 \delta_i \frac{\left(x_q \cos\phi - R_a \sin\phi\right) const - \left(R_a \cos\phi + x_q \sin\phi\right)\left(x_q I_t \cos\phi - R_a I_t \sin\phi\right)}{const^2}$$

$$\frac{\partial \delta_i}{\partial E_t} = -\cos^2 \delta_i \frac{x_q I_t \cos\phi - R_a I_t \sin\phi}{const^2}$$

$$\frac{\partial \delta_i}{\partial \phi} = \cos^2 \delta_i \frac{-x_q I_t \sin\phi - R_a I_t \cos\phi - \left(-R_a I_t \sin\phi + x_q I_t \cos\phi\right)\tan\delta_i}{const} \tag{5.57}$$

$$\frac{\partial I_t}{\partial Q} = \frac{1}{V_t \sin\phi}$$

$$\frac{\partial E_t}{\partial Q} = \frac{1}{I_t \sin\phi} \tag{5.58}$$

$$\frac{\partial \phi}{\partial Q} = \frac{1}{V_t I_t \cos\phi}$$

Above considerations allows defining the "extended" K-parameter model shown in Figure 5-12.

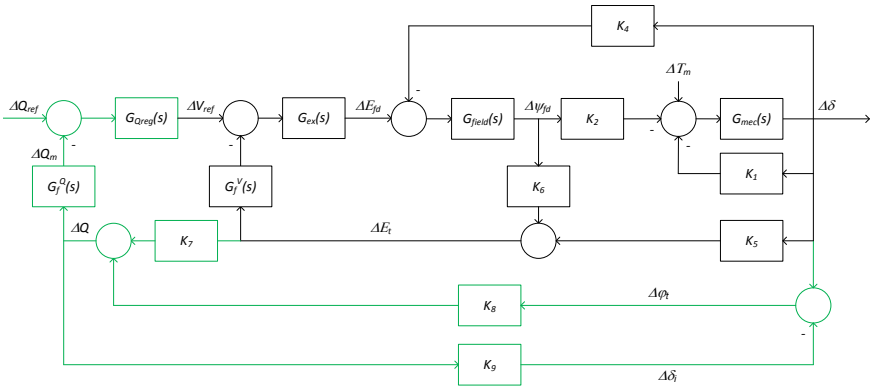

Figure 5-12: "extended" K-parameter model, proposed part outlined in green.

Two possible reduction methods leading to symbolically explicit the closed loop transfer function $G_{CL}^{Q(B)}(s) = \frac{\Delta Q_m}{\Delta Q_{ref}}$ are briefly described in A.4.

5.5 VALIDATION OF SMALL SIGNAL MODELS

An important step towards the comparison of tuning methods is the validation of small signal model found in 5.4. For such a purpose in this paragraph the step response of PSCAD® electrical model and small signal one are compared, in presence of same reactive power regulator and initial conditions. All the system parameters are reported in A.4.

The small signal response is going to be regarded as:

$$y_{small\ \ signal}(t) = y_0 + \Delta y(t) \tag{5.59}$$

Where:

- y_0 is the output at initial conditions, given by power flow equation (5.1);
- $\Delta y(t)$ is the output variation of the extended K-parameter model to a given input;

In order to ease the comparison following considerations were made:

- small perturbation, limiting the effects of the linearization in the small signal model;
- different reactance to resistance scenarios are considered, keeping same impedance module $z_t = 0.0566 p.u. (\Leftrightarrow S_{sc} = 1.77 MVA)$;
- two stages validation, through comparison with time domain response of the electrical system modelled in PSCAD®. First the AVR response is validated, which is followed by the test of the reactive power regulator given k_p, k_i.

While considering only the voltage regulator, the results obtained with two different reactance to resistance ratio scenarios, assuming same short circuit power at SG terminals, are shown in Figure 5-13.

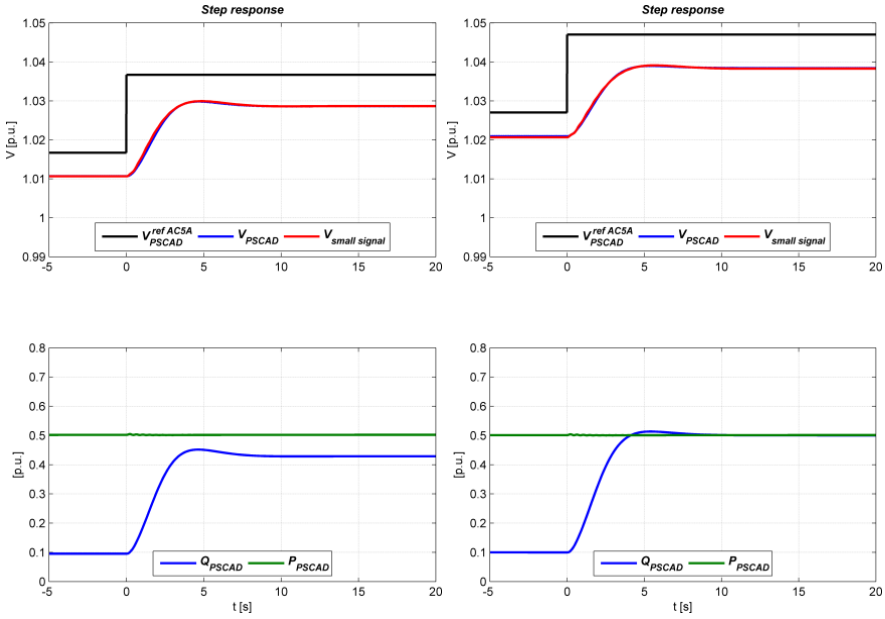

Figure 5-13: ΔV=0.02 p.u. step response, starting from P=0.5 p.u. and Q=0.1 p.u in the scenarios X/R=5, on the left, and X/R=1.37, on the right (© 2016 IEEE).

Relevant observations are:

- symbolic solution of power flow equations (5.1) through MATLAB® is confirmed, since initial conditions of PSCAD® model matches with y_0;
- AC5A exciter performs a no zero steady state voltage error regulation as shown in both cases of Figure 5-13. An analytical explanation is given applying the Final Value Theorem:

$$\Delta e_\infty = \lim_{t\to\infty}\left(V_{ref} - v(t)\right) = \lim_{s\to 0} s\left(1 - G^V_{CL}(s)\right)\frac{\Delta V_{ref}}{s} \tag{5.60}$$

Analysing the closed loop transfer function in (5.46) turns out that it is featured by type $g = 0$, therefore (5.60) becomes:

$$\Delta e_\infty = \left(1 - k_{st}\right)\Delta V_{ref} \tag{5.61}$$

Where the static gain k_{st} results:

$$k_{st} = \frac{k_3 k_A (k_1 k_6 - k_2 k_5)}{S_E k_1 + k_1 k_E + k_1 k_3 k_6 k_A - k_2 k_3 k_5 k_A - k_2 k_3 k_4 k_E - S_E k_2 k_3 k_4} \tag{5.62}$$

For the sake of the reader this is here confirmed with reference to X/R=1.37 scenario of Figure 5-13. The substitution of the parameters in (5.46) leads to the zero pole map shown in Figure 5-14, whose characteristics are summarized in Figure 5-1.

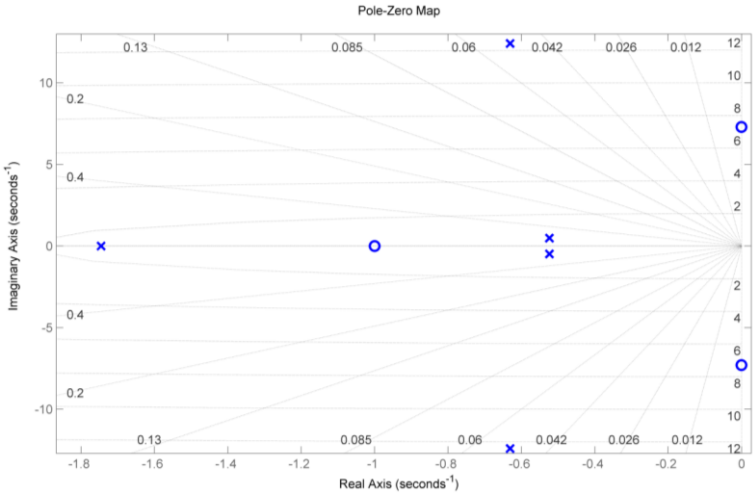

Figure 5-14: zero-pole map of closed loop transfer function $G_{CL}^{V}(s)$ in case X/R=1.37 (enlargement).

Table 5-1: closed loop transfer function characteristics.

Static gain	0.881
Zeros [Hz]	-50 ; -0.0006 ± 7.2928i ; -1
Poles [Hz]	-650.92 ; -50.05 ; -0.63 ± 12.41i ; -1.75 ; -0.52 ± 0.48i

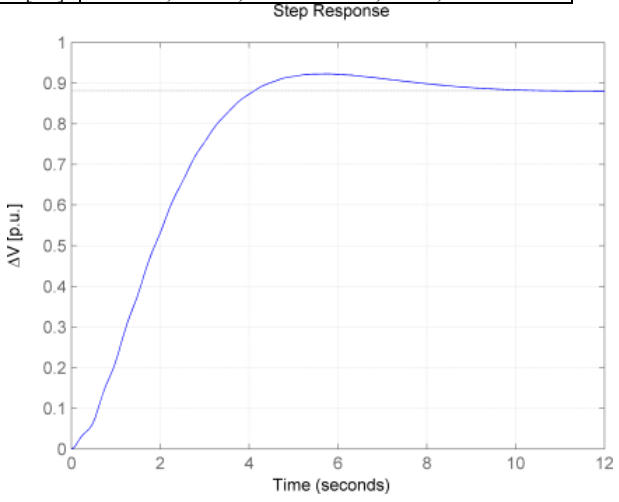

Figure 5-15: unit step response in X/R=1.37 scenario.

The analyses of both confirm that there are neither poles nor zeros lying on the imaginary axe. Moreover the static gain value matches with the symbolic expression in (5.62). Previous conclusions are further confirmed by the step response of (5.46) represented in Figure 5-15.

- The matching between EMT simulation and small signal model appears outstanding, confirming K-parameter model validity under different reactance to resistance ratios;
- In order to obtain same reactive power dispatch in all scenarios the terminal voltage E_t is higher as much as the equivalent line is resistive;
- Active power profile is not affected by terminal voltage perturbations, confirming the validity of formulated *A method*:

$$\Delta\varphi_t = -\frac{\partial P}{\partial E_t}\frac{\partial \varphi_t}{\partial P}\Delta E_t \tag{5.63}$$

$$\Delta Q = \frac{\partial Q}{\partial E_t}\Delta E_t + \frac{\partial Q}{\partial \varphi_t}\Delta\varphi_t \tag{5.64}$$

The small signal models developed for the reactive power regulator are validated assuming same PI parameters ($k_p = 0.05669$; $k_i = 0.06136$) and system conditions. Relevant results, useful for comparing small signal model and PSCAD® electrical response, are shown in Figure 5-16.

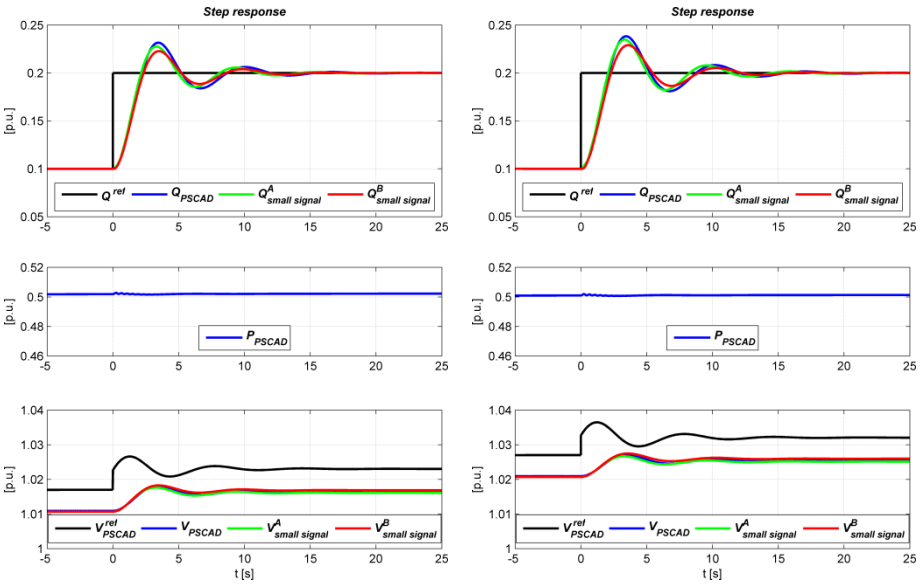

Figure 5-16: ΔQ=0.1 p.u. step response, starting from P=0.5 p.u. and Q=0.1 p.u in the scenarios X/R=5, on the left, and X/R=1.37, on the right (© 2016 IEEE).

In these cases can be observed:

- proposed external PI regulator guarantees a zero steady state error control of the reactive power, in both reactance to resistance ratio scenarios, confirming the efficacy of proposed regulator;

- The matching between reactive power responses is good, but *A* method appears leading to a closer response to PSCAD® result, rather than what with *B* one permits. This is further confirmed in the frequency domain observing the Bode plots of Figure 5-17. All represented transfer functions are referred to pre-event steady state operating conditions in case of X/R=1.37. In particular the black line represents the estimated closed loop transfer function, obtained applying Matlab Identification Toolbox [16] to the data extracted from a separate PSCAD® run. In order to scan system response for a wide range of frequencies a white noise was added to the pre-event input Q^{ref} and the corresponding output Q_m is sensed. All the transfer functions show same bandwidth but *A* and *B* methods differ at higher frequencies, in particular they show a couple of "resonance peaks" not presented by the identified transfer function. Such discrepancies are deemed to be due to the steady state simplifications assumed with (5.4) and (5.27) respectively for *A* and *B* method. The latter moreover is certainly affected by the extensive use of linearized equations;

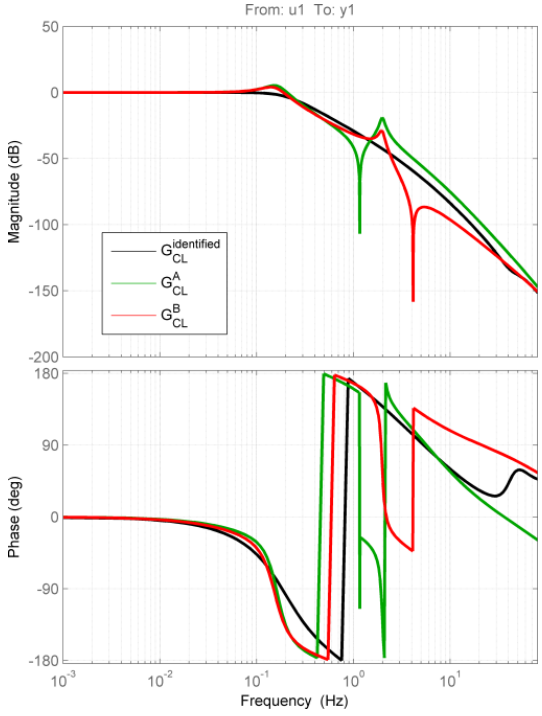

Figure 5-17: comparison of analytical and identified reactive power closed loop transfer functions.

- as previously remarked active power profile is not affected by reactive power perturbations, confirming the validity of the assumptions made with *A* method.

5.6 NELDER AND MEAD SIMPLEX OPTIMIZATION

For power system engineers the lack of plant know-ledge and tools represent the most challenging hurdle for the analytical approach to the regulator tuning. Empirical tuning methods, as Ziegler-Nichols technique, in these cases could turn out useful. Otherwise multiple run simulation can be used even if they are rather time consuming. That is the case of blind multi-run simulations covering all predefined combinations set in advance by the designer, or even Monte Carlo based methods, where domain combinations are picked up on the base of probabilistic distribution. Another approach is represented by iterative runs based optimizations, where the searching criterion pursues the minimization of an objective function computed by running. PSCAD® which is a powerful tool offering four optimization methods [105].

In this paragraph the reactive power regulator is tuned by making use of Nelder-Mead Simplex method.

A mathematical insight to Nelder-Mead Simplex algorithm is given in [106, 107]. This optimization method fits to nonlinear problems and it has not to be confused with Simplex method [108], belonging to the linear optimization methods family, even if they perform similar procedure. Such technique has been already applied by PSCAD® developers in [109, 110] for solving power system optimization problems by means of iterative EMT simulations in case of low variables number. No need of computing derivatives represents the main advantage of this method, while the likehood of trapping the solution trajectory in a local optimum should be mentioned as the most important drawback.

It must be remarked that PSCAD® offers the optimization engine embedded in the "Optimum Run" block, while the definition of the objective function is let to the user. The same block doesn't allow setting any constraint on the parameters, therefore the user is highly recommended to:

- Connect a ceiling limiter block at the output of the "Optimum Run" block;
- Evaluate whether parameters trajectories described by iteration remained inside the domain during the optimization, since former trick cannot be effective for some classes of problems.

It is also very important highlighting that no postprocessment of simulation results is allowed since "Optimun Run" block automatically computes the optimization on the base of the available objective function at the end of each run.

With reference to the geometrical approach adopted for proceeding with the optimization, it should be mentioned that the so-called simplex polygon turns out a triangle. In fact the number of vertices is always given by $n_v + 1$, where $n_v = 2$ in this case, since the variables are k_p and k_i.

In spite of considering traditional Performance Indexes, like Integral Square Error (ISE), Integral of Absolute value of Error (IAE) and time weighted IAE (ITAE), for defining the objective function, as done in [109-111], two alternative methods are here proposed. Both of them rely on the step response characteristics, and don't make direct use of the output signal $y(t)$ into the objective function as it was instead necessary with aforementioned Performance Indexes. Considered step response characteristics, referred as Characteristic Indexes (CI) among control engineers [112], are:

- t_r is the rise time, that is the time required for the response to rise from 10% to 90% to its final value;
- s is the overshoot;
- t_s is the settling time, that is the time elapsed from the application of a step input to instant when the output enters and remains within a predefined band.

In order to make these CIs available at the end of each run, the detectors shown in Figure 5-18 were conceived. It must be noted that a meaningful settling time value can be detected only in case the simulation time is long enough for letting the signal to come inside the predefined band. This implies that the system is stable with a response featured by sufficiently damped oscillations around the final value. For this reason the designer has to define an initial guess of optimization variables that ensure to track the proper settling time. Moreover the initial step has to be set reasonably small. Such ruse allows avoiding unstable cases and properly addressing the simulation, since solutions featured by longer settling times will be automatically disregarded due to the fact that they determine higher objective function values.

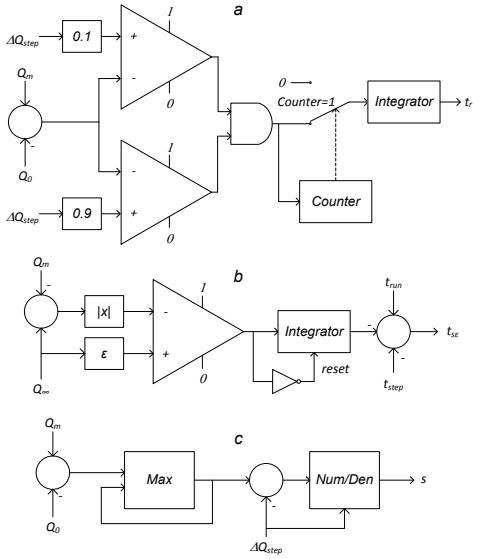

Figure 5-18: runtime detectors for rise time (a), settling time (b) and overshoot (c) (© 2016 IEEE).

Following alternative objective functions are formulated:

$$OF_1(k_p,k_i) = k_1 \frac{\left|t_r^{ref} - t_r\right|}{t_r^{ref}} + k_2 \frac{\left|s^{ref} - s\right|}{s^{ref}} + k_3 \frac{\left|t_s^{ref} - t_s\right|}{t_s^{ref}} \tag{5.65}$$

$$OF_2(k_p,k_i) = k_1 \frac{t_r}{t_r^{ref}} + k_2 \frac{s}{s^{ref}} + k_3 \frac{t_s - t_r}{t_s^{ref} - t_r^{ref}} \tag{5.66}$$

Objective function OF_1 defines the weighted sum of the relative errors of the parameters. On the other hand OF_2 represents the weighted sum of the relative values but taking into account that the rise time requirement is usually counteracting to the overshoot and to the difference between settling and rise time, in a nutshell the time necessary for damping the ringing.

The results obtained in Figure 5-19 and Figure 5-20 are obtained considering:

- The X/R=1.37 scenario, analysed in paragraph 5.5;
- The optimisation targets of Table 5-2;

Table 5-2: optimisation references

CI	Target value
t_r^{ref}	2 s
s^{ref}	10%
t_s^{ref}	10 s

- The optimisation settings of Table 5-3, where Δ refers to the tolerance threshold enabling the successful termination of the optimisation;

Table 5-3: weighting factor and optimisation tolerance values

Objective function	k_1	k_2	k_3	Δ
$OF_1(k_p,k_i)$	1	4	1	0.01
$OF_2(k_p,k_i)$	1	1	1	0.005

- Same initial value of PI parameters;
- Same reactive power step change.

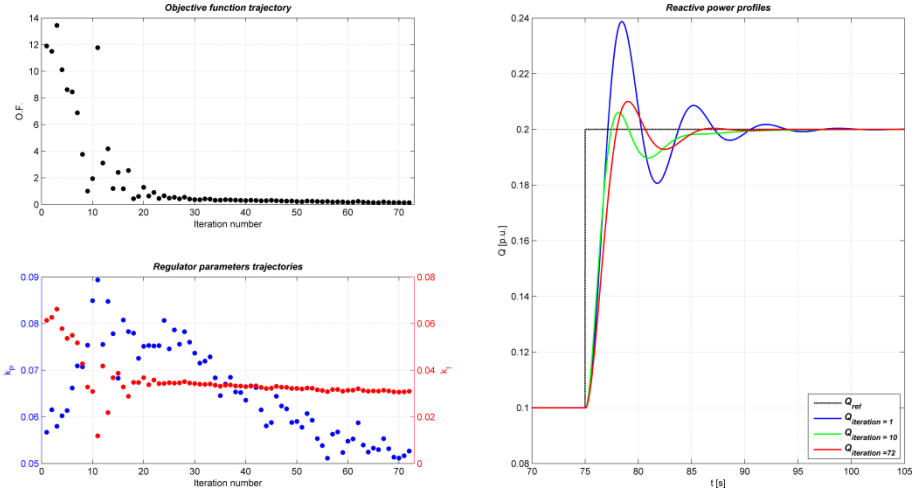

Figure 5-19: summary results referred to OF_1 (© 2016 IEEE).

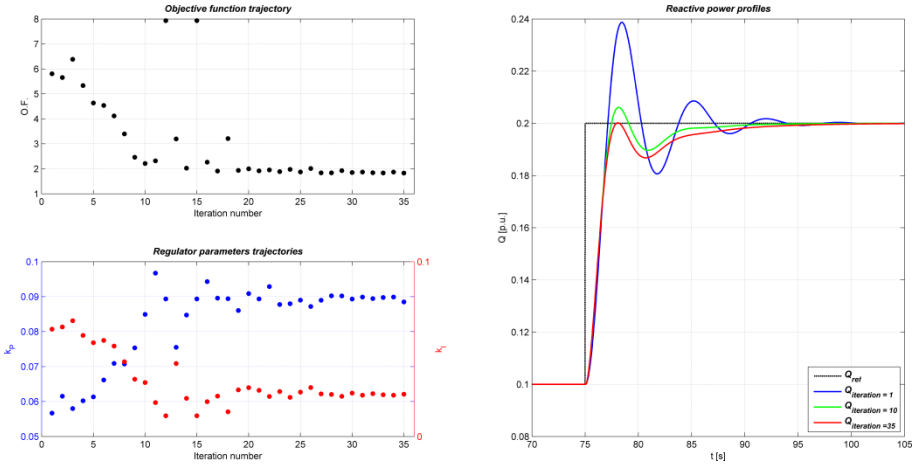

Figure 5-20: summary results referred to OF_2 (© 2016 IEEE).

The iteration based optimization led evidently to decrease the objective function in both cases. Due to different objective functions the optimal step responses are different, but both look evidently improved respect to the first iteration. With reference to formulated objective functions it is worth to be noted that while OF_1 aims minimizing the relative errors, which leads to null the objective function whenever attained the reference values, OF_2 instead minimizes an objective function where reference terms are used only for normalization. This has a huge impact in case like in Figure 5-20 where the final value of the objective function turns out lower than $\sum_{i=1}^{3} k_i = 3$. For this reason the final value of the overshoot fell to almost zero, since the optimization found room for decreasing the objective function acting on the term $\frac{s}{s^{ref}}$. In order to avoid such effect the weight of the overshoot term, k_2, should be decreased.

Both methods however appear appropriate for a multiple run based optimization. In order to highlight the cons of non-linear Simplex method of Nelder-Mead is proposed Figure 5-21, referred to an optimization identical to the one referred to Figure 5-19 apart for the parameter affected by the optimization and weighting factor k_2 value (here considered 4). In this case in fact, beyond k_p, the simplex acts on $\frac{1}{k_i}$ instead of k_i. Due to $\frac{1}{k_i} \approx 16.6$ the optimization stops since small variations of $\Delta\frac{1}{k_i}$ don't significantly affect the value of the objective function at the last iterations (in other words the improvement of the objective function value is less than the predefined tolerance Δ). Slightly improved results could be obtained reducing the tolerance, at the cost of a higher optimization burden. Latter optimization therefore confirms the drawback represented by the possibility of finding only local optima with this method. Moreover it underlines the importance of a wise parameters choice, like performed in Figure 5-19 and Figure 5-20 where $k_p \approx k_i$.

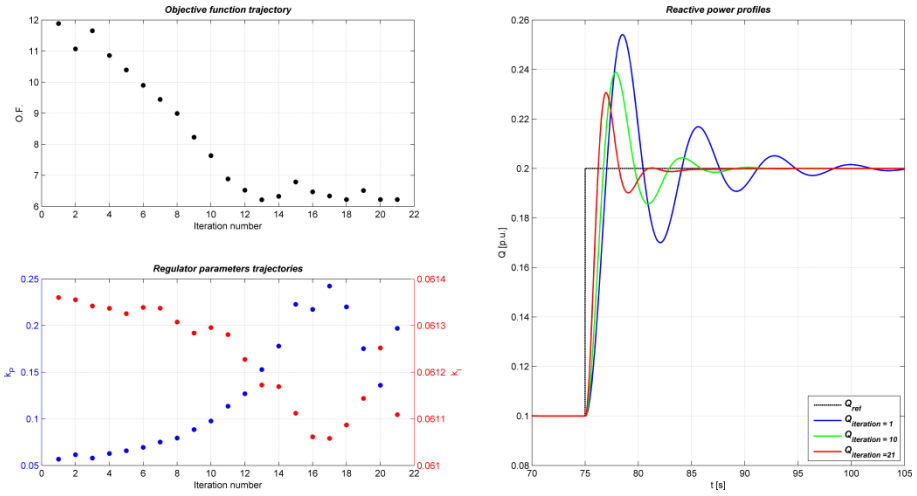

Figure 5-21: results referred to the objective function(5.65), formulated as $OF(k_p, \frac{1}{k_i})$.

5.7 POLE ASSIGNMENT METHOD

Once known the plant transfer function and regulator type, and given the speed step response characteristics, regulator parameters can be set easily making use of the root locus if the closed loop transfer function looks or can be reduced, through identification of dominant poles, to:

$$G_{CL}(s) = \frac{\omega_n^2}{s^2 + 2\zeta\omega_n s + \omega_n^2} \tag{5.67}$$

Under this assumption as discussed in A.2 a relation between the location of the complex conjugate dominant poles and the step response characteristics exists, in particular as shown in Figure 5-22 can be identified:

- Damping ratio ζ, linked to the overshoot by (A.10);
- Natural pulsation ω_n;
- Settling time $t_{s\varepsilon} = -\frac{ln 0.01\varepsilon}{\zeta\omega_n}$;

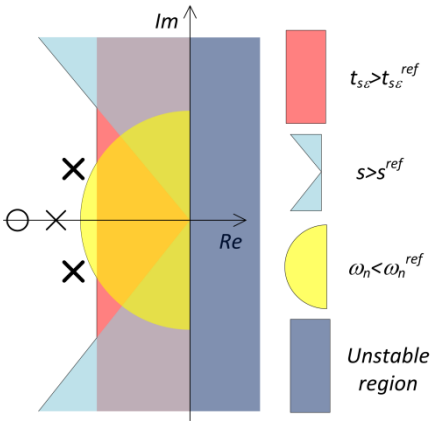

Figure 5-22: relation between CIs and zero pole map in presence of dominant complex conjugate poles.

The root locus in this sense eases the offline step response assessment since it represents the trajectory described by closed loop system poles varying the static gain of the transfer function.

Moreover since the PI parameter design is a two degree of freedom problem, the zero associated with the PI regulator is frequently chosen in order to cancel the dominant pole of the plant, as proposed by Modulus Optimum criterion presented in A.2. In this way the pole assignment method is eased and an iterative procedure could still be necessary only in case the specifications for the transient response aren't met at first trial. Moreover in case of second order plants, the pole cancellation always ensures the fulfilment of aforementioned hypothesis on the closed loop transfer function.

The plant transfer function $G_{plant} = \frac{\Delta Q_m}{\Delta V_{ref}}$, found analytically through the first method described in appendix A.4, instead has eighth order even if most of the poles are negligible. On the other hand there are two dominant complex conjugate zeros and two complex conjugate poles, as listed in Table 5-4 and graphically shown in the enlargement of the zero pole map of Figure 5-23. It is worth to be remarked that the presence of dominant complex conjugate pair of poles impedes any cancellation with PI regulator zero. For the case in analyses the satisfaction of transient specifications is not ensured by the root locus, even if the poles are properly placed [113].

Table 5-4: closed loop transfer function characteristics.

Static gain	16.610
Zeros [Hz]	-50; -1; -0.0006±25.9838i
Poles [Hz]	-650.92; -50.05 ; -25; -1.75; -0.63 ± 12.41i; -0.52 ± 0.48i

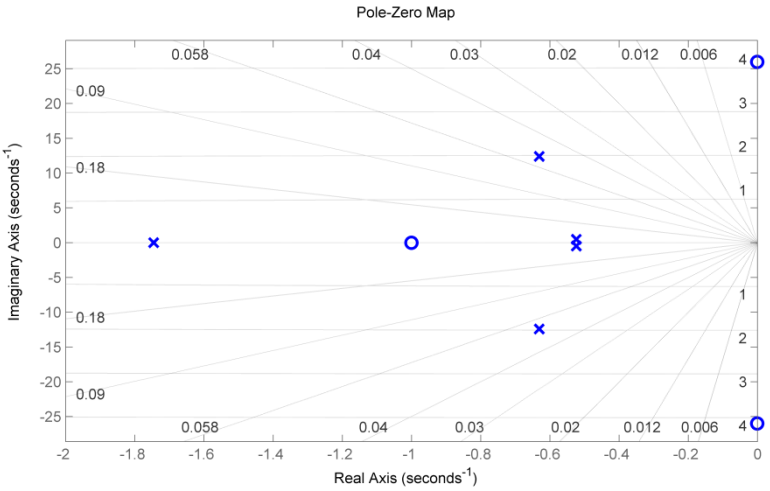

Figure 5-23: poles and zeros map of the plant (enlargement).

Therefore PI parameters are selected making use of Sisotool [15] with a trial and error method. Obtained results are shown in Figure 5-24.

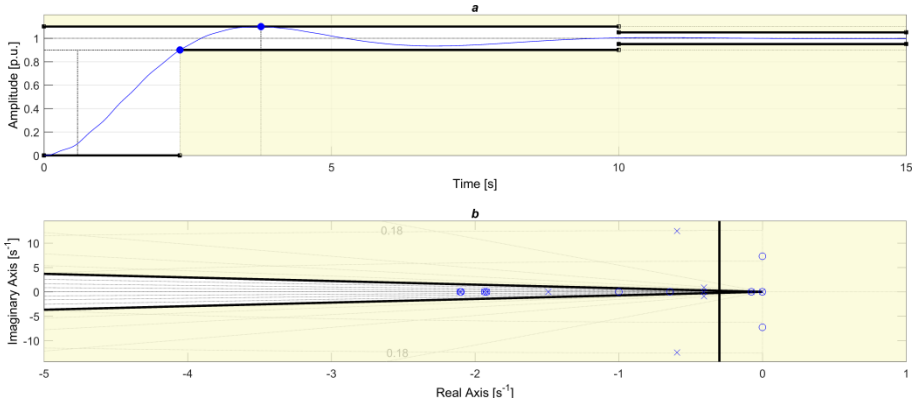

Figure 5-24: closed loop step response (a) and enlargement of pole-zero map with geometrical limits considering a second order closed loop transfer function (b) (© 2016 IEEE).

Described procedure allowed selecting proper PI parameters. Moreover the zero-pole map of the closed loop transfer function, proposed in Figure 5-24, highlights that a couple of complex conjugate poles lays in the region out of predefined transient response characteristics if the closed loop transfer function would present a couple of complex conjugate dominant poles. This confirms that pole placement based on the root locus would have been misleading with this plant transfer function. Alternative the user could have designed the regulator by means of autotuning tools such as [114].

5.8 CONCLUSIONS

In this chapter two classes of tuning methods of a simple linear reactive power regulator are proposed. Both methods turned out effective and suitable for obtaining the required step response characteristic.

In the first paragraph an insight is given about the effect of different equivalent grid impedance angle, through a parametric study of the power flow Jacobian matrix elements. Then the validity of traditional K-parameter model in different reactance to resistance ratio of the equivalent interconnecting line has been proven. The study highlighted that an AC5A exciter shows up a steady state error in the voltage regulation. Cascading previous regulator with an external reactive power loop allowed performing a zero steady state reactive power regulation. The regulator tuning resulted feasible either through time based enabled Nelder and Mead optimization and with modern tools for pole assignment method, once calculated the plant transfer function. For this reason in the chapter are proposed two small signal approaches, suitable for any grid impedance value. So called *A method*, based on the decoupling of active power control from voltage control, provides results closer to PSCAD® simulation results. On the other hand proposed *B method*, developed extending K-parameter model, offers the advantage of an in deep insight in machine magnitudes. With reference to time enabled optimization methods this chapter proposes two new objective functions relying on step response characteristics. Such methods offer the advantage of not being based on all the time series data respect to traditional Performance Indexes methods. A comparison of reactive power profiles to a step reference change obtained with the two sets of PI parameters under same step response characteristics in PSCAD® environment is given in Figure 5-25.

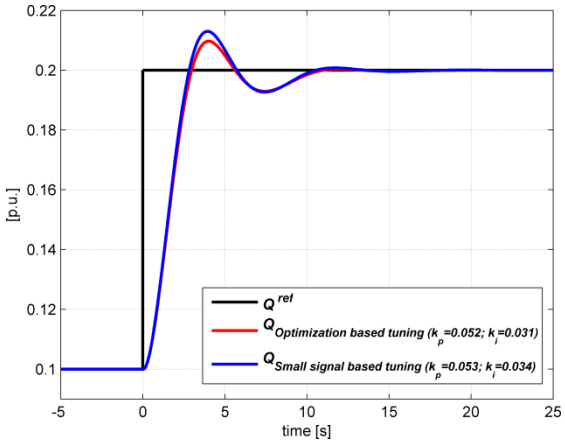

Figure 5-25: Step response comparison of same system considering different sets of reactive power regulator parameters (© 2016 IEEE).

In Figure 5-25 the small signal model based tuning appears leading to a slight deviation respect to time enabled optimization tuning, which fully satisfy characteristic indices targets. On the other hand it is worth to be reminded that the analytical definition of the small signal model could be very time consuming and sometimes difficult to obtained without advanced tools in case of complex plants. Optimization enabled simulations are certainly resource demanding but the relative simplicity in the formulation of the objective function saves tuning times. Moreover literature demonstrated the validity of latter method even in case of non linear plants. Nevertheless the designer is invited to pay attention to the optimization results, since as shown in this chapter inappropriate objective functions or unwise parameter handling or non convex problems could lead to suboptimal solutions.

CHAPTER 6

A REDUCTION METHOD FOR RADIAL ACTIVE DISTRIBUTION NETWORKS

With this last chapter the focus of thesis shifts from the control of the DGs to the overall response of a distribution network where they are connected. The core idea here proposed blossomed during a meeting held the industrial project partners and it aims tackling a real issue faced by network operators. Indeed year by year the presence of distributed generators has been increasing, making difficult to represent properly distribution networks for system security assessments.

The problem description is given initially, the description of the core idea follows. Taking into account a portion of a real Danish Distribution Network the proposed idea is validated, through comparison of the results obtained in PSCAD® with the detailed network model and with the reduced one. The chapter includes the description of the DGs model used for the detailed simulation and some methodological notes regarding the implementation of reduction method in PSCAD®.

The contents of this chapter are presented in [115].

6.1 PROBLEM DESCRIPTION

So far the Transmission System Operators (TSOs) have been modelling Distribution Networks (DNs) with a simplified MV busbar for online stability studies [27]. In order to take into account also the internal generators, beyond the load represented with an aggregated load, one or more equivalent synchronous generators, depending by the rating of the units, and an equivalent wind turbine have been connected to the busbar. This makes a rough dynamic model of the DN most of all because it is usually kept constant, regardless from real operating condition of the units. Such representation however is acceptable whenever the share of Distributed Energy Resource (DER) is low. In fact the low short circuit power at the Point of Common Coupling (PCC) of a DN and the poor Distributed Generators (DGs) inertia support don't

justify costly and time consuming model enhancements. Nevertheless DER diffusion and their related possibility to offer ancillary services are changing the scenarios as in a renewable committed country like Denmark. Therefore the need of adaptable DN models taking into account unit controls and online measurements turns out.

On the other hand the reduction methods described in paragraph 2.2, don't appear suitable for reducing external subsystems populated by a mix of loads and VSC interfaced sources. Loads indeed could have a voltage dependent behaviour, therefore lumping them in an equivalent should take into account the voltage drops occurring in a real DN. DGs on the other hand shows up different responses during normal and faulted conditions, since they must be compliant with the grid codes. Therefore it is not possible to determine a single linearized DG model, most of all lumped at the aggregation node, fitting to both conditions. On the other hand detailed representation of the DN for system stability studies would be too resource demanding.

6.2 THE CONCEPT

Simulations tackling system stability are traditionally performed by TSOs at the fundamental, sometimes considering only the symmetrical component. Such phasorial otherwise called RMS simulations are featured by a relative large time step, millisecond order, therefore they don't allow taking into account electrical transients, but permit to model the control and dynamics of large loads, tap changer, plant controllers of large renewable based plants and exciter and governors of synchronous generators. It is then straightforward that the current regulator dynamics own of grid connected VSC, which have a bandwidth of some hundreds of Hertz, depending by the switching frequency as shown in Chapter 3, can be hardly represented only in case of further VSC delays (i.e. gate block status following severe voltage perturbations). Under this assumption if the external susbsystem contains only VSC interfaced renewable based DGs and loads without significant dynamics, then the same part of the network is state less and it can be represented by an equivalent voltage dependent PQ node located at the boundary node. This is schematically shown in Figure 6-1.

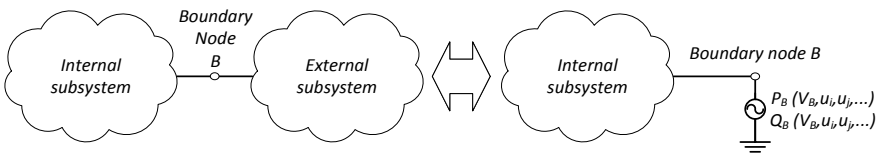

Figure 6-1: reduction of the external radial susbsystem in an equivalent dynamic PQ node.

It must be noted that renewable based DGs have zero marginal costs therefore, most of all in case of medium and small rated units, they are always operated in Maximum Power Point Tracking mode. The grid code regulation compliance moreover ensures that those units provide dynamic reactive current support or simply disconnect. It follows that DGs power output is univocal, given the terminal voltage and "natural input", as wind speed or irradiance measurements. Similarly also the load, through local measurements and the estimation of its characteristic, can be unambiguously defined. Such features allow defining an equivalent PQ node that it is dependant not only by the local voltage but to further specific inputs, hereinafter referred as external factors.

In order to properly program this equivalent node, the here defined mapping process has to be carried out offline through multiple power flows. The internal subsystem indeed has to be replaced at the boundary node by an ideal generator representing the slack node in power flows, as shown schematically in Figure 6-2. VSC interfaced renewable DGs can then be modelled as voltage and weather dependent PQ nodes. Once the defined the model of the external subsystem, for each element of the sets of external inputs the voltage at the slack node is varied and the corresponding power flow, in terms of active and reactive powers, is tracked.

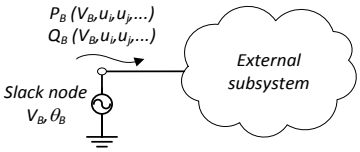

Figure 6-2: mapping procedure.

The resulting multidimensional arrays defining active and reactive powers at the equivalent node turns out smooth meshes allowing interpolating the data series.

On the base of this observation the here determined multidimensional arrays can be interpolated online, given instantaneous inputs. Through this process two simple look-up tables defining respectively active and reactive power at the boundary node as a function of its voltage can be defined. Just this method allows easily defining the voltage dependent PQ node for dynamic studies.

Proposed method on the other hand suffers following weaknesses:

- It doesn't take into account the LVRT disconnection times of DGs, which would make the model time dependent;
- It is fully deterministic, therefore it represents a non viable solution in case of complex DNs with tens of external factors;

- It doesn't fit to DNs populated by synchronous generators, f.e. CHPs, or large induction motor loads.

6.3 CASE STUDY

The proposed aggregation method is tested taking into consideration the simplified model of radial Støvring distribution network, managed by HEF, project partner of the project, and already adopted for research purposes in [116]. It was here redesigned in PSCAD® and resulting SLD is shown in Figure 6-3.

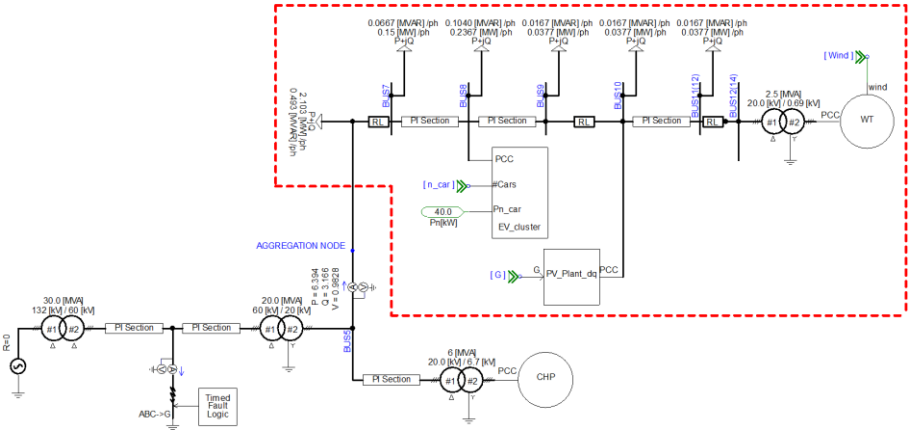

Figure 6-3: PSCAD® SLD of simplified Støvring network. The DN to be reduced is red outlined (© 2013 IEEE).

The overall power system includes a 132 kV source, 60 kV and 20 kV lines, beyond the interfacing transformers. A 5 MW gas fired turbine, represented with a GAST model [38], coupled to a synchronous generator adopting brushless AC5A exciter, is connected at 20 kV level through its dedicated transformer. The external susbsystem, outlined with a red dashed line in Figure 6-3, includes both loads and VSC interfaced DGs.

Considering a fault occurring in the internal subsystem at 60 kV level, the response of the overall detailed model and the one considering the equivalent are given in this paragraph. A detailed description of the main elements populating the external subsystem loads is given as well.

6.3.1 LOAD MODELS

All the loads included in the external subsystem are represented by so called exponential model [27], therefore they are voltage dependent.

$$P = \begin{cases} P_0 \left(\frac{V}{V_0} \right)^{k_V^P} & if \ V \geq 0.8 pu \\ P\big|_{V=0.8pu} \left(\frac{V}{0.8V_0} \right)^2 & if \ V < 0.8 pu \end{cases}$$
$$Q = \begin{cases} Q_0 \left(\frac{V}{V_0} \right)^{k_V^Q} & if \ V \geq 0.8 pu \\ Q\big|_{V=0.8pu} \left(\frac{V}{0.8V_0} \right)^2 & if \ V < 0.8 pu \end{cases} \quad (6.1)$$

Where:

- $_0$ refers to nominal conditions;
- k_V^P, k_V^Q can range from 0 to 2 load by load [27];
- $P\big|_{V=0.8pu}, Q\big|_{V=0.8pu}$ represents respectively active and reactive power values when the voltage is 0.8 p.u.

It is worth to be noted that this treatise does not take into account the dependency by the frequency. Moreover with reference to Equation (6.1) should be highlighted that whenever the voltage drops below 0.8 p.u. the load model switches automatically to constant impedance for convergence reason.

In the DN however a charging station for EV is considered. Since these loads are power electronically interfaced they are modelled as constant 40 kW power load per vehicle. Moreover it is here assumed that they are voltage sensitive, therefore they automatically disconnect in case the voltage drops below 0.75 p.u..

6.3.2 WIND TURBINE

The 1.5 MW type 4 WT described in [117] is assumed to be connected the end of the 20 kV feeder, through its own step-up transformer. The unit is schematically represented in Figure 6-4.

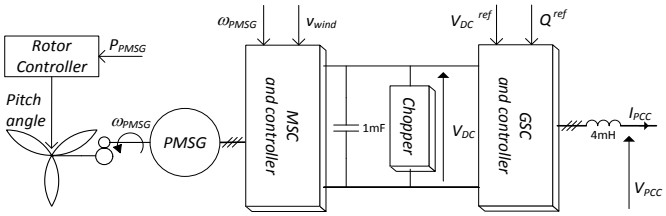

Figure 6-4: type 4, pitch controlled, wind turbine scheme (© 2013 IEEE).

The WT shaft is coupled to the Permanent Magnet Synchronous Generator (PMSG) through a gearbox. A turbine rotor controller is in charge for curtailing the output power whenever it exceeds the rated power by means of the blade pitch angle regulation. The Back-to-Back (B2B) converter is modelled through power lossless average converters, each one controlled operating on the rotating reference frame aligned to its AC side voltage. The damping shunt capacitor on the DC link is taken into account mathematically in the equation keeping the power balance through the DC link. The Machine Side Converter (MSC) controller regulates the turbine speed maintaining it at the optimal value, given instantaneous wind speed and PMSG rotational speed. The Grid Side Converter (GSC) in normal operation is in charge for controlling the reactive power exchanged with the grid and the DC link voltage, indirectly regulating in this way the active power flow through the B2B converter. Nevertheless just the GSC control scheme has been modified as shown in Figure 6-5 for providing Dynamic Reactive Current Support (DRCS) during faults as prescribed by Danish grid code for unit larger than 1.5 MW [118]. The disconnection time requirement in LVRT is here disregarded. Particular care has been taken in order not to overload the GSC in terms of current during fault ride through. In this work it was assumed possible overloading the WT converter up to 120% respect to the rated power. Considering a rotating reference frame aligned to the voltages sensed after the GSC filter, the scheme constrains the d-current during faults prioritizing the q-current component, as stated in inequality:

$$i_d^{ref\,\prime} \le \sqrt{\left(1.2I_n\right)^2 - \left(i_q^{ref}\right)^2} \tag{6.2}$$

Whenever the d-current component reference reaches the allowed ceiling, the GSC cannot handle anymore the DC-link voltage control. In this case an ideal chopper is supposed to be triggered, absorbing the exceeding power and maintaining constant the DC-link voltage.

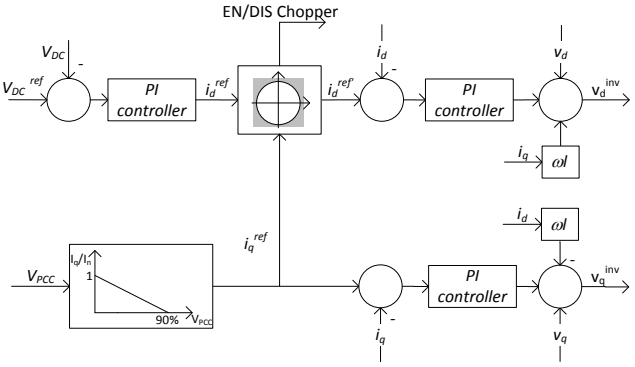

Figure 6-5: Grid Side Converter control scheme (© 2013 IEEE).

For the sake of proof in Figure 6-6 the WT response to a variable wind speed is given.

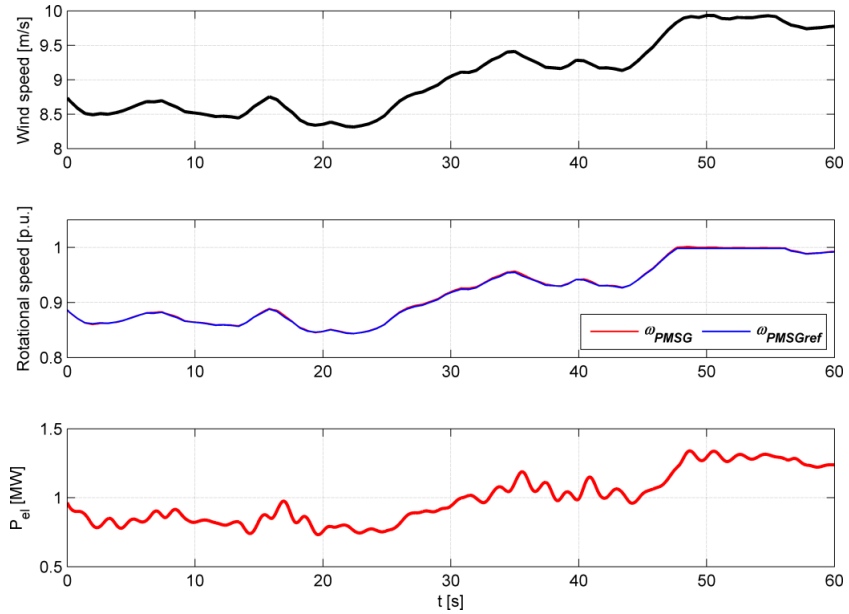

Figure 6-6: rotational speed control.

6.3.3 PHOTOVOLTAIC PLANT

A 250 kW PVP is connected at a node along the 20 kV distribution line. The detailed unit description is provided in [119] while in Figure 6-7 is reported the basic layout. It must be underlined that the unit design has not been modified respect to [119]. Thanks to an extremely high array open circuit voltage (1700 V) and the VSC

output voltage of only 230 V, the MPPT algorithm is performed, exploiting the incremental conductance method, through a buck converter. With respect to [119] the Voltage Source Converter (VSC) control is here improved making use of de-coupled d-q control with inner current loops. In particular similarly to the WT scheme the VSC controller regulates the DC link voltage and the reactive power at the PCC. Contrary to the WT case, the PVP is here assumed not providing DRCS but it is allowed suddenly disconnecting whenever the grid voltage drops below 0.75 p.u..

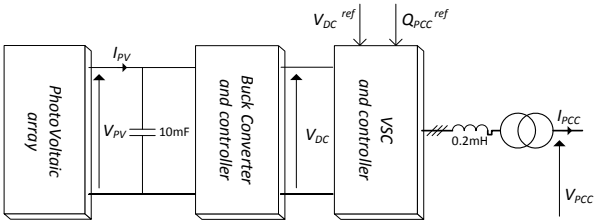

Figure 6-7: PhotoVoltaic unit control scheme (© 2013 IEEE).

6.3.4 METHODOLOGICAL NOTES AND MAPPING RESULTS

Proposed mapping process demands running several power flows, a function currently not available in PSCAD®. A workaround procedure is as follows:

- Both regarded DGs operate in MPPT mode unless when giving priority to the reactive current for DRCS. Therefore the correspondence between the external factor and the maximum corresponding power is known, assuming steady state operation. In the case of the WT the well known wind cubic dependent expression was used, neglecting shaft dynamics. In the case of the PVP instead the power vs irradiance characteristic was found imposing a slowly increasing irradiance to previously described dynamic model. As shown in Figure 6-8 the relation is almost linear and the current dependent losses in power electronics devices are negligible as expected. This is highlighted by the slightly increasing difference between the power delivered by the array and the power fed into at the PCC whenever the irradiance increases as well.

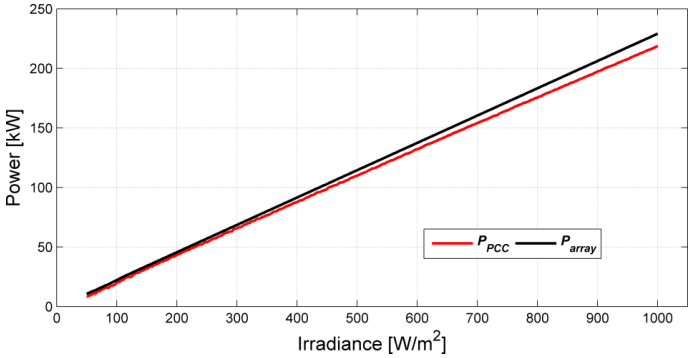

Figure 6-8: photovoltaic plant characteristic (© 2013 IEEE).

Known the DRCS law then the reactive power and consequently the active power during faulted conditions, given VSC capability, were calculated. Through this step both units were represented by externally controlled three-phase impedances, that can assume negative parameters in PSCAD®;

- The mapping process followed slowly varying the voltage at the mains (HV side of the network) for all predefined combinations of the external factors listed in Table 6-1, using *multiple run* function. The elements of such external factor arrays are selected in order to cover with good granularity their possible ranges and taking into account the dependency between the external factor and corresponding output power. For the sake of the reader this is shortly described with reference to the WT. Given the cubic relation between the wind speed and WT output power, the array has a finer granularity at medium and high winds up to the WT nominal wind speed (10.5 m/s). Moreover the array values choice takes into consideration the cut-off wind speed (12.5 m/s).

Table 6-1. external factors regarded for the mapping process

External factor	Set of values
EVs in charging mode	$\{0,1,2,3,4\}$
Wind speed [m/s]	$\{0,3.5,5,7,9,10,10.5,12.5,12.6,14\}$
Irradiance [W/m^2]	$\{0,350,700,1000\}$

A user designed MATLAB® script automatically imports simulation log out files and it handles them for defining two multidimensional meshes, representing the output active and reactive powers flowing at the aggregation node as a function of the voltage and the set of parameters. In order to define a uniform grid from the scattered data imported from the simulation, *TriScatteredInterp* MATLAB® function was used. Through this procedure the impact of each external factor can be easily assessed. In Figure 6-9 a and b the active power flows drawn by the DN at the boundary node respectively in case of null and very high irradiance (1000 W/m^2) are

plotted. In particular the circles define the scattered data obtained through the mapping process, while the mesh is computed through interpolation. It is straightforward observing that the power at the boundary node decreases as the wind increases, since load notation is considered. Looking from the voltage perspective the overall network behaviour looks similar to the load one, since loads remains dominant respect to the DER in Støvring network. Nevertheless some interesting details are worth to be mentioned. As shown in Figure 6-9c the effect of wind stronger than the cut-off wind speed is evident on the power flow at the retained node. Moreover the assumption of PVP plant disconnection in case of terminal voltage dropping below 0.75 p.u. is made evident by a gradient variation of the mesh in Figure 6-9b and proposed in the enlargement of Figure 6-9d. It is worth to be noted that such slope variation is as much more evident as the irradiance is higher, while it doesn't show up in the scenario of null irradiance of Figure 6-9a.

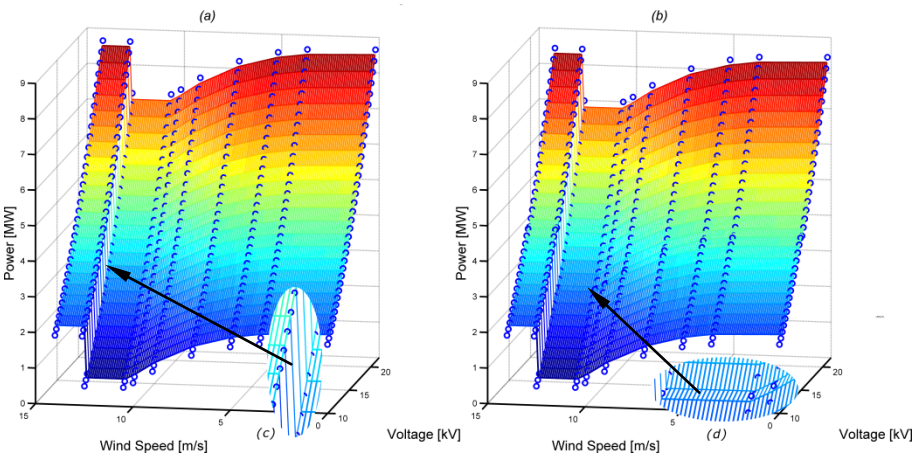

Figure 6-9: active power meshes as function of voltage at the aggregation node and wind speed, considering no EVs in charging mode and constant impedance loads. No and high irradiance scenarios, respectively G=0 W/m2 and G=1000 W/m2 (a and b). Enlargements of mesh slope variations due to WT disconnection in case of wind stronger than cut-off speed (c) and PV plant disconnection for LVRT (d).

Through a second defined script, exploiting *Interpn* MATLAB® function, given the instantaneous external factors the imported data are efficiently interpolated in order to define the final two look-up tables, graphically represented in Figure 6-10.

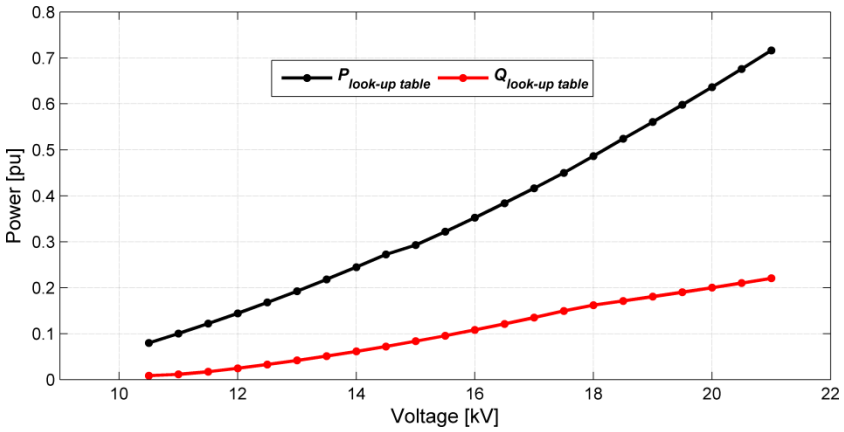

Figure 6-10: characteristics of the aggregated distribution network assuming base power 10 MVA (© 2013 IEEE).

Such methodology allows defining the equivalent in the grey box of Figure 6-11.

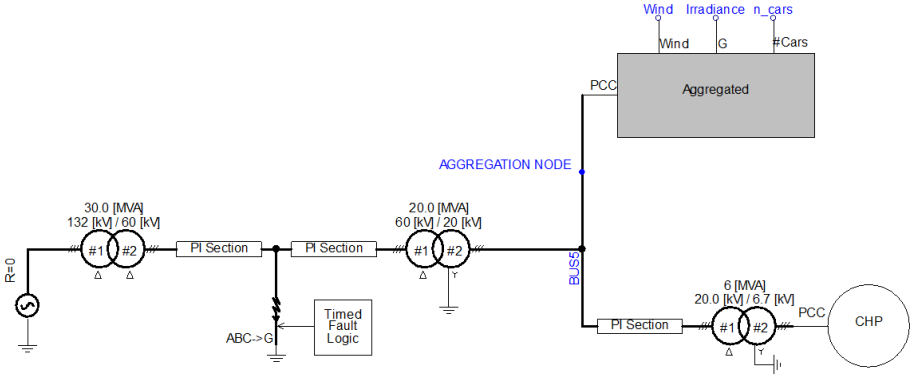

Figure 6-11: PSCAD® representation of the power system with the aggregated distribution network (© 2013 IEEE).

6.3.5 RESULTS

Considering following scenario:

- One car in charging mode;
- 10.4 m/s wind speed;
- 400 W/m^2 irradiance;
- Constant impedance loads ($k_V^P = 2$ and $k_V^Q = 2$);
- Symmetrical fault occurring in the retained 60 kV line, with impedance 10 Ω, occurring at 1 s and self cleared at 1.5 s.

The comparison between detailed and reduced network model responses is presented in Figure 6-12. Outstanding is the matching in voltage and power profiles both in

steady state and transient conditions. For a deeper analysis the enlargements of all profiles during fault transient are given in the right side of Figure 6-12. The good matching is confirmed even if the reduced network response is slightly affected by an oscillation due to the interpolation of implemented look-up tables.

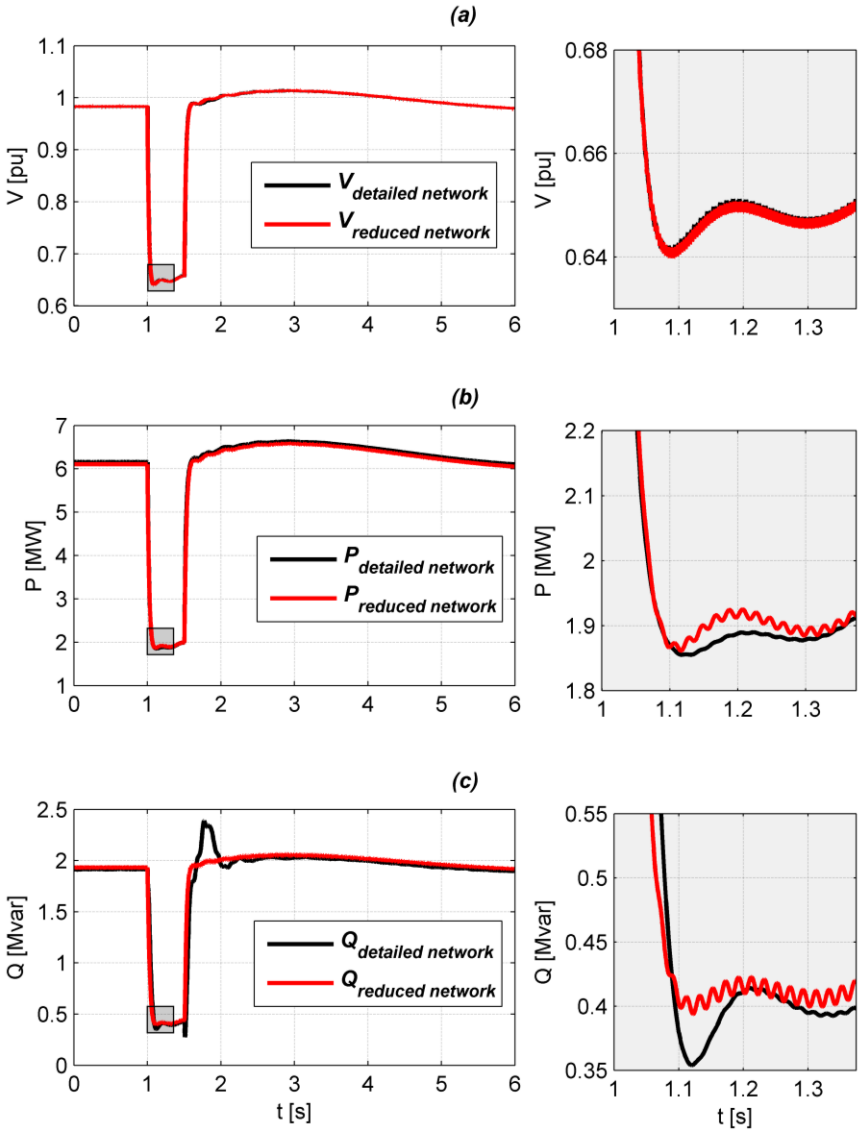

Figure 6-12: comparison in the same scenario. Voltage (a), active and reactive power (b and c) at the retained node. The enlargements of fault transients, highlighted with grey boxes are proposed on the right for a detailed comparison (© 2013 IEEE).

Instead the oscillation in the reactive power profile of the detailed network occurring after the fault clearing is due to PVP control. Indeed an overshoot in DC-link voltage and power profiles in the PVP appears when the unit reconnects after the fault, as shown in Figure 6-13. However the overall control of the PV unit turns out stable and it doesn't influence the reduction method proof.

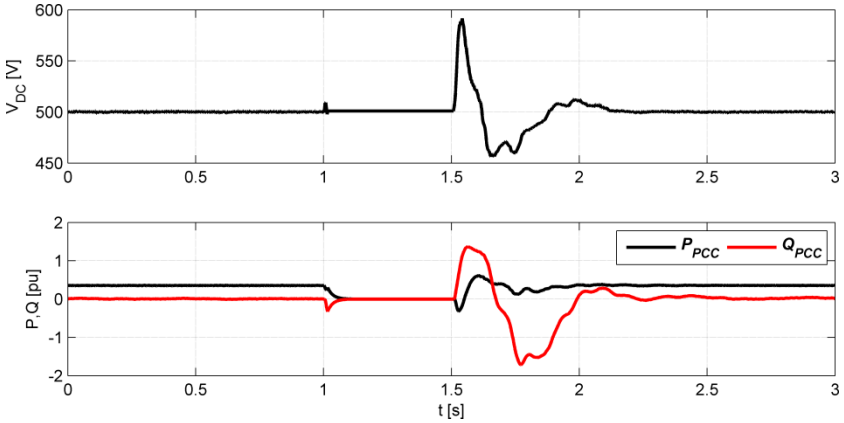

Figure 6-13: photovoltaic plant response to the fault (base power 250 kVA) (© 2013 IEEE).

The WT as well reacts properly as shown in the plots of Figure 6-14. In particular the relation between voltage at the PCC and reference of q-current component is clear and matches with DCRS requirement. For the considered fault scenario the WT is not forced to limit the active power output during FRT operation, as shown in Figure 6-14c.

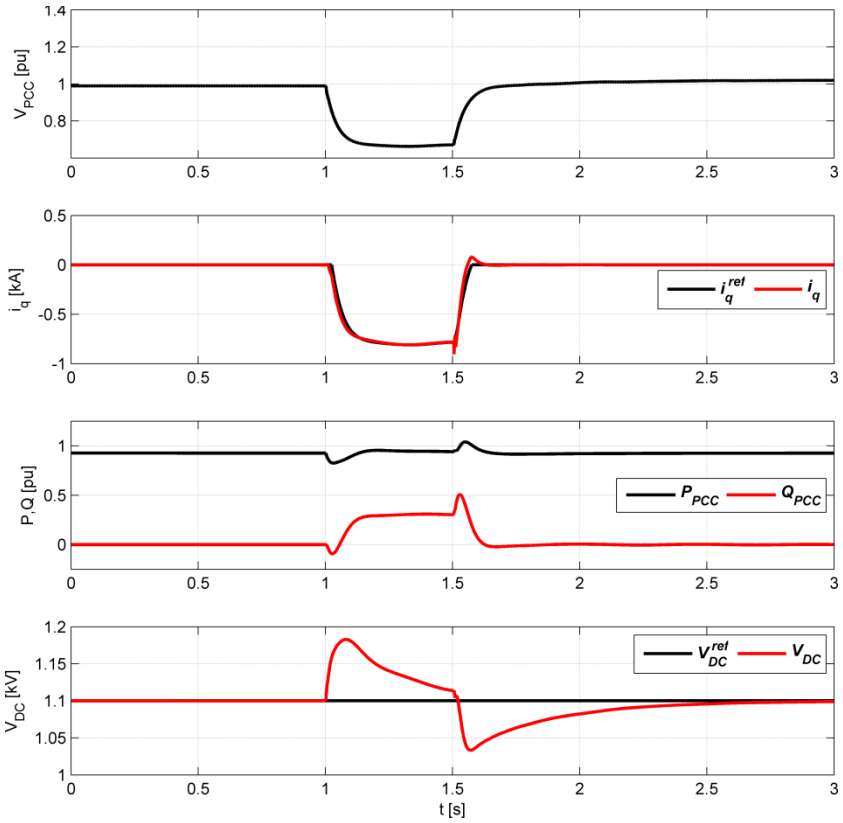

Figure 6-14: wind turbine response to the fault (base power 1.5 MVA) (© 2013 IEEE).

Moreover Figure 6-13 and Figure 6-14 confirm that power electronically interfaced DGs have fast responses. The exclusion of time dependant units from the reduction method, as the case of the synchronous generator based CHP connected to the internal subsystem, is instead confirmed by the profiles in Figure 6-12. After the fault clearing in fact a small and slow voltage oscillation occurs due to the long transient associated to the machine rotor and field current equations.

6.4 CONCLUSIONS

The performances and advantages of proposed reduction method appear evident. A good matching between detailed and reduced models is obtained. The large amount of data following the mapping process turned out bearable by modern tools. Moreover irradiance and wind predictors well fit to such kind of reduction process.

This method on the other hand suffers of some severe limitations. Such approach indeed requires the knowledge of external factors and the detailed information regarding network topology, beyond its real time status. Moreover it turned out not suitable for synchronous generator based DGs, like CHPs and hydro-power plants.

Further work could address following issues not tackled in this treatise:

- Behaviour in case of asymmetrical faults and frequency perturbations;
- Consideration of disconnection times allowed during LVRT and HVRT;

Moreover a stochastic approach could likely overcome the drawbacks and limitation occurring whenever considering several external factors. In this case indeed previously proposed mapping method could turn out too resource demanding.

CHAPTER 7

CONCLUSIONS AND FUTURE WORK

The conclusions about the overall thesis are here given. Beyond the work contributions some comments about thesis development are reported. Moreover this chapter includes the hints for extending the contents of this thesis in the future.

7.1 CONCLUSIONS

The overall thesis covers the control of DGs and their integration in modern DNs. This purpose is achieved combining power system, control and power electronics competences, making a broad use of advanced functions offered by PSCAD® and MATLAB®-Simulink tools. The thesis proposes in several cases analytical studies, frequently symbolically carried out in order to be a reference on these specific subjects. Just the comparison of different approaches is frequently given, in order to highlight pros and cons of considered methods.

The advantages of VSC interfaced LV Flexible DGs, as SBU and MT, are presented since the introduction. The state of the art section presents models and control techniques on the topic.

An assessment of different VSC models for transient studies is given with the aim of providing a guideline for selecting the best representation on the base of simulation purpose and available resources. The choice and design of a passive damped LCL filter is fully demonstrated. Just the possibility to operate these LV flexible DGs both in grid connected and island modes prompted the author to deepen their corresponding control schemes. The current controlled mode is assessed with respect to the grid impedance variations, the current sensor position and the difference of approximated and detailed plant transfer function are analyzed in detail. Results confirm that simplified plant transfer functions are acceptable. Moreover proposed filter appears suitable for a wide range of grid impedance values, justifying the absence of any virtual resistances. The operation as a voltage controlled unit, just without any

virtual impedance but taking into consideration the power decoupling matrix, is considered, with a cascade of a voltage and current regulators. Maintaining the voltage sensor on the filter shunt branch, the compensation of the voltage drop on the grid inductance is considered. The corresponding Thevenin equivalent is analytically given, a significant contribution since LCL interfaced voltage controlled VSCs are rarely debated in literature.

The overall modelling of these LV flexible units is presented for integration studies. In this framework a novel model of a battery is proposed and compared with a similar purpose model available in literature. Then the operation of VSC interfaced DGs in a hierarchical MG is studied. The traditional direct droop control scheme is considered; as well it is given evidence about the drawbacks of reverse droop for managing such kind of system. The benefits of these units is analysed in the case of intentional islanding of a distribution feeder. The control schemes modifications necessary in order to dispatch power through a direct drooped unit in presence of secondary control is considered.

Similarly to aforementioned flexible LV DGs, a DE can be exploited as a flexible unit. In this work the tuning of a reactive power regulator, acting on the brushless exciter voltage reference is studied. In particular the effects of different equivalent Thevenin impedance values are tackled, both for steady state and dynamic points of view. The latter turned out interesting for highlighting that AC5A exciter performs voltage regulation featured by a steady state error. Its magnitude is analytically determined starting from classical K-parameter model developed for power system stability studies. The tuning of the reactive power regulator is done in order to obtain not only a stable closed loop response, but a predefined step response. Such goal was pursued through two alternative methods. Starting from K-parameter model two analytical methods are proposed. *A method* is suitable for constant active power operation and it relies on the load flow Jacobian elements. *B method* on the other hand relies on overall small signal model of the system and led developing an "extended" K-parameter model. An alternative tuning of the reactive power regulator is proposed making use of optimisation driven multiple runs. The application of Nelder-Mead Simplex method already proposed in literature for nonlinear system, was here enhanced formulating novel objective functions based on the step response characteristics. Results of both methods are compared, highlighting the pros of optimization driven multiple runs both in terms of precision and reduction of tuning time.

Once deepened these control issues the focus of the thesis moved to the reduction of active radial DN for system stability studies. Here a novel idea is proposed, relying on the decoupling time dynamics of synchronous generator respect to VSC inter-

faced DGs and loads. The methodology is here described, highlighting its pros and cons. Then taking into account the simplified model of a Danish rural DN the comparison of its detail representation and the model including the equivalent is given. Results confirm that under initial assumption this reduction method is effective.

In short the thesis contributed to:

- Provide a comparison of different VSC models for transient studies;
- Investigate the usage of a passive damped LCL filter for the operation of a VSC in current and voltage control modes;
- Provide a comparison between direct droop with angle bias, direct droop with frequency bias and reverse droop VSC control schemes for the operation of an islanded MG;
- Tune the reactive power regulator of a SG by considering the grid impedance and given Characteristic Indices. This work led to formulate some novel objective functions for optimization based tunings. Moreover the small signal analyses is formulated and validated;
- Propose an aggregation method for radial DN in presence of VSC interfaced DGs.

As a final conclusion the author would like to remark that the contents of this thesis are the outcome of the ideas and the learning process matured during his PhD stay at the Department of Energy Technology at Aalborg University, while they don't necessarily reflect the view of ABB DMPC PG Solar or ABB Power Grids. Certainly the following industrial career of the author contributed to add some practical considerations to the overall work. Under this perspective here proposed LCL filter inductances appears too large for an industrial product, as well as the passive damping solution and the decoupling matrixes are likely losing choices respect to virtual impedance and admittance based schemes. Moreover the adoption of more complete tools, as DIgSILENT - Power Factory would have eased the implementation of the proposed network reduction method.

7.2 FUTURE WORK

In this work the adoption of the virtual impedance is not investigated, neither for damping the LCL filter nor for shaping the Thevenin impedance of the equivalent voltage controlled VSC. A comparison with here proposed passive damped solution and decoupling matrix would be certainly interesting. Lower values of the damping resistor moreover would certainly affect the output impedance of the VSC, with the possibility of grid impedance estimation need for properly applying the decoupling matrix. With this reference the evaluation of the stability margin given a wrong impedance value would be certainly a very interesting work. The direct droop con-

trol via phase bias looks a viable solution for the operation of a VSC in both grid connected and islanded modes, nevertheless further work would be necessary for making this scheme more robust respect to grid perturbations. Moreover if grid code regulation would allow the intentional islanding then the operation through 4 wires of LV flexible units should be addressed.

Proposed reactive power controller tuning methods appears very interesting, bridging time and Laplace domains. Widening the treatise to constant power factor operation would certainly complete an analytical treatise of all synchronous generator modes. The same methodology could be adopted for carrying out an extensive parametric stability assessment of voltage and reactive power controlled SG. Moreover it could allow performing online adaptive regulator tunings. The engine of the Nelder-Mead Simplex optimization used was offered directly by PSCAD® so any designer exploiting different tools should write on her/his own the corresponding script.

The reduction method here proposed could be broadened to asymmetrical grid conditions. Moreover combining this method with irradiance and wind predictors appears a great opportunity for carrying out grid analyses studies in the short time horizon. Finally, as already mentioned, the adoption of a different power system tool, as DIgSILENT – PowerFactory, would certainly ease the mapping process.

REFERENCES

[1] J. Rifkin, *The zero marginal cost society: the internet of things, the collaborative commons and the eclipse of capitalism*: Palgrave Macmillan, 2014.

[2] N. Jenkins and E. Institution of Electrical, *Embedded Generation*: Institution of Engineering and Technology, 2000.

[3] D. Pudjianto, C. Ramsay, and G. Strbac, "Virtual power plant and system integration of distributed energy resources," *Renewable Power Generation, IET,* vol. 1, pp. 10-16, 2007.

[4] FENIX, "Flexible Electricity Networks to Integrate the eXpected energy evolution: results," www.smartgrids.eu/documents/projects/2009.

[5] PowerMatcher. *flexiblepower.github.io*.

[6] Flexitricity. *www.flexitricity.com*.

[7] R. H. Lasseter, "MicroGrids," in *Power Engineering Society Winter Meeting, 2002. IEEE*, 2002, pp. 305-308 vol.1.

[8] L. Yunwei, D. M. Vilathgamuwa, and L. Poh Chiang, "Design, analysis, and real-time testing of a controller for multibus microgrid system," *IEEE Transactions on Power Electronics,* vol. 19, pp. 1195-1204, 2004.

[9] J. M. Guerrero, L. Garcia De Vicuna, J. Matas, M. Castilla, and J. Miret, "A wireless controller to enhance dynamic performance of parallel inverters in distributed generation systems," *IEEE Transactions on Power Electronics,* vol. 19, pp. 1205-1213, 2004.

[10] J. A. Peas Lopes, C. L. Moreira, and A. G. Madureira, "Defining control strategies for MicroGrids islanded operation," *IEEE Transactions on Power Systems,* vol. 21, pp. 916-924, 2006.

[11] F. Katiraei, M. R. Iravani, and P. W. Lehn, "Micro-grid autonomous operation during and subsequent to islanding process," *IEEE Transactions on Power Delivery,* vol. 20, pp. 248-257, 2005.

[12] "IEEE Guide for Design, Operation, and Integration of Distributed Resource Island Systems with Electric Power Systems," *IEEE Std 1547.4-2011,* pp. 1-54, 2011.

[13] The MathWorks Inc., "MATLAB 2014a and SimPowerSystems release 6.1," 2014 ed.

[14] The MathWorks Inc., "MATLAB 2014a and Symbolic Math Toolbox release 6.0," 2014 ed.

[15] The MathWorks Inc., "MATLAB 2014a and Control System Toolbox release 9.7," 2014 ed.

[16] The MathWorks Inc., "MATLAB 2014a and System Identification Toolbox release 9.0," 2014 ed.

[17] ABB. *http://www.abb.com/product/us/9AAC167809.aspx?country=IT*.

[18] ABB. *http://new.abb.com/power-converters-inverters/solar/energy-storage/react-3-6kw-4-6kw*.

[19] Tesla. *www.teslamotors.com/powerwall*.

[20] "IEEE Standard Conformance Test Procedures for Equipment Interconnecting Distributed Resources with Electric Power Systems," *IEEE Std 1547.1-2005,* pp. 1-62, 2005.

[21] IEC, "IEC 62116 Ed. 1," *IEC International Standard,* 2008-2009.

[22] J. A. P. Lopes, C. L. Moreira, and A. G. Madureira, "Defining control strategies for MicroGrids islanded operation," *IEEE Transactions on Power Systems,* vol. 21, pp. 916-924, 2006.

[23] J. M. Guerrero, L. Hang, and J. Uceda, "Control of Distributed Uninterruptible Power Supply Systems," *IEEE Transactions on Industrial Electronics,* vol. 55, pp. 2845-2859, 2008.

[24] W. Xiongfei, J. M. Guerrero, C. Zhe, and F. Blaabjerg, "Distributed energy resources in grid interactive AC microgrids," in *Power Electronics for Distributed Generation Systems (PEDG), 2010 2nd IEEE International Symposium on*, 2010, pp. 806-812.

[25] T. Kawabata and S. Higashino, "Parallel operation of voltage source inverters," *IEEE Transactions on Industry Applications,* vol. 24, pp. 281-287, 1988.

[26] M. C. Chandorkar, D. M. Divan, and R. Adapa, "Control of parallel connected inverters in standalone AC supply systems," *IEEE Transactions on Industry Applications,* vol. 29, pp. 136-143, 1993.

[27] P. Kundur, *Power System Stability and Control*. New York: McGraw-Hill, Inc., 1994.

[28] Q. Shafiee, J. M. Guerrero, and J. C. Vasquez, "Distributed Secondary Control for Islanded Microgrids—A Novel Approach," *IEEE Transactions on Power Electronics,* vol. 29, pp. 1018-1031, 2014.

[29] J. M. Guerrero, L. Garcia de Vicuna, J. Matas, M. Castilla, and J. Miret, "Output Impedance Design of Parallel-Connected UPS Inverters With Wireless Load-Sharing Control," *IEEE Transactions on Industrial Electronics,* vol. 52, pp. 1126-1135, 2005.

[30] J. M. Guerrero, J. Matas, L. G. de Vicuna, M. Castilla, and J. Miret, "Wireless-Control Strategy for Parallel Operation of Distributed-Generation Inverters," *IEEE Transactions on Industrial Electronics,* vol. 53, pp. 1461-1470, 2006.

[31] L. Yun Wei and K. Ching-Nan, "An Accurate Power Control Strategy for Power-Electronics-Interfaced Distributed Generation Units Operating in a Low-Voltage Multibus Microgrid," *IEEE Transactions on Power Electronics,* vol. 24, pp. 2977-2988, 2009.

[32] J. M. Guerrero, J. Matas, V. Luis Garcia de, M. Castilla, and J. Miret, "Decentralized Control for Parallel Operation of Distributed Generation Inverters Using Resistive Output Impedance," *IEEE Transactions on Industrial Electronics,* vol. 54, pp. 994-1004, 2007.

[33] Y. Wei, C. Min, J. Matas, J. M. Guerrero, and Q. Zhao-ming, "Design and Analysis of the Droop Control Method for Parallel Inverters Considering the Impact of the Complex Impedance on the Power Sharing," *IEEE Transactions on Industrial Electronics,* vol. 58, pp. 576-588, 2011.

[34] K. De Brabandere, B. Bolsens, J. Van den Keybus, A. Woyte, J. Driesen, and R. Belmans, "A Voltage and Frequency Droop Control Method for Parallel Inverters," *IEEE Transactions on Power Electronics,* vol. 22, pp. 1107-1115, 2007.

[35] J. C. Vasquez, J. M. Guerrero, A. Luna, P. Rodriguez, and R. Teodorescu, "Adaptive Droop Control Applied to Voltage-Source Inverters Operating in Grid-Connected and Islanded Modes," *IEEE Transactions on Industrial Electronics,* vol. 56, pp. 4088-4096, 2009.

[36] A. Nagliero, R. A. Mastromauro, V. G. Monopoli, M. Liserre, and A. Dell'Aquila, "Analysis of a universal inverter working in grid-connected, stand-alone and micro-grid," in *Industrial Electronics (ISIE), 2010 IEEE International Symposium on*, 2010, pp. 650-657.

[37] S. N. D.N. Gaonkar, "Modeling and performance analysis of microturbine based Distributed Generation system, “a review”," in *Energytech, 2011 IEEE*, 2011, pp. 1 - 6.

[38] Y. Soon Kiat, J. V. Milanovic, and F. M. Hughes, "Overview and Comparative Analysis of Gas Turbine Models for System Stability Studies," *IEEE Transactions on Power Systems,* vol. 23, pp. 108-118, 2008.

[39] J. H. Kim, T. S. Kim, and S. T. Ro, "Analysis of the dynamic behaviour of regenerative gas turbines," *Proceedings of the Institution of Mechanical Engineers, Part A: Journal of Power and Energy,* vol. 215, pp. 339-346, 2001.

[40] S. Haugwitz, "Modelling of microturbine systems," *Surge,* vol. 2, p. 1, 2002.

[41] R. Lasseter, "Dynamic models for micro-turbines and fuel cells," in *Power Engineering Society Summer Meeting, 2001*, 2001, pp. 761-766 vol.2.

[42] A. Bertani, C. Bossi, F. Fornari, S. Massucco, S. Spelta, and F. Tivegna, "A microturbine generation system for grid connected and islanding operation," in *Power Systems Conference and Exposition, 2004. IEEE PES*, 2004, pp. 360-365 vol.1.

[43] A. Mohamed, M. Nizam, and A. A. Salam, "Performance evaluation of fuel cell and microturbine as distributed generators in a microgrid," *European Journal of Scientific Research,* vol. 30, pp. 554-570, 2009.

[44] A. Al-Hinai and A. Feliachi, "Dynamic model of a microturbine used as a distributed generator," in *System Theory, 2002. Proceedings of the Thirty-Fourth Southeastern Symposium on*, 2002, pp. 209-213.

[45] S. R. Guda, C. Wang, and M. H. Nehrir, "A Simulink-based microturbine model for distributed generation studies," in *Power Symposium, 2005. Proceedings of the 37th Annual North American*, 2005, pp. 269-274.

[46] D. N. Gaonkar and R. N. Patel, "Modeling and simulation of microturbine based distributed generation system," in *Power India Conference, 2006 IEEE*, 2006, p. 5 pp.

[47] W. Huang, J. Zhang, Z. Wu, and M. Niu, "Dynamic modelling and simulation of a Micro-turbine generation system in the microgrid," in *Sustainable Energy Technologies, 2008. ICSET 2008. IEEE International Conference on*, 2008, pp. 345-350.

[48] A. K. Saha, S. Chowdhury, S. P. Chowdhury, and P. A. Crossley, "Modeling and Performance Analysis of a Microturbine as a Distributed Energy Resource," *Energy Conversion, IEEE Transactions on,* vol. 24, pp. 529-538, 2009.

[49] M. Z. C. Wanik and I. Erlich, "Simulation of microturbine generation system performance during grid faults under new grid code requirements," in *PowerTech, 2009 IEEE Bucharest*, 2009, pp. 1-8.

[50] L. Gang, L. Gengyin, Y. Wei, Z. Ming, and K. L. Lo, "Modeling and simulation of a microturbine generation system based on PSCAD/EMTDC," in *Critical Infrastructure (CRIS), 2010 5th International Conference on*, 2010, pp. 1-6.

[51] R. Noroozian, M. Abedi, G. B. Gharehpetian, and S. H. Hosseini, "Modelling and Simulation of Microturbine Generation System for on-grid and off-grid Operation Modes," in *International Conference on Renewable Energies and Power Quality*, 2009.

[52] H. Nikkhajoei and M. R. Iravani, "A matrix converter based micro-turbine distributed generation system," *Power Delivery, IEEE Transactions on,* vol. 20, pp. 2182-2192, 2005.

[53] G. J. Kish and P. W. Lehn, "A micro-turbine model for system studies incorporating validated thermodynamic data," in *Power and Energy Society General Meeting, 2011 IEEE*, 2011, pp. 1-6.

[54] M. Z. C. Wanik and I. Erlich, "Dynamic simulation of microturbine distributed generators integrated with multi-machines power system network," in *Power and Energy Conference, 2008. PECon 2008. IEEE 2nd International*, 2008, pp. 1545-1550.

[55] P. Eguia, I. Zamora, E. Torres, J. I. San Martín, M. Moya, J. C. Bruno*, et al.*, "Modelling and Simulation of a Microturbine Turing Transient Events," in *International Conference on Renewable Energies and Power Quality*, Granada, 2010.

[56] M. Ceraolo, "New dynamical models of lead-acid batteries," *Power Systems, IEEE Transactions on,* vol. 15, pp. 1184-1190, 2000.

[57] O. Tremblay, L. A. Dessaint, and A. I. Dekkiche, "A Generic Battery Model for the Dynamic Simulation of Hybrid Electric Vehicles," in *Vehicle Power and Propulsion Conference, 2007. VPPC 2007. IEEE*, 2007, pp. 284-289.

[58] J. Machowski, J. Bialek, and D. J. Bumby, *Power System Dynamics: Stability and Control*: Wiley, 2008.

[59] T. L. Baldwin, L. Mili, and A. G. Phadke, "Dynamic Ward equivalents for transient stability analysis," *IEEE Transactions on Power Systems,* vol. 9, pp. 59-67, 1994.

[60] A. J. Germond and R. Podmore, "Dynamic Aggregation of Generating Unit Models," *IEEE Transactions on Power Apparatus and Systems,* vol. PAS-97, pp. 1060-1069, 1978.

[61] R. Singh, M. Elizondo, and L. Shuai, "A review of dynamic generator reduction methods for transient stability studies," in *Power and Energy Society General Meeting, 2011 IEEE*, 2011, pp. 1-8.

[62] P. Marku and A. Sebastian, "Aggregated Wind Park Models for Analysing Power System Dynamics," www.digsilent.ru2003.

[63] T. L. Le, Q. T. Tran, O. Devaux, O. Chilard, and R. Caire, "Reduction and aggregation for critical and emergency operation of distribution network in presence of distributed generators," in *Electricity Distribution - Part 1, 2009. CIRED 2009. 20th International Conference and Exhibition on*, 2009, pp. 1-4.

[64] L. V. Tan and D. C. Lee, "Developing Function Models of Back-to-Back PWM Converters for Simplified Simulation," *Journal of Power Electronics,* vol. 11, pp. 51-58, Jan 2011.

[65] M. Hernes, K. Ljøkelsøy, T. Kleppa, and O. Mo, "Average model of PWM converter," Sintef Energy Research, www.sintef.no2003.

[66] M. Liserre *, F. Blaabjerg, and A. Dell'Aquila, "Step-by-step design procedure for a grid-connected three-phase PWM voltage source converter," *International Journal of Electronics,* vol. 91, pp. 445-460, 2004/08/01 2004.

[67] M. Liserre, F. Blaabjerg, and S. Hansen, "Design and control of an LCL-filter-based three-phase active rectifier," *IEEE Transactions on Industry Applications,* vol. 41, pp. 1281-1291, Sep-Oct 2005.

[68] R. Teodorescu, M. Liserre, and P. Rodriguez, *Grid Converters for Photovoltaic and Wind Power Systems*: Chichester, U.K. : Wiley, 2011.

[69] R. Beres, W. Xiongfei, F. Blaabjerg, C. L. Bak, and M. Liserre, "A review of passive filters for grid-connected voltage source converters," in *Applied Power Electronics Conference and Exposition (APEC), 2014 Twenty-Ninth Annual IEEE*, 2014, pp. 2208-2215.

[70] H. W. van der Broeck, H. C. Skudelny, and G. V. Stanke, "Analysis and realization of a pulsewidth modulator based on voltage space vectors," *IEEE Transactions on Industry Applications,* vol. 24, pp. 142-150, 1988.

[71] C. Bajracharya, M. Molinas, J. A. Suul, and T. M. Undeland, "Understanding of tuning techniques of converter controllers for VSC-HVDC," in *Nor-*

dic Workshop on Power and Industrial Electronics (NORPIE/2008), June 9-11, 2008, Espoo, Finland, 2008.

[72] V. Blasko and V. Kaura, "A new mathematical model and control of a three-phase AC-DC voltage source converter," *IEEE Transactions on Power Electronics,* vol. 12, pp. 116-123, 1997.

[73] M. P. Kaźmierkowski, R. Krishnan, and F. Blaabjerg, *Control in Power Electronics: Selected Problems*: Academic Press, 2002.

[74] P. Mattavelli and S. Buso, *Digital Control in Power Electronics*: Morgan and Claypool, 2006.

[75] A. Kahrobaeian and Y. A. R. I. Mohamed, "Robust Single-Loop Direct Current Control of LCL-Filtered Converter-Based DG Units in Grid-Connected and Autonomous Microgrid Modes," *IEEE Transactions on Power Electronics,* vol. 29, pp. 5605-5619, 2014.

[76] A. Nagliero, D. Ricchiuto, R. A. Mastromauro, and M. Liserre, "Management of grid-inverter outages and power quality disturbances in distributed power generation systems," in *IECON 2010 - 36th Annual Conference on IEEE Industrial Electronics Society*, 2010, pp. 3022-3027.

[77] T. L. Vandoorn, C. M. Ionescu, J. D. M. De Kooning, R. De Keyser, and L. Vandevelde, "Theoretical Analysis and Experimental Validation of Single-Phase Direct Versus Cascade Voltage Control in Islanded Microgrids," *IEEE Transactions on Industrial Electronics,* vol. 60, pp. 789-798, 2013.

[78] M. Savaghebi, J. C. Vasquez, A. Jalilian, J. M. Guerrero, and L. Tzung-Lin, "Selective harmonic virtual impedance for voltage source inverters with LCL filter in microgrids," in *Energy Conversion Congress and Exposition (ECCE), 2012 IEEE*, 2012, pp. 1960-1965.

[79] I. J. Balaguer, L. Qin, Y. Shuitao, U. Supatti, and P. Fang Zheng, "Control for Grid-Connected and Intentional Islanding Operations of Distributed Power Generation," *IEEE Transactions on Industrial Electronics,* vol. 58, pp. 147-157, 2011.

[80] M. Rizo, M. Liserre, E. Bueno, F. J. Rodriguez, and C. Giron, "Voltage Control Architectures for the Universal Operation of DPGS," *IEEE Transactions on Industrial Informatics,* vol. 11, pp. 313-321, 2015.

[81] K. Strunz, R. H. Fletcher, R. Campbell, and F. Gao, "Developing benchmark models for low-voltage distribution feeders," in *Power & Energy Society General Meeting, 2009. PES '09. IEEE*, 2009, pp. 1-3.

[82] P. Raboni, H. Weihao, S. K. Chaudhary, and C. Zhe, "Modeling and control of low voltage flexible units for enhanced operation of distribution

feeders," in *Industrial Electronics Society, IECON 2013 - 39th Annual Conference of the IEEE*, 2013, pp. 7469-7474.

[83] R. W. Erickson and D. Maksimovic, *Fundamentals of Power Electronics*: Springer, 2001.

[84] "Rechargeable lithium-ion battery VL 37570," S. batteries, Ed., ed. http://www.saftbatteries.com/, 2009.

[85] J. R. Pillai and B. Bak-Jensen, "Integration of Vehicle-to-Grid in the Western Danish Power System," *IEEE Transactions on Sustainable Energy,* vol. 2, pp. 12-19, 2011.

[86] S. Xiaofeng, T. Yanjun, and C. Zhe, "Adaptive decoupled power control method for inverter connected DG," *Renewable Power Generation, IET,* vol. 8, pp. 171-182, 2014.

[87] A. V. Timbus, P. Rodriguez, R. Teodorescu, and M. Ciobotaru, "Line Impedance Estimation Using Active and Reactive Power Variations," in *Power Electronics Specialists Conference, 2007. PESC 2007. IEEE*, 2007, pp. 1273-1279.

[88] M. Ciobotaru, V. Agelidis, and R. Teodorescu, "Line impedance estimation using model based identification technique," in *Power Electronics and Applications (EPE 2011), Proceedings of the 2011-14th European Conference on*, 2011, pp. 1-9.

[89] N. Hoffmann and F. W. Fuchs, "Online grid impedance estimation for the control of grid connected converters in inductive-resistive distributed power-networks using extended kalman-filter," in *Energy Conversion Congress and Exposition (ECCE), 2012 IEEE*, 2012, pp. 922-929.

[90] G. Herong, G. Xiaoqiang, W. Deyu, and W. Weiyang, "Real-time grid impedance estimation technique for grid-connected power converters," in *Industrial Electronics (ISIE), 2012 IEEE International Symposium on*, 2012, pp. 1621-1626.

[91] R. Majumder, A. Ghosh, G. Ledwich, and F. Zare, "Angle droop versus frequency droop in a voltage source converter based autonomous microgrid," in *Power & Energy Society General Meeting, 2009. PES '09. IEEE*, 2009, pp. 1-8.

[92] SMA, "SMA Fuel Save Controller, Technical Information: Functional Description."

[93] G. Vincent, C. Frederik, and K. Laurent, "Risk of stabilisation of islanding situation by local regulations," in *CIRED WorkShop*, Rome, 2014.

[94] N. Jenkins, "Embedded generation. Part 1," *Power Engineering Journal,* vol. 9, pp. 145-150, 1995.

[95] T. L. Vandoorn, B. Meersman, J. D. M. De Kooning, and L. Vandevelde, "Directly-Coupled Synchronous Generators With Converter Behavior in Islanded Microgrids," *IEEE Transactions on Power Systems,* vol. 27, pp. 1395-1406, 2012.

[96] F. P. Demello and C. Concordia, "Concepts of Synchronous Machine Stability as Affected by Excitation Control," *IEEE Transactions on Power Apparatus and Systems,* vol. PAS-88, pp. 316-329, 1969.

[97] P. Raboni, S. Chaudhary, and Z. Chen, "Design of Reactive Power Regulator for Synchronous Generator assigned Characteristic Index Objectives and considering Grid Impedance Angle," *IET Generation Transmission and Distribution,* (submitted Dec. 2015).

[98] S. Roy, O. P. Malik, and G. S. Hope, "An adaptive control scheme for speed control of diesel driven power-plants," *IEEE Transactions on Energy Conversion,* vol. 6, pp. 605-611, 1991.

[99] D. Canever, G. J. W. Dudgeon, S. Massucco, J. R. McDonald, and F. Silvestro, "Model validation and coordinated operation of a photovoltaic array and a diesel power plant for distributed generation," in *Power Engineering Society Summer Meeting, 2001*, 2001, pp. 626-631 vol.1.

[100] A. Elmitwally and M. Rashed, "Flexible Operation Strategy for an Isolated PV-Diesel Microgrid Without Energy Storage," *IEEE Transactions on Energy Conversion,* vol. 26, pp. 235-244, 2011.

[101] H. W. Dommel and A. Bonneville Power, *Electromagnetic Transients Program Reference Manual: (EMTP) Theory Book*: Bonneville Power Administration, 1986.

[102] A. E. Fitzgerald, C. J. Kingsley, and S. D. Umans, *Electric Machinery*, Sixth ed.: McGraw-Hill, 2003.

[103] S. M. L. Kabir and R. Shuttleworth, "Brushless exciter model," *Generation, Transmission and Distribution, IEE Proceedings-,* vol. 141, pp. 61-67, 1994.

[104] "IEEE Recommended Practice for Excitation System Models for Power System Stability Studies," *IEEE Std 421.5-2005 (Revision of IEEE Std 421.5-1992),* pp. 0_1-85, 2006.

[105] *EMTDC User's Guide*. Manitoba, MB, Canada, 2005.

[106] J. C. Lagarias, J. A. Reeds, M. H. Wright, and P. E. Wright, "Convergence Properties of the Nelder-Mead Simplex Method in low dimensions," *SIAM Journal of Optimization,* vol. 9, pp. 112-147, 1998.

[107] S. Filizadeh, "Optimization-Enabled Electromagnetic Transient Simulation," PhD Thesis, University of Manitoba, 2004.

[108] J. A. Nocedal and S. J. Wright, *Numerical Optimization*: Springer-Verlag New York, 1999.

[109] A. M. Gole, S. Filizadeh, R. W. Menzies, and P. L. Wilson, "Optimization-enabled electromagnetic transient simulation," *IEEE Transactions on Power Delivery,* vol. 20, pp. 512-518, 2005.

[110] S. Filizadeh, A. M. Gole, D. A. Woodford, and G. D. Irwin, "An Optimization-Enabled Electromagnetic Transient Simulation-Based Methodology for HVDC Controller Design," *IEEE Transactions on Power Delivery,* vol. 22, pp. 2559-2566, 2007.

[111] A. M. Vural and K. C. Bayindir, "Optimization of parameter set for STATCOM control system," in *Transmission and Distribution Conference and Exposition, 2010 IEEE PES*, 2010, pp. 1-6.

[112] M. A. Duarte-Mermoud and R. A. Prieto, "Performance index for quality response of dynamical systems," *ISA transactions,* vol. 43, pp. 133-151, 2004.

[113] C. T. Chen, *Analog and Digital Control System Design: Transfer-function, State-space, and Algebraic Methods*: Saunders College Pub., 1993.

[114] B. Eryilmaz, R. Chen, and P. Gahinet, "WO2010141046A1 - Automated pid controller design," 2010.

[115] P. Raboni and C. Zhe, "Reduction method for active distribution networks," in *PowerTech (POWERTECH), 2013 IEEE Grenoble*, 2013, pp. 1-6.

[116] P. Mahat, *Control and Operation of Islanded Distribution System: A Dissertation Submitted to the Faculty of Engineering, Science and Medicine, Aalborg University in Partial Fulfillment for the Degree of Doctor of Philosophy*: Department of Energy Technology, Aalborg University, 2010.

[117] W. Hu, Z. Chen, Y. Wang, and Z. Wang, "Flicker Mitigation by Active Power Control of Variable-Speed Wind Turbines With Full-Scale Back-to-Back Power Converters," *IEEE Transactions on Energy Conversion,* vol. 24, pp. 640-649, 2009.

[118] Energinet.dk, "Technical regulation 3.2.5 for wind power plants with a power output greater than 11kW," ed: Energinet.dk, 2010, p. 74.

[119] A. D. Rajapakse and D. Muthumuni, "Simulation tools for photovoltaic system grid integration studies," in *Electrical Power & Energy Conference (EPEC), 2009 IEEE*, 2009, pp. 1-5.

[120] S. J. Mason, "Feedback Theory-Some Properties of Signal Flow Graphs," *Proceedings of the IRE,* vol. 41, pp. 1144-1156, 1953.

[121] C. M. Velèz, "Symbolic reduction of block diagrams and signal flow graphs," www.mathworks.com/matlabcentral/fileexchange/.

APPENDICES

A.1. Definition of VSC current control scheme 1
A.2. Modulus Optimum Criteria 3
A.3. Rowen Gas Turbine model 5
A.4. Control scheme reduction: “extended” K-parameter model case 6
A.5. Small synchronous generator and electrical network data 9

A.1. Definition of VSC current control scheme

With reference to Figure 3-7 neglecting the filter shunt branch, the single phase KVL is:

$$e_{inv} - e_g = L\frac{di}{dt} + Ri \tag{A.1}$$

Where:

$$L = L_1 + L_2 + L_g \tag{A.2}$$

$$R = R_1 + R_2 + R_g \tag{A.3}$$

Considering the corresponding of equation (A.1) in the synchronous *dq0* reference frame becomes:

$$v_{inv}^{dq0} - v_{grid}^{dq0} = T(\theta)\left\{L\frac{di}{dt}\right\} + Ri^{dq0}$$

$$v_{inv}^{dq0} - v_{grid}^{dq0} = T(\theta)\left\{L\left[\frac{d}{dt}\left(T(\theta)^{-1}\cdot I^{dq0}\right)\right]\right\} + Ri^{dq0}$$

$$v_{inv}^{dq0} - v_{grid}^{dq0} = T(\theta)\left\{L\left[\frac{d}{dt}T(\theta)^{-1}\cdot I^{dq0} + T(\theta)^{-1}\cdot\frac{d}{dt}I^{dq0}\right]\right\} + Ri^{dq0}$$

$$v_{inv}^{dq0} - v_{grid}^{dq0} = T(\theta)\left\{L\left[\frac{\partial}{\partial\theta}\frac{\partial\theta}{\partial t}T(\theta)^{-1}\cdot i^{dq0} + T(\theta)^{-1}\cdot\frac{dI^{dq0}}{dt}\right]\right\} + Ri^{dq0}$$

$$v_{inv}^{dq0} - v_{grid}^{dq0} = \omega L\cdot T(\theta)\frac{\partial T(\theta)^{-1}}{\partial\theta}\cdot i^{dq0} + L\frac{di^{dq0}}{dt} + Ri^{dq0}$$

$$v_{inv}^{dq0} - v_{grid}^{dq0} = \omega L\cdot\begin{bmatrix}0 & -1 & 0\\ 1 & 0 & 0\\ 0 & 0 & 0\end{bmatrix}\cdot i^{dq0} + L\frac{di^{dq0}}{dt} + Ri^{dq0}$$

$$v_{inv}^{dq0} - v_{grid}^{dq0} = -\omega L\cdot\begin{bmatrix}i^q\\ -i^d\\ 0\end{bmatrix} + L\frac{di^{dq0}}{dt} + Ri^{dq0}$$

$$v_{inv}^{dq0} - v_{grid}^{dq0} = \begin{bmatrix}R & -\omega L & 0\\ \omega L & R & 0\\ 0 & 0 & R\end{bmatrix}i^{dq0} + L\frac{di^{dq0}}{dt} \tag{A.4}$$

Since traditional inverters are three wires devices, the zero sequence can be neglected:

$$v_{inv}^{dq} - v_{grid}^{dq} = \begin{bmatrix} R & -\omega L \\ \omega L & R \end{bmatrix} i^{dq} + L\frac{di^{dq}}{dt} \tag{A.5}$$

Equation (A.5) can be easily put in the form of linear system in fact:

$$\frac{di^{dq}}{dt} = \begin{bmatrix} -\frac{R}{L} & \omega \\ -\omega & -\frac{R}{L} \end{bmatrix} i^{dq} + \frac{1}{L}\left\{v_{inv}^{dq} - v_{grid}^{dq}\right\} \Leftrightarrow \dot{x} = Ax + Bu + Cd \tag{A.6}$$

Equation (A.6) is graphically shown in the plant frame of Figure 3-10.

A.2. Modulus Optimum Criteria

In order to achieve the fastest possible response the plant dominant pole must be cancelled with the regulator zero. This implies:

$$T_i = \tau \tag{A.7}$$

The closed loop transfer function becomes:

$$G_{CL}(s) = \frac{L(s)}{1+L(s)} = \frac{\dfrac{k_p}{1.5RT_ST_i}}{s^2 + \dfrac{s}{1.5T_S} + \dfrac{k_p}{1.5RT_ST_i}} \tag{A.8}$$

This fits to the characteristic form of a second order transfer function:

$$G_{II}(s) = \frac{\omega_n^2}{s^2 + 2\zeta\omega_n s + \omega_n^2} \tag{A.9}$$

Where with reference to the scheme in Figure A-1 can be identified:

- Natural pulsation $\omega_n = \sqrt{a^2 + b^2}$;
- Damping factor $\zeta = -\dfrac{a}{\sqrt{a^2 + b^2}}$.

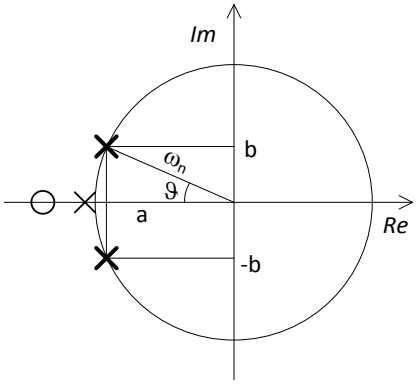

Figure A-1: dominant pole location and relation with natural pulsation and damping factor

Moreover in case of step input the relation between damping factor and overshoot becomes:

$$\frac{s_{\%}}{100} = e^{-\frac{\pi\zeta}{\sqrt{1-\zeta^2}}} \tag{A.10}$$

Considering a 5% overshoot to the step input, equivalent to damping factor $\zeta = \frac{1}{\sqrt{2}}$, are found from (A.8) and (A.10) the natural pulsation ω_n and the controller proportional gain k_p:

$$k_p = \frac{L}{3T_S} \tag{A.11}$$

Given (A.7) the integral gain k_i:

$$k_i = \frac{k_p}{T_i} \tag{A.12}$$

A.3. Rowen Gas Turbine model

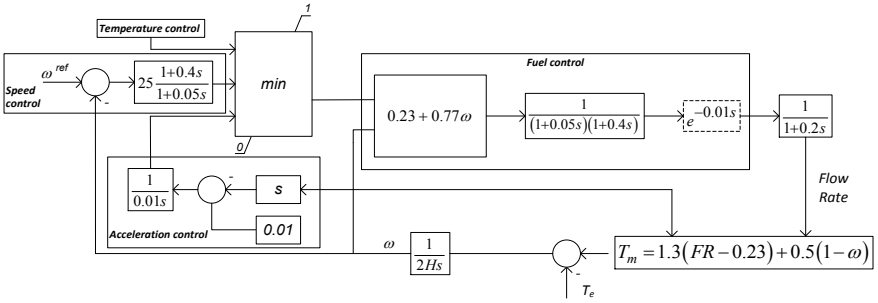

Figure A-2: Rowen model neglecting the exhaust temperature controller

A.4. Control scheme reduction: "extended" K-parameter model case

Determining the transfer function in case of a given complex control scheme could turn out a rather time consuming task. That is the case of the "extended" k- parameter model shown in Figure 5-12. In Figure A-3 the reductions steps following basic control scheme knowledge are shown.

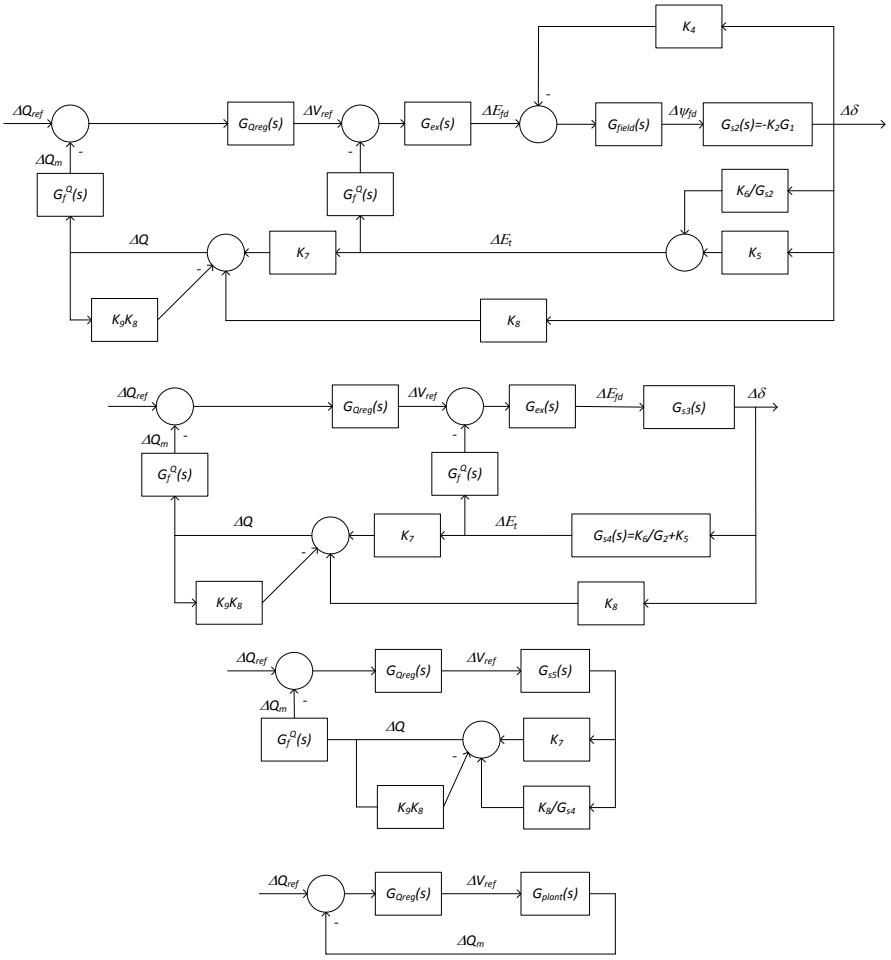

Figure A-3: block scheme reduction process.

Alternatively the closed loop transfer function can be computed applying Mason’s rule [120]. The control scheme has to be transformed in a graph scheme, labelling all the signals as shown in Figure A-4. In order to benefit of modern tools [14] it is then necessary expliciting each signal as $x = \sum k_y y$:

$$
\begin{array}{lll}
b - a + v = 0 & i + h + l = 0 & p - G_f^V o = 0 \\
c - G_{reg}^Q b = 0 & j - G_{mec} i = 0 & q - K_7 o = 0 \\
d - c + p = 0 & k - K_4 j = 0 & r - j + u = 0 \\
e - G_{ex} d = 0 & l - K_1 j = 0 & s - K_8 r = 0 \\
f - e + k = 0 & m - K_5 j = 0 & t - q - s = 0 \\
g - G_{field} f = 0 & n - K_6 g = 0 & u - K_9 t = 0 \\
h - K_2 g = 0 & o - m - n = 0 & v - G_f^Q t = 0
\end{array}
\qquad \text{(A.13)}
$$

Through the coefficients of (A.13), following the procedure and instructions given [121] the closed loop transfer function can be symbolically found automatically.

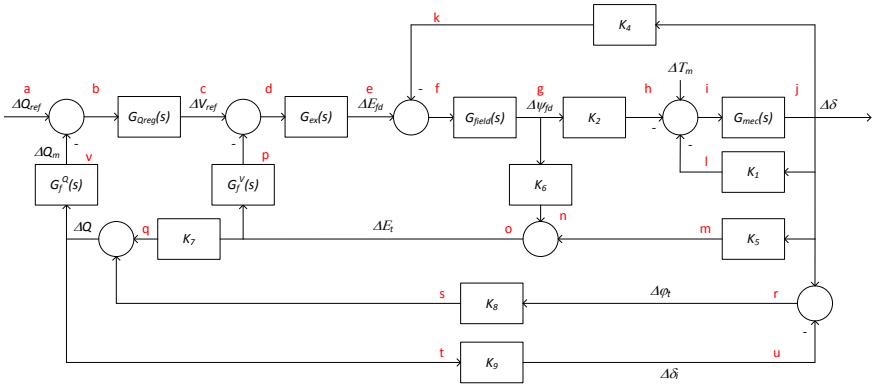

Figure A-4: labelling according to Mason’s rule.

Both alternative methods lead to following closed loop transfer function:

$$
\begin{aligned}
G_{CL}^{Q} &= \frac{\Delta Q_m}{\Delta Q_{ref}} = \frac{N}{\sum_{j=1}^{2} D_j} \\
N &= G_{ex} G_f^Q G_{field} G_{reg}^Q \left(k_6 k_7 + G_{mec} \left(k_1 k_6 k_7 - k_2 k_5 k_7 - k_2 k_8 \right) \right) \\
D_1 &= 1 + k_8 k_9 + G_{ex} G_{field} [\, G_f^V k_6 (1 + k8\ k9) + G_f^Q G_{reg}^Q k_6 k_7 \,] \\
D_2 &= G_{mec} (k_1 \left(1 + k_8 k_9 \right) + G_{field} (-k_2 k_4 - k_2 k_4 k_8 k_9 + \\
&+ G_{ex} (G_f^V \left(k_1 k_6 - k_2 k_5 + k_1 k_6 k_8 k_9 - k_2 k_5 k_8 k_9 \right) + \\
&+ G_f^Q G_{reg}^Q (-k_2 (k_8 + k5\ k7) + k_1 k_6 k_7)))
\end{aligned}
\qquad \text{(A.14)}
$$

A.5. Small synchronous generator and electrical network data

Table A-1: Grid characteristics at the Point of Common Coupling.

V [V]	400
f [Hz]	50
S_{sc} [MVA]	1.77

Table A-2: Synchronous Generator and shaft data
(with grey background the parameters not used for small signal model calculation).

Nominal power	**S_n [kVA]**	100
Nominal voltage	**V_n [V]**	400
Nominal frequency	**f_n [Hz]**	50
Inertia constant	**H [s]**	2
Friction factor	**K_d [p.u.]**	0.005
Armature resistance	**R_a [p.u.]**	0.002
Stator leakage reactance	**X_l [p.u.]**	0.14
d-axis unsaturated magnetizing reactance	**X_{ad} [p.u.]**	1.66
Field resistance	**R_{fd} [p.u.]**	1.40688e-3
Field reactance	**X_{fd} [p.u.]**	6.1789e-2
d-axis damping resistance	**R_{1d} [p.u.]**	4.0699e-3
d-axis damping reactance	**X_{1d} [p.u.]**	5.4581e-3
Lf1d-Lad	**X_{f1dad} [p.u.]**	0
q-axis saturated magnetizing reactance	**X_{aq} [p.u.]**	1.58
q-axis damping resistance	**R_{1q} [p.u.]**	1.4545e-2
q-axis damping reactance	**X_{1q} [p.u.]**	0.32928

Table A-3: AC5A parameters.

K_a [p.u.]	400
T_A [s]	0.02
T_{f1}[s]	1
K_f [p.u.]	0.03
K_e [p.u.]	1
S_E (mean value) [p.u.]	0.68
T_E [s]	0.8

Table A-4: measurement smoothing constants.

T_V [s]	0.02
T_Q [s]	0.04

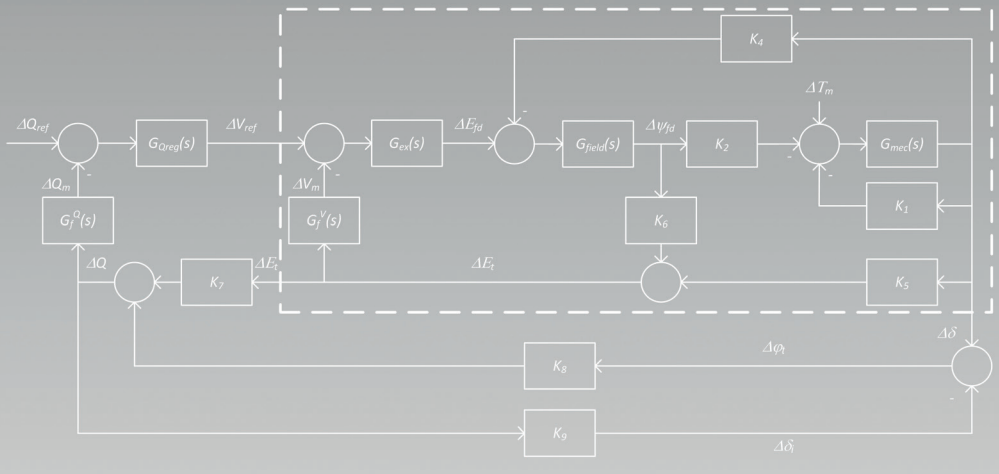

ISSN (online): 2246-1248
ISBN (online): 978-87-7112-493-4

AALBORG UNIVERSITY PRESS